DEVELOPMENT OF HIGHLY CORROSION RESISTANT PLATINGS VIA STRUCTURE DESIGN

A Doctoral Dissertation by

Jae-Hyeok PARK

MARCH 2021

DEPARTMENT OF CHEMICAL SYSTEMS ENGINEERING
GRADUATE SCHOOL OF ENGINEERING
NAGOYA UNIVERSITY

CONTENTS

CHAPTER 1

INTRODUCTION

1.1 Introduction

Corrosion is a natural and inevitable phenomenon in which the refined metal materials return to a more stable state by the surrounding environment [1]. Metals are essential materials used in variety of applications, including architectures, automobiles, railways, electronics, etc. and thus, corrosion has been an ever-lasting problem of human history [2]. Corrosion causes deformation and deterioration of metals and has led to serious social problems. For example, corrosion of metal parts in electronic products causes an increase in contact resistance and malfunction, and corrosion of cooling fins in air conditioner degrades cooling performance [3]. The corrosion of structure materials has led to deterioration and breakdowns of social infrastructure facilities such as bridges, buildings and so on. Nowadays, corrosion has become one of the most serious and worrisome problems of modern society. Thus, prevention of corrosion is one of the major tasks of recent times and the corrosion resistance of metal materials is considered as a most fundamental and essential property.

Moreover, recently developed and future technologies are also closely related to corrosion protection technologies. Recently, various technologies in areas, such as clean energy production and environmental conservation are being developed to reach the global goals for sustainable development [4,5]. Many of these technologies required advanced, safe and environmental-friendly corrosion protection technologies. For example, polymer electrolyte fuel cell (PEMFC), which is expected to be one of the most promising power sources using the environmental-friendly hydrogen as a fuel, high corrosion resistive components that can withstand the severe acidic environment during operation are essential [6,7]. Therefore, the development of an advanced but safe and environmental-friendly corrosion protection technology is a long and ever-lasting desire for human being, which not only provides solutions to problems of conventional technologies but also those of technologies to be developed in the future.

Among various surface treatment methods to prevent corrosion of such metals, platings have been widely used as a corrosion protective method for metals due to various advantages such as excellent performance and relatively low production cost [8]. For example, Zn and Zn alloy plating are used for anti-corrosion plating of steel materials in automobiles, home appliances, and infrastructure such as building, tower and bridges and Cr plating are used for hard coating for various industrial parts and decorative [9–13]. However, considering the fact that these materials are becoming to be applied in applications subjected to more harsh corrosive environments than before, the development of high corrosion resistance plating technology that surpasses conventional performance is increasingly required.

In addition, many conventional anti-corrosion platings contains toxic elements and increasing requirements for alternative platings using safer and abundant elements has drastically arose in recent years. Hexavalent chromium (Cr^{6+}) used for producing Cr platings are known to be carcinogenic [14,15] and Ni used in various heat- and corrosion-resistant platings and underlying plating for gold (Au) plating are known to be a major cause for metal allergy [16,17]. However, it is still insufficient for development of new plating materials that can replace the existing plating which have excellent properties. Therefore, in order to extend lifespans and save resources as well as maintenance cost of materials, it is essential to develop a new plating with excellent corrosion resistance.

In this dissertation, as a possible method to improve the performance of plating, a method of 'structure design' of the plating is proposed. The designing and controlling of plating structure are anticipated to be effective in improving the plating properties. For example, methods such as alloying with other elements [18,19], incorporating functional particles into the plating [20–22], or forming a multi-layered structure [23–25] can change the crystal structure or size, surface structure of the plating, and even change the corrosion mechanism of the plating by the change in corrosion product formation, which is the main factor for determining the corrosion resistance of the plating.

This dissertation summarizes a series of research on structure design of newly developed platings for improving the corrosion resistance of materials in various applications. Structure designs to meet requirements according to the applied

environment and purpose are of great importance considering the diverse applications existing in the present and future society. The research aims to provide solutions for developing plating structures to improve properties than conventional plating and also to replace the existing plating using harmful elements. The developed structural design shall contribute to the development of the industry as well as realizing a sustainable future.

1.2 Research background

1.2.1 Metal corrosion

1.2.1.1 Problems caused by corrosion

Corrosion occurs due to the interaction between the material and the environment, and corrosion occurs in various forms depending on the type of metal material and the exposed environment. Corrosion has caused various social problems for mankind so far. Corrosion damage to social infrastructure facilities and structures is considered as one of the most serious social problems [26]. Corrosion proceeds inconspicuously and slowly, and corrosion of steel reinforcing bars inside the concrete leads to a decrease in the life of the structure and, in severe cases, the collapse of the structures. For example, in 1967 the sudden collapse of a Silver Bridge over the Ohio, USA, caused by corrosive fatigue, resulted in the loss of 46 lives and millions of dollars in cost [27]. In addition, the collapse of Nanfangao Bridge in Taiwan in 2019 was also found to be due to corrosion of the steel wire that supports the load of the bridge [28]. The inside of the reinforced concrete supporting the bridge is in an alkaline environment, and the internal steel wire is protected in a passivation state. However, when cracks occur due to aging or defects of the concrete, chlorides seeps into the structure and destroys the passivation of steel, leading to corrosion, and finally the failure of structure. The National Association of Corrosion Engineers (NACE) in the United States estimates that annual maintenance costs for highways and bridges from corrosion are estimated at about $13.6 billion [29]. The Statue of Liberty in the United States has also become a social issue due to corrosion problems. Galvanic corrosion caused by contact of the copper plate on the surface of the statue and the internal reinforcement steel structure accelerated the corrosion of the structure, and in 1986, repair work was carried out with enormous cost [30].

Corrosion is also a common problem close to human daily life. Corrosion is problematic in automobile components, metal tools, electronic devices, and home appliances and so on. In automobiles, corrosion occurs in various parts, such as car body, suspension parts, brake caliper, muffler, fuel tank, and various fasteners, etc. Because automobiles are exposed to the harsh external environment, components directly exposed to the outside environment, such as brakes, suspensions and mufflers,

are susceptible to corrode by chloride ion [31]. The corrosion problem of automobile parts is an important problem that not only degrades the durability and performance of the material but can also cause a serious traffic accident and cause damage of human life. Toyota motors recalled 370,000 Lexus vehicles in 2017, and the reason was a possibility for crevice corrosion caused by poor locking of nuts on the suspension arm. Recently, some automakers have begun applying Zn-Ni alloy plating, which is more corrosion resistive than conventional Zn plating on brake calipers, where corrosion is accelerated by deicing agents used for roads in winter due to their high concentrations of chloride ions [32].

Corrosion is also a major task that must be solved indispensably for the future society. The bipolar plate, a key component of polymer electrolyte fuel cell (PEMFC), one of the promising next-generation clean energy source, requires high electric conductivity and corrosion resistance during operating [6]. Until now, various materials including carbon materials and stainless steel are considered as material for bipolar plate, but carbon materials are difficult to apply for fuel cell vehicles due to their low workability and brittleness, and stainless steel has high contact resistance due to its surface oxide film and insufficient corrosion resistance. Corrosion of bipolar plates cause failure of the component by lowering the cell voltage through formation of corrosion product on its surface, which increases the contact resistance, and by deteriorating the ion exchange membrane through elution of metal ions. Therefore, the development of metal materials with high corrosion resistance is essential for the development of next-generation technologies.

As can be seen from above, corrosion problem of metallic materials is not a limited issue in the past. The development of advanced corrosion protection technology is an essential for the development of present and future technology for human.

1.2.1.2 Definition of metal corrosion

In order to understand the corrosion phenomenon of metals, it is necessary to understand basic knowledge about the principle of metal corrosion [1]. Generally, to apply metal materials as an engineering material, they should be extracted from nature resources using external energy. Therefore, refined metals are not thermodynamically stable state in the open environment and tend to return to their stable state such as oxides and hydroxide, which has lower Gibbs free energy. Like this, the chemical or electrochemical phenomenon, in which metals return to their lower Gibbs free energy states are defined as corrosion. Basically, the corrosion reactions are composed as various chemical or electrochemical reactions, where in electrons pass between two half-cell reactions. In anodic reactions, corresponding to the dissolution reaction of metal, electrons are produced by the following reaction:

$$M^0 \rightarrow M^{n+} + ne^- \qquad (1.1)$$

Here, M represents a metal element and n represents ionic valence of each metal element. In the other half-cell reaction, defined as cathodic reaction, electrons are consumed. Cathodic reactions in aqueous solution depend on pH and availability of different components in solution. The most common cathodic reactions are hydrogen reduction reaction under acidic condition and oxygen reduction reaction under neutral or alkaline environment:

$$2H^+ + 2e^- \rightarrow H_2 \qquad (1.2)$$

$$O_2 + 2H_2O + 4e^- \rightarrow 4OH^- \qquad (1.3)$$

In general, corrosion of metals is a slow and steady process which destroys metallic structures and causes enormous direct and indirect maintenance cost for our society. Therefore, development of corrosion protection technology is considered as an indispensable technology in the industrial field.

1.2.1.2 Corrosion protection of metal

Corrosion protection is defined as method for protecting the metal from corrosion by reducing the corrosion rate of the metal through inhibition of either or

both the cathode and anode reaction of corrosion. Coatings are considered as an effective way to control corrosion of metals. Protective coatings, which act as protective barriers on the metal surface by slowing down anodic and cathodic reaction rates, can be prepared by various methods. The following Figure 1.1 shows the classification of surface finishing methods for various metallic materials. The classification of surface finishing methods is largely divided into two group: wet and dry process, which are those treated in the aqueous solution and those treated in vacuum or air, respectively. Among the various surface finishing methods, electroplating is a widely used coating method that provides corrosion protection for metallic materials; such as steel, aluminum and magnesium, with superior anti-corrosion property, relatively low production cost, simple and affordable equipment [33]. The principle and application of electroplating will be explained in the next chapter.

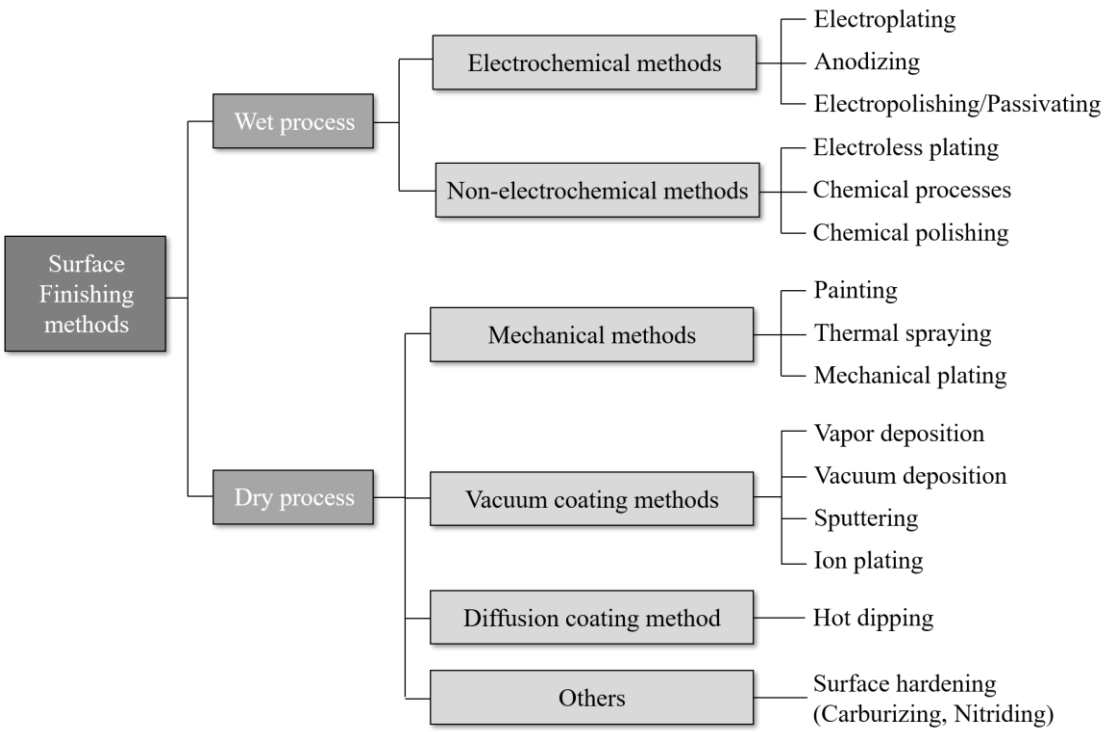

Figure 1.1 Classification of metal surface finishing methods.

1.2.2 Electrodeposition

1.2.2.1 Principle and applications

Electrodeposition can be broadly defined as the process of depositing a material onto the electrode by electrolysis [8]. Based on the principle of electrochemistry, it is a process that uses electricity to reduce the ions of a desired metal from an electrolyte and form continuous films of those materials onto a conductive surface. In general, the growth process of the metallic film by electrodeposition can be divided into the following three processes [34].

① Transfer of metal ion M^{z+} to the substrate surface

② Generation of adsorbed metal atom M_{ad} by interfacial passage

③ Crystallization process by surface diffusion or crystallization reaction of M_{ad} ($M_{ad} \rightarrow M_{crystal}$)

The first reaction relies on diffusion of metal ions inside the electrolyte, and the second reaction is a discharge reaction using overvoltage as a driving force. The second reaction speed (v mol/cm^2·s) is proportional to the current (i A/cm^2) according to Faraday's law ($i = zFv$). The discharge reaction can be expressed by the following equation:

$$M^{z+} + ze^- \rightarrow M_{ad} \qquad (1.4)$$

Based on this principle, electrodeposition is widely utilized in various industrial areas as a method for manufacturing metal coatings. Electrodeposition offers several advantages compared to other surface treatment technologies, such as:

- Relatively low production cost
- Simple and affordable equipment
- Relatively low operating temperature
- Controllable thickness, composition and microstructure of deposit
- Production of high purity and low defect-density deposit

According to these advantages, electrodeposition has been applied in various industrial areas to extend the lifecycle of materials by improving their corrosion resistance and also to impart functionalities, such as electrical conductivity, wear and friction resistance, heat tolerance, and also for decorative purpose.

1.2.2.2 Electrodeposition of alloys

1.2.2.2.1 Principle of alloy deposition

Fabrication of alloys by electrodeposition has been mainly used for decoration or anticorrosive purposes such as Zn-Ni, Ni-Co, Cu-Zn, Co-Sn, Sn-Ni, Pb-Sn, etc [33]. In recent years, electrodeposition has been extended to the preparation of magnetic alloys, amorphous alloys, and compound semiconductors [34]. In the electrolyte containing two kinds of metal ions; M^{m+} and N^{n+}, are reduced to absorbed atoms M_{ad} and N_{ad} on the electrode surface by discharge reactions shown in equations 1.2 and 1.3. Then, an M-N alloy film is formed by an alloying reaction on the electrode surface (equation 1.4). The alloy deposition model is shown in Figure 1.2.

$$M^{m+} + me^- \rightarrow M_{ad} \qquad (1.5)$$

$$N^{n+} + ne^- \rightarrow N_{ad} \qquad (1.6)$$

$$M_{ad} + N_{ad} \rightarrow M\text{-}N_{alloy} \qquad (1.7)$$

In order to co-deposit two different metals, each of their deposition potential must be reasonably close. For instance, the standard potential E^0 of both metals are close in the case of Sn and Pb (-0.126 and -0.136 V (vs. SHE) [35], respectively) and thus electrodeposition of Sn-Pb alloys is possible. Even though the deposition potentials of the two metals can be slightly controlled toward each other by changing the concentration of one of the metal ions in the plating bath, this method has a limited range of applicability. Meanwhile, when the two metal ions have widely different E^0, basically codeposition does not take place. However, their reduction potential can be made close enough to induce codeposition by forming complex ions through addition of complexing agent with different stability constants. Although, when using a complexing agent for alloy deposition, the solution chemistry of plating bath and

possible formation of metal complexes must be fully considered [35]. In alloy plating, the composition of the alloy is determined by the ratio of the partial current of each alloy component, and the partial current is determined by the overvoltage for each component [34]. The investigation on the kinetics of electrodeposition for alloys is fairly complicated because at least two or more electrode reactions occur simultaneously. The investigated relation between current and potential indicates a combination of the various redox reactions, each reaction having its own overpotential, potential and rate constant, related to the applied current density. Therefore, any information obtained from the current-potential relation have meaningful values in evaluating the electrodeposition mechanism of the alloy.

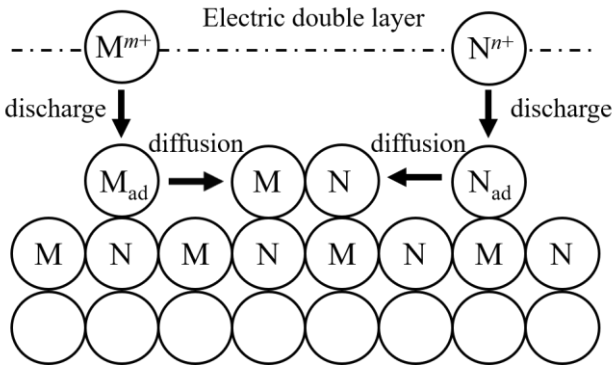

Figure 1.2 Alloy deposition model [34].

1.2.2.2.2 Classification of alloy deposition

Brenner [8] classified alloy plating as shown in the following Figure 1.3. Regular codeposition is a case when the electrodeposition of an alloy proceeds under the diffusion-controlled mechanism, and the composition of the deposits is governed by the diffusion rate of each ion. Irregular codeposition is when the composition of the electrodeposition is dominated by their potentials. Equilibrium codeposition is when the composition of the deposits is proportional to the concentration of ions in bath. These processes are classified as 'normal codeposition because the composition of the whole alloy deposits can be qualitatively predicted from the equilibrium potential of the component metals.

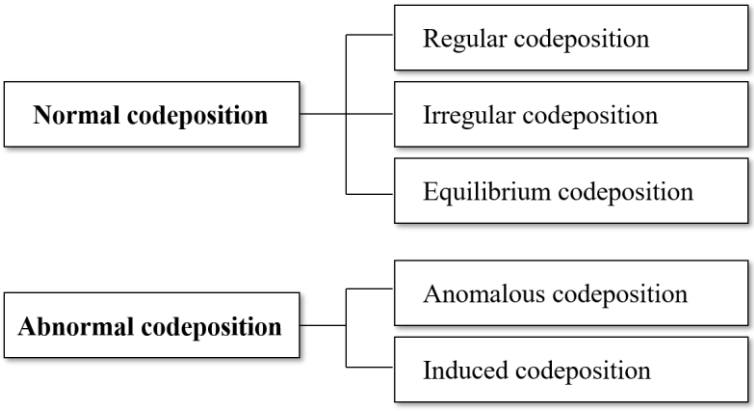

Figure 1.3 Classification of alloy deposition [8].

On the other hand, abnormal codeposition is when the composition of deposits cannot be predicted from the equilibrium potential of the component metals. Anomalous deposition is defined that the elemental composition of the alloy deposits exhibits unexpected behaviors. This is a case in which relatively low-potential metals precipitate preferentially over noble-potential metals, and this phenomenon normally occurs mainly in alloy deposition of iron-group metals (Fe-Ni, Ni-Co, etc) or zinc-iron group metal alloys [33]. One possible theory is that one of the alloying elements form metal hydroxides at electrode surface, which inhibits the reduction of the other. Another hypothesis is that the two or more ions form a mixed-metal complex, for example:

$$Fe^{2+} + Cit^{3-} \rightarrow [FeCit]^{-} \quad (1.8)$$

$$Ni^{2+} + Cit^{3-} \rightarrow [NiCit]^{-} \quad (1.9)$$

followed by,

$$[FeCit]^{-} + [NiCit]^{-} \rightarrow [FeNiCit]^{+} + Cit^{3-} \quad (1.10)$$

Induced codeposition is a case in which an element that does not precipitate alone but is precipitated through codeposition with other metals. This is the case when deposition of elements that generally cannot be not electrodeposited in aqueous solutions take place, such as tungsten (W), molybdenum (Mo), phosphorus (P), germanium (Ge), etc. These elements can be deposited as alloys with iron-group metals. For example, elements, such as Mo, W, P and B cannot be electrodeposited

alone from an aqueous solution. However, these elements can be codeposited with iron-group elements, such as Fe, Co and Ni. This principle was widely applied to electrodeposition of Ni-P alloy platings and later for electrodeposition of W and Mo alloys with iron-group elements. This has a great research interest from an academic point of view, to understand the mechanism of induced codeposition, as well as for the improvement of plating baths for industrial use. This is considered as an anomalous deposition that the elemental composition of the deposited alloy cannot be directly predicted from the obtained electrochemical behaviors of each mentioned element.

1.2.2.3 Mo, W and their alloys

In this dissertation, electrodeposited alloy plating using refractory metals, Mo and W, which have superior properties such as high hardness, thermal stability and corrosion resistance, etc. are selected as a high corrosion resistive plating material [19,35–37]. The fabrication of metal Mo, W and its alloys are challenging because they have high melting point of 2,622 and 3422 °C, but it is possible to manufacture their alloy plating even at low temperatures using electrodeposition, based on electrochemical reaction in an aqueous solution [8]. The following describes the properties of metal Mo and W, and their alloy electrodeposition.

1.2.2.3.1 Properties of Mo and W

Mo is a silvery-white, ductile, hard, refractory metal which suitable for alloy components required high strength and corrosion resistance at high temperature. The melting point of Mo is 2622 °C, which the fifth highest among the metals. And it has highest electric conductivity among all refractory metals, and high thermal conductivity compared to Fe, Ni based alloys [35]. It also has superior mechanical properties such as high tensile strength, Young’s modulus and hardness. The major application of Mo in industrial fields is an alloying element of alloy steels, tools, stainless steels and superalloys based on Ni or Co. Mo also have high thermal conductivity, low thermal expansion coefficient and low specific heat, important in various electronic applications.

Meanwhile, W possess the highest melting point, lowest thermal expansion coefficient and highest tensile strength among the metals. W maintains superior strength and hardness at high temperatures and also corrosion resistance. W and its alloys have been used in filaments, electric contacts, heating elements, thermocouples, cutting tools, bearings and corrosion-resistant alloys [38]. Recently, its application fields become wider as electrode materials for hydrogen evolution reaction (HER) and possible substitutes for hard chromium (Cr) plating with its high hardness, wear resistance and corrosion resistance [39–41]. However, W has limited availability owing to its fairly expensive cost. Various properties of Mo and W are listed in Table. 1.1.

Table 1.1 Properties of Mo and W [38].

Property	Mo	W
Atomic number	42	74
Atomic mass, M (g mol^{-1})	95.9	183.8
Oxidation states	2,3,4,5,6	2,3,4,5,6
Crystal structure	bcc	bcc
Atomic radius, r_{metal} (Å)	1.39	1.41
Density, ρ (g·cm^{-3})	10.1-10.3	19.25-19.35
Melting point, T_m (°C)	2,607-2,622	3,410-3,420
Thermal conductivity, k (Wm^{-1}K^{-1})	129-147	170-175
Specific resistivity, ρ (Ω·cm)	5.2-6×10^{-8}	5.4-6×10^{-8}
Tensile strength, σ_u (MPa)	380-2,100	1,670-3,900
Yield strength, σ_y (MPa)	170-2,000	1,350-3,500
Young's modulus of elasticity, E (GPa)	315-343	340-405
Strain at fracture, ε_f (%)	1-45	1-25
Poisson's ratio, v	0.29-0.295	0.27-0.29
Hardness (MPa)	1,500-6,500	4,500-8,500

1.2.2.3.2 Electrodeposition of Mo, W and its alloys

Mo, W and its alloys have been used in various industrial fields due to their a superior tribological, mechanical, thermal and corrosion properties [35]. Nevertheless, the fabrication of metal Mo, W and its alloys are energy consuming because they have high melting point of 2,622 and 3422 °C. In terms of resources and energy saving, reduction of production cost is considered a necessary factor in order to apply these metals to various industrial fields.

In this respect, electrodeposition is anticipated as a cost-effective and economical method for preparing Mo and W alloys because it requires relatively low temperatures in the range of 20 to 100 °C (in case of aqueous solution) for operating. However, electrodeposition of metal Mo and W from aqueous solution is generally difficult because of theirs highly oxidized ionic states. The reduction of oxy-anion such as MoO_4^{2-} and WO_4^{2-} is a fairly complex process. This process involves transfer of eight protons and six electrons to metal state and may proceed in several reaction steps. Attempts to preparing the pure Mo and W coating has been tried from 140 years ago. However, recently, it is commonly recognized that W cannot be electrodeposited alone from aqueous solution, because of its highly oxidized states, such as paratungstates; $[HW_6O_{21}]^{5-}$, metatungstates; $[H_2W_{21}O_{40}]^{6-}$ and tungstate; $[WO_4^{2-}]$ ions. Until now, the electrodeposition of pure metal Mo or W has been reported to be only possible from high temperature molten salts [42–44], which is one of the non-aqueous solutions.

Although pure metal Mo and W cannot be electrodeposited from aqueous solutions, they can be codeposited as an alloy with iron-group metals, which based on the principle of the induced codeposition as firstly presented by Brenner [8]. Electrodeposition of iron-W group alloy plating can be obtained by induced codeposition in a plating bath with complexing agent by forming mixed-metal complexes. Normally, electrodeposition mechanism of iron-group metal with Mo alloys shows similar tendency to that of W [35]. However, it should be remembered that even though the two deposition behaviors are similar, they are not the same and differences are reported. According to Ernst and Holt [45], molybdate ion was first deposited at cathode as an oxide-states and could be reduced to metallic state by

hydrogen in the presence of the iron-group metals. The number of unpaired-electrons adsorbed in the iron-group metals was anticipated to be the main factor to form a bond with hydrogen and, thereby, reduce the Mo oxide to Mo metal [45]. In recent years, several theories to explain the mechanism of induced codeposition of Mo with the iron-group metals have been newly reported [46,47]. Based on their reports about the electrodeposition of Ni-Mo alloys, the deposition precursor for the Ni-Mo alloy was anticipated to be an adsorbed intermediate mixed-metal complex, $[NiCit(MoO_2)]^-_{ads}$. Metal Mo can be electrodeposited from this mixed-metal intermediate. And the formation of deposition precursor, $[NiCit(MoO_2)]^-_{ads}$, is mainly affected by the fraction of Cit-Mo complex ions (Figure 1.4), similar to W.

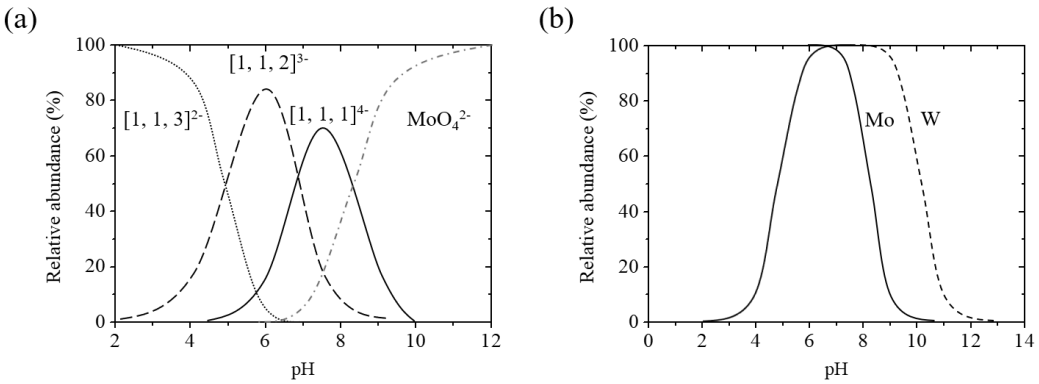

Figure 1.4 The relative abundance of complex ions: (a) pH dependence of protonated $[(MoO_4)(Cit)(H)_m]^{-(5-m)}$ complexes, and (b) Comparison of the sum of both concentrations of $[1,1,2]^{3-}$ and $[1,1,1]^{4-}$ of MoO_4^{2-} and WO_4^{2-} with Cit^{3-} as bath pH [35,46].

1.2.3 Structure design of plating

The properties of plating are not simply determined by the thickness of the plating but are greatly influenced by the structure of the plating [48]. The structure of the plating mentioned here can include the crystalline phase, the grain size, alloying elements, surface roughness and the layered structure of the plating and so on. Therefore, in order to manufacture a plating material with improved performance, structure designs to meet requirements according to the applied environment and purpose are of great importance. In this dissertation, the following three different structural control solutions were applied to suit the application environment and purpose of use.

1.2.3.1 Method 1: Incorporation of functional particles

The first method considered for structure design of plating is to incorporate functional particles into the plating. Recently, the composite plating, which forms a metal/particle composite plating by dispersing functional particles in the plating bath, is being used for improving various properties of plating. This method enables us to impart specific properties such as water repellency, abrasion resistance, electric conductivity and most importantly, corrosion resistance to the plating according to the kind of functional particles incorporating into the plating [22,49]. For example, the composite of ceramic particles such as SiO_2 and Al_2O_3 improves the hardness, abrasion resistance and wear resistance of plating [50,51], and diamond is effective in improving hardness, wear resistance, thermal property and also corrosion resistance [52,53]. Ashassi-Sorkhabi et al. [45] reported that electroless Ni-P plating has a columar plating structure and corrosion proceeded along this structural boundary, leading to accelerated corrosion rate. On the other hand, codeposited nano-diamond in Ni-P plating prevented the growth of this columnar structure and transformed the plating structure. This transformed plating structure contributed to improve the corrosion resistance of plating by acting as a barrier to the growth of the corrosion path.

Among the various candidates for composite particles, carbon nanotube (CNT) with high corrosion resistance and conductivity have been reported

to have the effect of improving the friction resistance, abrasion resistance, corrosion resistance and conductivity of the plating when composited in the plating layer [49,54,55]. Therefore, by incorporating CNT into plating, it is anticipated that corrosion resistance as well as electrical conductivity of plating could be improved. This method was thought to be applicable as a method for improving the properties of coating for bipolar plate of PEMFC that requires high corrosion resistance and electric conductivity in acidic environment.

1.2.3.2 Method 2: Addition of third element

Alloying by addition of extra elements is also one of the effective methods that improves various properties of plating including corrosion resistance [19,56]. In general, in the case of Zn plating, which is widely used as corrosion resistance plating for steel materials, corrosion resistance is determined by the purity and thickness of the plating [34]. However, since there the corrosion resistance of pure zinc plating is limited, the corrosion resistance of Zn plating is improved by alloying with other metals, such as Zn-Ni, Zn-Fe, Zn-Co and Zn-Sn [57–60]. Even in the case of alloy plating, corrosion resistance is greatly affected by the type of alloying element and the content of the alloying element, and these factors determine the crystalline phase and macro and microstructure of the plating [61,62]. For example, in the case of Zn-Ni alloy plating, when the Ni content of the plating is about 15%, the structure of plating consist of *r* phase and the corrosion resistance become maximized [56]. In the corrosion of Zn-Ni alloy plating, relatively active Zn in the plating layer is firstly eluted and formed a Zn-based corrosion product layer on the surface, and the Ni-based plating layer remained and maintain the plating structure, thereby exhibiting high corrosion resistance. In the induced codeposition type binary alloy plating such as Ni-P and Ni-W, all the crystalline structure generally changes to a nanocrystalline structure through alloying, and the crystalline size is refined depending on the content of induced element, which is the main factor for determining the properties of plating such as corrosion resistance and hardness, etc [53,62]. Moreover, it has been reported that a ternary alloy plating such as Zn-Ni-P [63] and Zn-Ni-B [64] exhibits better corrosion resistance than binary Zn-Ni

plating because the crystal structure of the plating changes to an amorphous-like structure with less grain boundaries by the addition of the third element. Therefore, electrodeposition of ternary alloy by adding a third element into the binary alloy plating was adopted as a second method for improving the corrosion resistance of plating.

1.2.3.3 Method 3: Formation of multi-layer structure

The corrosion reactivity of the metal plating is generally determined by the electrochemical potential of the metals that comprises the plating. Also, the rate and direction of the corrosion reaction are determined according to the potential of plating and potential gap between the plating layer and the substrate. In general, Zn plating which has a lower redox potential (-0.76 V/SHE) than that of Fe (-0.44 V/SHE), is used for corrosion-resistive plating metal for various steel materials. Zn preferentially corrodes in the presence of steel in corrosive environments and protects iron substrate by acting as a sacrificial anode for Fe when defects were formed. However, since Zn plating has insufficient corrosion resistance, chromate treatment, which is types of chemical conversion treatment is used as a method to improve corrosion resistance [65]. The chromate coating layer acts as a protective film for the Zn plating layer, lowers the corrosion rate by decreasing active area of plating and contributes to the improvement of corrosion resistance by forming insoluble corrosion products. However, since the chromate treatment uses harmful Cr^{6+}, an eco-friendly alternative technology is required [12,14]. In addition, in our previous study, it was confirmed that the Mg film laminated on the Zn-based plating contributes to the improvement of corrosion resistance by forming protective Mg corrosion products and also transforming the corrosion products of eluted Zn into a more compact and protective structure [58]. Therefore, the formation of a multilayer plating structure is expected to be an effective method that can improve the corrosion resistance of plating by changing the direction of corrosion progression between each plating layer or slowing the corrosion rate of overall plating layer. Moreover, the relation between the stacked layers may evolve a new corrosion protection mechanism based on the reaction promoted by the existence of the secondary layer, which may further enhance

the corrosion resistance. Therefore, multilayer formation was considered as a third method to improve the corrosion resistance of Zn-based plating by lamination of an additional coating using a harmless element.

1.3 Objective of this dissertation

This dissertation aims to prepare high corrosion resistance alloy plating comprising Mo or W through structural design, and to clarify the effect of plating structure on the improvement of corrosion resistance of plating. Three approaches for structure design of platings have been explored considering the environment of three applications in this dissertation. Adapted methods are as follows:

1. Incorporation of functional carbon material into plating: 'electrodeposition of metal/carbon composite plating'
2. The addition of the third element into binary alloy plating system: 'electrodeposition of ternary alloy plating'
3. Formation of multilayer structure by additional coating onto plating.

Above methods were applied to the following three research contents, respectively.

(I) ***Electrodeposition of Ni-W/CNT composite plating as a possible coating for PEMFC bipolar plate.*** The applicability of Ni-W/CNT composite plating as a new coating material for bipolar plate of polymer electrolyte membrane fuel cell (PEMFC) that requires high anti-corrosion property and conductivity in an acidic environment was discussed from a viewpoint of corrosion resistance and contact resistance. The effect of adding carbon nanotubes (CNT) to Ni-W alloy plating on the structural change and performance improvement of the plating is discussed.

(II) ***Electrodeposition of ternary Fe-W-Zn alloy plating: improvement of corrosion properties of binary Fe-W alloy by Zn addition.*** As for promising alternative for harmful Cr^{6+} plating, Ni-W alloy plating is considered as a promising plating. However, the use of Ni in plating also gradually becoming avoided because of its harmfulness to human body. Therefore, the electrodeposition of a novel ternary Fe-W-Zn alloy plating, which use affordable, harmless and eco-friendly Fe, was

studied as a possible alternative. The electrodeposition behavior of ternary alloy plating based on the influence on the Zn addition to the binary Fe-W alloy system is investigated, and the influence of the plating structure on the improvement of the corrosion resistance is discussed.

(III) ***Electrodeposition of ternary Zn-Fe-Mo plating and improvement in corrosion resistance by additional Mo-oxide coating.*** As a possible alternative for Zn-Ni plating, which uses harmful element Ni, ternary Zn-Fe-Mo plating was prepared by electrodeposition, and an additional Mo-oxide layer was formed on top of the Zn-Fe-Mo plating by electrodeposition in order to form a multilayer structure and further improve the corrosion resistance. The corrosion resistance of the prepared multilayer plating is evaluated, and the improvement in corrosion resistance is discussed from the viewpoint of the change in corrosion mechanism through the formation of a multilayer structure.

1.4 Structure of this dissertation

This dissertation is composed of the 5 chapters. Chapter 1 presents the necessity of the invention of a highly corrosion-resistant plating material and presents a solution via structural control of plating as a method for improving the corrosion resistance of plating. Also, backgrounds and objective of this dissertation were presented. Chapters 2, 3 and 4 consist of the conducted main research in this dissertation. The research topics introduced in section 1.3 will be explained in detail separately in chapter 2, 3, and 4, respectively. In Chapter 5, as a summary of this research, the conclusions obtained in each chapter are summarized and an overall conclusion along with future prospects are presented considering structure design of platings for corrosion protection. The structural overview of this dissertation is shown in Figure 1.6.

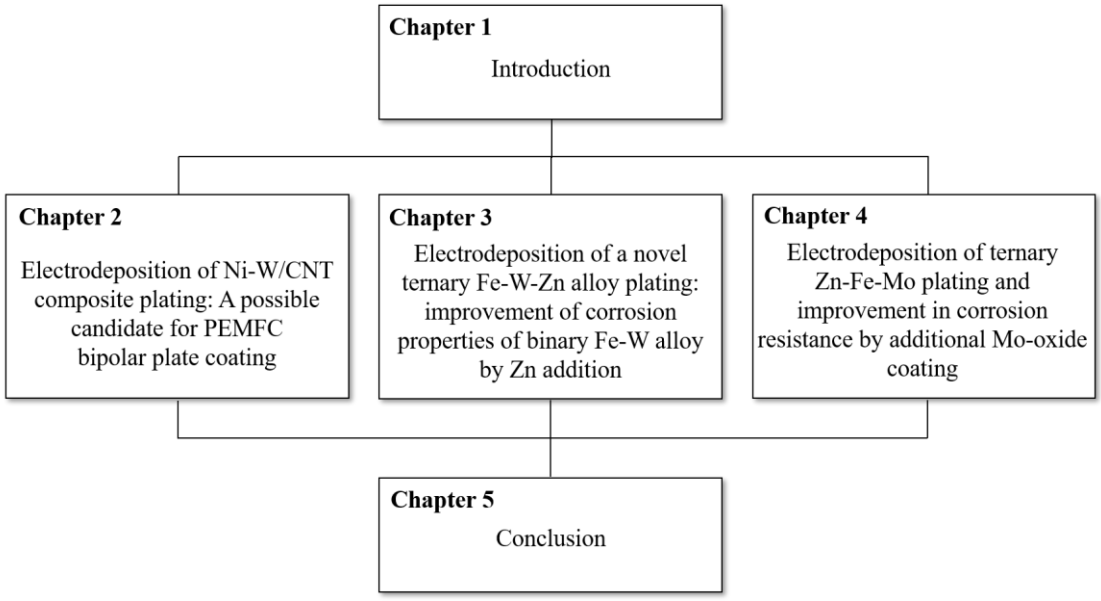

Figure 1.6 Structural overview of this dissertation.

References

[1] D.L. Piron, The electrochemistry of corrosion, Houston Univ., 1991.

[2] U.R. Evans, The Corrosion and Oxidation of Metals, Edward Arnold Pub, Ltd., 1960.

[3] R.B. Comizzoli, R.P. Frankenthal, P.C. Milner, J.D. Sinclair, Corrosion of electronic materials and devices, Science. 234 (1986) 340–345.

[4] R.W. Lashway, Fuel cells: the next evolution, MRS Bull. 30 (2005) 581–586.

[5] K.S. Dhathathreyan, N. Rajalakshmi, Polymer electrolyte membrane fuel cell, in: Recent Trends Fuel Cell Sci. Technol., Springer, 2007.

[6] D.P. Davies, P.L. Adcock, M. Turpin, S.J. Rowen, Bipolar plate materials for solid polymer fuel cells, J. Appl. Electrochem. 30 (2000) 101–105.

[7] R.C. Makkus, A.H.H. Janssen, F.A. de Bruijn, R.K.A.M. Mallant, Stainless steel for cost-competitive bipolar plates in PEMFCs, Fuel Cells Bull. 3 (2000) 5–9.

[8] A. Brenner, Electrodeposition of Alloys: Practical and specific information, Academic Press, 1963.

[9] J. Mackowiak, N.R. Short, Metallurgy of galvanized coatings, Int. Met. Rev. 24 (1979) 1–19.

[10] K. Nishimura, K. Kato, H. Shindo, Highly corrosion-resistant Zn-Mg alloy galvanized steel sheet for building construction materials, Nippon Steel Tech. Rep. 81 (2000).

[11] A.P. Yadav, H. Katayama, K. Noda, H. Masuda, A. Nishikata, T. Tsuru, Effect of Al on the galvanic ability of Zn–Al coating under thin layer of electrolyte, Electrochim. Acta. 52 (2007) 2411–2422.

[12] H. Bhatt, Alternatives to Hexavalent Chromium to Comply with European Union’s Directives (ELV, RoHS and WEEE), Plat. Surf. Finish. 93 (2006) 20–23.

[13] M.R.S. Beyragh, S.K. Asl, S. Norouzi, A comparative research on corrosion behavior of a standard, crack-free and duplex hard chromium coatings, Surf. Coatings Technol. 205 (2010) 2605–2610.

[14] L. Hua, Y.C. Chan, Y.P. Wu, B.Y. Wu, The determination of hexavalent chromium (Cr^{6+}) in electronic and electrical components and products to comply with RoHS regulations, J. Hazard. Mater. 163 (2009) 1360–1368.

[15] V.S. Protsenko, F.I. Danilov, Chromium electroplating from trivalent chromium baths as an environmentally friendly alternative to hazardous hexavalent chromium baths: comparative study on advantages and disadvantages, Clean Technol. Environ. Policy. 16 (2014) 1201–1206.

[16] J.P. Thyssen, Nickel and cobalt allergy before and after nickel regulation–evaluation of a public health intervention, Contact Dermatitis. 65 (2011) 1–68.

[17] M. Saito, R. Arakaki, A. Yamada, T. Tsunematsu, Y. Kudo, N. Ishimaru, Molecular mechanisms of nickel allergy, Int. J. Mol. Sci. 17 (2016) 202.

[18] J. Winiarski, W. Tylus, M.S. Krawczyk, B. Szczygieł, The influence of molybdenum on the electrodeposition and properties of ternary Zn-Fe-Mo alloy coatings, Electrochim. Acta. 196 (2016) 708–726.

[19] H. Kazimierczak, J. Morgiel, Z. Swiatek, J.M. Vega, E. García-Lecina, Effect of Mo addition on corrosion of Zn coatings electrodeposited on steel, Corros. Sci. 135 (2018) 107–119.

[20] Y. Kamimoto, S. Okura, T. Hagio, T. Wada, H. Tanaka, H. Hara, P. Deevanhxay, R. Ichino, Nickel–carbon composite plating using a Watts nickel electroplating bath, SN Appl. Sci. 2 (2020) 170.

[21] S. Arai, J. Fujii, Electroless deposition of silver on multiwalled carbon nanotubes using iodide bath, J. Electrochem. Soc. 158 (2011) 506–510.

[22] S. Arai, T. Saito, M. Endo, Cu–MWCNT composite films fabricated by electrodeposition, J. Electrochem. Soc. 157 (2010) 147–153.

[23] J. Zhang, W. Zhang, C. Yan, K. Du, F. Wang, Corrosion behaviors of Zn/Al–Mn alloy composite coatings deposited on magnesium alloy AZ31B (Mg–Al–Zn), Electrochim. Acta. 55 (2009) 560–571.

[24] E. Zoestbergen, J. van de Langkruis, T.F.J. Maalman, E. Batyrev, Influence of diffusion on the coating adhesion of zinc-magnesium thin films onto steel, Surf. Coatings Technol. 309 (2017) 904–910.

[25] M. Lee, I. Bae, Y. Kwak, K. Moon, Effect of interlayer insertion on adhesion properties of Zn–Mg thin films on steel substrate by PVD method, Curr. Appl. Phys. 12 (2012) 2–6.

[26] H. Böhni, Corrosion in reinforced concrete structures, Elsevier, 2005.

[27] A.G. Lichtenstein, The silver bridge collapse recounted, J. Perform. Constr. Facil. 7 (1993) 249–261.

[28] M. Greenwood, What caused Taiwan'S Nanfang'Ao bridge to collapse, 2020.

[29] N.G. Thompson, M. Yunovich, D. Dunmire, Cost of corrosion and corrosion maintenance strategies, Corros. Rev. 25 (2007) 247–262.

[30] R. Baboian, E.B. Cliver, Corrosion on the Statue of Liberty, part five: the Statue restoration, Mater. Perform. 25 (1986) 80–83.

[31] K. Takahashi, K. Mori, H. Takebe, Application of titanium and its alloys for automobile parts, in: MATEC Web Conf., EDP Sciences, 2020.

[32] T. Oriti, B. Heights, A comparative study of Gamma-Phase Zinc-Nickel deposits electroplated from various alkaline and acid systems, NASF Surf. Technol. White Pap. 79 (2014) 1–16.

[33] 若林信一, 次世代めっき技術 表面技術におけるプロセス・イノベーション, 日刊工業新聞社, 2005.

[34] 春山志郎, 表面技術者のための電気化学, 丸 善, 2001.

[35] N. Eliaz, E. Gileadi, Induced codeposition of alloys of tungsten, molybdenum and rhenium with transition metals, in: Mod. Asp. Electrochem., Springer, 2008.

[36] O. Younes-Metzler, L. Zhu, E. Gileadi, The anomalous codeposition of tungsten in the presence of nickel, Electrochim. Acta. 48 (2003) 2551–2562.

[37] W. Sassi, L. Dhouibi, P. Berçot, M. Rezrazi, E. Triki, Comparative study of protective nickel–tungsten deposit behavior obtained by continuous and pulsed currents from citrate–ammonia media, Surf. Coatings Technol. 206 (2012) 4235–4241.

[38] M. Ashby, G. Design, Material property data for engineering materials, Cambridge, 2016.

[39] G. Yar-Mukhamedova, N. Sakhnenko, T. Nenastina, Electrodeposition and properties of binary and ternary cobalt alloys with molybdenum and tungsten, Appl. Surf. Sci. 445 (2018) 298–307.

[40] A. Nicolenco, N. Tsyntsaru, H. Cesiulis, Fe (III)-based ammonia-free bath for electrodeposition of Fe-W alloys, J. Electrochem. Soc. 164 (2017) 590–596.

[41] K.A. Kumar, G.P. Kalaignan, V.S. Muralidharan, Pulse electrodeposition and characterization of nano Ni–W alloy deposits, Appl. Surf. Sci. 259 (2012) 231–237.

[42] F. Jiang, Y. Zhang, N. Sun, J. Leng, Tungsten coating prepared on molybdenum substrate by electrodeposition from molten salt in air atmosphere, Appl. Surf. Sci. 327 (2015) 432–436.

[43] A. Katagiri, M. Suzuki, Z. Takehara, Electrodeposition of Tungsten in $ZnBr_2$-NaBr and $ZnCl_2$-NaCl Melts, J. Electrochem. Soc. 138 (1991) 767.

[44] W. Simka, D. Puszczyk, G. Nawrat, Electrodeposition of metals from non-aqueous solutions, Electrochim. Acta. 54 (2009) 5307–5319.

[45] D.W. Ernst, M.L. Holt, Cathode potentials during the electrodeposition of molybdenum alloys from aqueous solutions, J. Electrochem. Soc. 105 (1958) 686.

[46] E.J. Podlaha, D. Landolt, Induced codeposition I. An experimental investigation of Ni-Mo alloys, J. Electrochem. Soc. 143 (1996) 885–892.

[47] E.J. Podlaha, D. Landolt, Induced Codeposition II. A Mathematical Model Describing the Electrodeposition of Ni-Mo Alloys, J. Electrochem. Soc. 143 (1996) 893–899.

[48] K.Y. Sasaki, J.B. Talbot, Electrodeposition of Binary Iron-Group Alloys, J. Electrochem. Soc. 142 (1995) 775–782.

[49] Z. Zhang, A. Kitada, T. Chen, K. Fukami, M. Shimizu, S. Arai, Z. Yao, K. Murase, Dispersion of multiwalled carbon nanotubes into a diglyme solution, electrodeposition of aluminum-based composite, and improvement of hardness, J. Alloys Compd. 816 (2020) 152585.

[50] A. Nicolenco, A. Mulone, N. Imaz, N. Tsyntsaru, J. Sort, E. Pellicer, U. Klement, H. Cesiulis, E. García-Lecina, Nanocrystalline Electrodeposited Fe-W/Al_2O_3 Composites: Effect of Alumina Sub-microparticles on the Mechanical, Tribological, and Corrosion Properties, Front. Chem. 7 (2019) 241.

[51] D. Dong, X.H. Chen, W.T. Xiao, G.B. Yang, P.Y. Zhang, Preparation and properties of electroless Ni–P–SiO_2 composite coatings, Appl. Surf. Sci. 255 (2009) 7051–7055.

[52] S.Q. Jia, F. Yang, High thermal conductive copper/diamond composites: state of the art, J. Mater. Sci. (2020) 1–34.

[53] H. Ashassi-Sorkhabi, M. Es, Corrosion resistance enhancement of electroless Ni–P coating by incorporation of ultrasonically dispersed diamond nanoparticles, Corros. Sci. 77 (2013) 185–193.

[54] P.M. Ajayan, O.Z. Zhou, Applications of carbon nanotubes, in: Carbon Nanotub., Springer, 2001.

[55] S. Arai, K. Miyagawa, Fabrication of Co-W Alloy/Multiwalled Carbon Nanotube Composite Films by Electrodeposition for Improved Frictional Properties, ECS J. Solid State Sci. Technol. 2 (2013) 39.

[56] I. Rodriguez-Torres, G. Valentin, F. Lapicque, Electrodeposition of zinc–nickel alloys from ammonia-containing baths, J. Appl. Electrochem. 29 (1999) 1035–1044.

[57] G. Roventi, R. Fratesi, R.A. Della Guardia, G. Barucca, Normal and anomalous codeposition of Zn–Ni alloys from chloride bath, J. Appl. Electrochem. 30 (2000) 173–179.

[58] Z.L. Qun, Electrodeposition of zinc-iron alloy from an alkaline zincate bath, Met. Finish. 96 (1998) 54–57.

[59] J. Winiarski, W. Tylus, B. Szczygieł, EIS and XPS investigations on the corrosion mechanism of ternary Zn–Co–Mo alloy coatings in NaCl solution, Appl. Surf. Sci. 364 (2016) 455–466.

[60] K. Wang, H.W. Pickering, K.G. Weil, EQCM studies of the electrodeposition and corrosion of tin–zinc coatings, Electrochim. Acta. 46 (2001) 3835–3840.

[61] H. Alimadadi, M. Ahmadi, M. Aliofkhazraei, S.R. Younesi, Corrosion properties of electrodeposited nanocrystalline and amorphous patterned Ni–W alloy, Mater. Des. 30 (2009) 1356–1361.

[62] N.P. Wasekar, N. Hebalkar, A. Jyothirmayi, B. Lavakumar, M. Ramakrishna, G. Sundararajan, Influence of pulse parameters on the mechanical properties and electrochemical corrosion behavior of electrodeposited Ni-W alloy coatings with high tungsten content, Corros. Sci. 165 (2020) 108409.

[63] Y. Kamimoto, K. Yamamoto, S. Yamashita, T. Sakai, R. Ichino, Preparation of Zn–Ni–P Alloys with High Zn Content Using Electrochemical Processes, Sci. Adv. Mater. 6 (2014) 2269–2274.

[64] T. Sakai, Y. Kamimoto, R. Ichino, Preparation of electrodeposited Zn–Ni–B alloy coatings, Jpn. J. Appl. Phys. 55 (2015) 01AA24.

[65] 井上雅博, 現代めっき教本, エレクトロニクス実装学会誌, 2012.

CHAPTER 2

Electrodeposition of Ni-W/CNT composite plating: A possible candidate for PEMFC bipolar plate coating

2.1 Background of this research

2.1.1 Polymer electrolyte membrane fuel cell (PEMFC)

Since the 20th century, energy has been intensively consumed due to advances in science and technology. Global energy consumption has gradually increased in recent decades and is expected to continue rising due to the explosive population growth of developing countries. About 90% of the current energy consumption is due to the burning of fossil fuels, and abnormal consumption of fossil fuels reduces the self-cleaning effect of the earth and causes various destruction of the global environment [1]. Above all, the problem of global warming caused by CO_2 is the biggest issue common to the world. In this perspective, fuel cells are attracting great attention as a promising power source due to their abilities to produce electricity from hydrogen, which emits no harmful gases in contrast to traditional fossil fuels [2]. The reaction product of fuel cells is only pure water and can contribute to reduce CO_2 emissions. Among the fuel cells, polymer electrolyte membrane fuel cell (PEMFC) is considered to be promising for fuel cell vehicles [3].

Since PEMFC can operate at low temperatures, it is expected to be used as a power source for automobiles, home generators, small power supplies and emergency power supplies [4]. On the other hands since the thickness of the electrolyte membrane is thin, high processing precision is required and catalyst poisoning by CO or organic matter is considered as shortcoming [5]. The basic structure of PEFC is shown in Figure 2.1. PEMFC has a structure in which the electrolyte layer is sandwiched between two bipolar plates. This structure is called a unit cell. Since the voltage of one cell is as only about 1 V or less, numerous cells are connected in series to increase the voltage [6].

When hydrogen gas is introduced into the anode and oxygen gas is introduced into the cathode, the following reactions (2.1) and (2.2) occur.

$$2H^+ + 2e^- + \frac{1}{2}O_2 \rightarrow H_2O \qquad (2.1)$$

$$H_2 \rightarrow 2H^+ + 2e^- \qquad (2.2)$$

The produced water is discharged from the cathode. Each electrode needs a catalyst to cause the reactions of (2.1) and (2.2), and a catalyst layer is formed on both the anode and cathode.

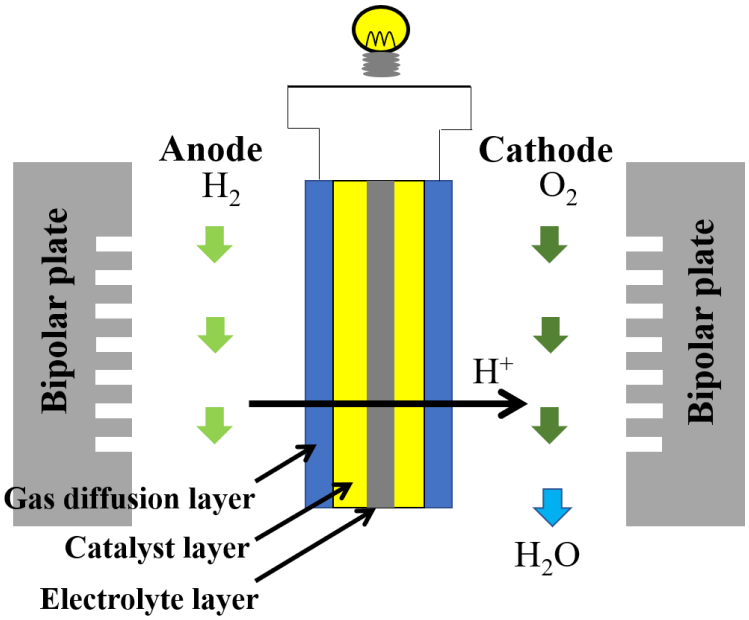

Figure 2.1 Schematic diagram for PEMFC operation.

2.1.1.1 Bipolar plate for PEMFC

The bipolar plate (also called separator) is considered as a one of the core components of PEMFC. The bipolar plate plays a critical role in PEMFC including the followings [5]:

(1) Separating each unit cell
(2) Connecting anode and cathode to provide conductive pathway
(3) Supplying reaction gas through a flow pathway
(4) Removing reaction products such as water and heats from cell

Therefore, the following properties are required for bipolar plate of PEMFC:

(1) Affordable cost
(2) Mechanical properties that can withstand the operating environment
(3) High electrical conductivity for enabling accumulation of cell voltage
(4) High corrosion resistance under acidic environment

Among these, electrical conductivity and corrosion resistance are considered as particularly important. Especially, high corrosion resistive metal materials that hardly corrode in acidic environment is needed since the operation environments of the PEMFC is similar to harsh acidic conditions. Metal ions eluted from metal parts are easily ion exchanged in the solid polymer electrolyte membrane, increasing resistance for proton conduction and thus causing the decrease in cell voltage. This causes degradation of the membrane and leads to failure of the fuel cell [7-9].

2.1.1.1.1 Materials for PEMFC bipolar plate

Currently, carbon and metal materials are used as materials for PEMFC bipolar plate [7]. Carbon materials show good electrical conductivity, anti-corrosion property and chemical stability, but carbon materials have some shortcomings for applying to automobile application owing to their insufficient mechanical properties and also low processability. The metal materials have high electric conductivity, superior mechanical properties and low cost. Thus, these are considered as suitable materials for PEMFC bipolar plate. Generally, stainless steel [10,11], aluminum [12,13], and titanium [14,15] plates are anticipated as promising materials, but the corrosion resistance of stainless steel and aluminum is insufficient, and the titanium plate has cost problems. The surface oxide film of such materials contributes to increase in corrosion resistance, but also increase the contact resistance. Corrosion of such a metal bipolar plate can occur at both anode and cathode side during PEMFC operation, and metal ions eluted by corrosion can contaminate the ion exchange membrane and reduce the activity of the catalyst layer [8,9]. Therefore, a surface coating method has been developed as a method to further improve the corrosion resistance of such metallic materials.

2.1.1.1.2 Coatings for PEMFC bipolar plate

As a method for enhancing the corrosion resistance of PEMFC bipolar plate, a surface finishing method of metals such as nitriding [16,17], physical vapor deposition [18,19], electroplating [20-22] methods are reported as a possible coating method. Ho et al. reported multi-layered TiN/CrN and CrN/Ti coating prepared by cathodic arc deposition exhibited further improved corrosion resistance and low contact resistance than stainless 304 substrate and also single layer TiN and CrN [19]. They reported that deposited CrN layer on top surface was effective in lowering the corrosion rate and underlying Ti layer was effective in improving the electric conductivity in the bi-layer coating structure. From this result, they suggested that the structural change of the coating may be effective in improving the properties of coating.

Among various coating methods for PEMFC, electroplating has some strongpoints such as low manufacturing cost, uniform coating, suitable for mass production and also applicable to complex-shaped parts. For high electric conductivity and high corrosion resistance, plating using noble metals such as gold [15], silver [22], and platinum [23] are considered as effective. Ho et al. reported electrodeposited Ag/polytetrafluoroethylene (PTFE) composite plating was a promising coating material for PEMFC bipolar plate [22]. They suggested that the PTFE particles dispersed on the Ag plating surface reduced surface defects and roughness of plating. This cause increased in water repellency with high contact angle, and also effective in improving corrosion resistance. However, considering the need to reduce the production cost of PEMFC, the high manufacture costs for such noble-metal plating hinder their application. Therefore, for application to PEMFC bipolar plate coating, the development of a new plating technology that does not use expensive noble metals and has high corrosion resistance with conductivity is required.

2.2 Proposed structure design of plating

In this study, Ni-W alloy plating was considered as a possible coating material for PEMFC bipolar plates, which requires high corrosion resistance in acidic environments. However, considering the bipolar plate material used in harsh acid environments, the corrosion resistance of Ni-W plating may not be sufficient. Moreover, in consideration of the point that the contact resistance of Ni-W plating can be increased by the formation of oxide film on the plating surface due to the W content, structural design of plating for improving corrosion resistance and lowering contact resistance was considered. As a promising solution, incorporation of carbon nanotubes (CNT), one of the carbon materials with high electrical conductivity and also corrosion resistance, into the plating layer was considered. It is expected that the corrosion resistance of the plating will be improved by the presence of inactive CNT on the plating surface, and the CNT evenly distributed in the plating layer will act as a proper conductive path to improve contact resistance of plating layer. In order to obtain this designed-plating structure, a composite plating method, which particles are dispersed in a plating bath to form a metal/particle composite film was applied. The graphical overview of the designed plating structure is shown in Figure 2.5.

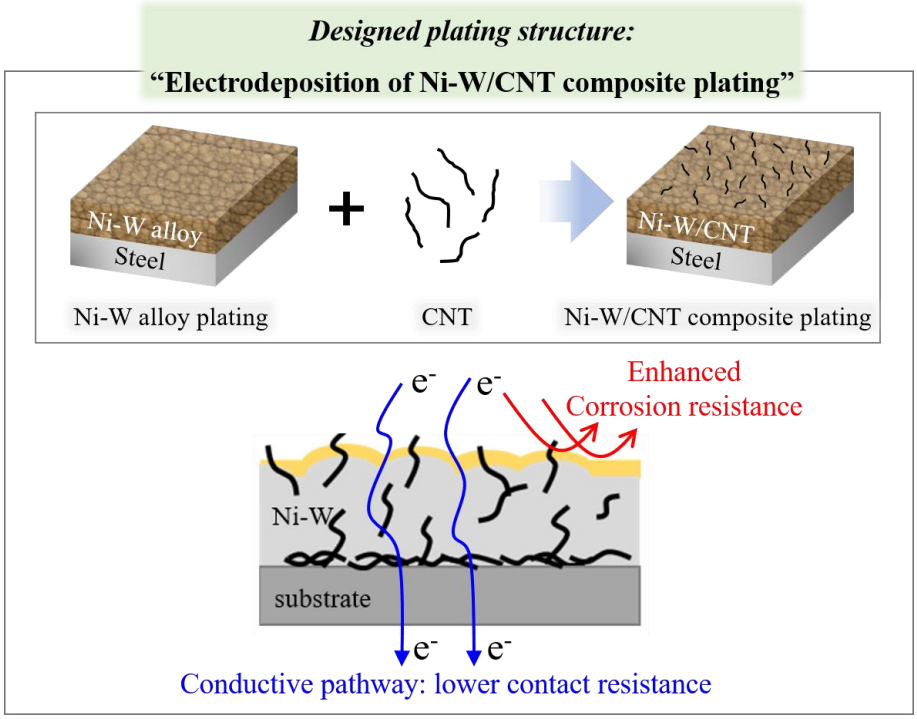

Figure 2.5 The graphical overview of the designed plating structure.

2.3 Objective of this work

This study aims to examine the applicability of electrodeposited Ni-W/CNT composite plating as a new coating for PEMFC bipolar plate. In addition, the effect of CNT incorporation on the property improvement of the electrodeposited Ni-W plating was studied, and the effect was discussed in terms of the structural change of the plating.

Ni-W/CNT composite plating was prepared by electrodeposition from citrate-based Ni-W plating bath containing dispersed CNT. The effect of hydrothermal treatment of hydrophobic CNT in a mixed-acid solution for improving the dispersibility of CNT in aqueous solution was investigated. Also, the change of electrodeposition behavior according to the addition of CNT into the Ni-W plating bath was investigated, and the optimum concentration of CNT added was discussed. The structure of the electrodeposited composite plating was observed, and the effective plating structure to improve corrosion resistance and contact resistance was discussed. The corrosion resistance of the prepared composite plating was evaluated in 0.5M H_2SO_4 solution, which similar corrosion environment of PEMFC bipolar plate. And its contact resistance was measured and compared with Ni and Ni-W plating without containing CNT. In addition, changes in the plating structure of the composite plating as corrosion progress are observed, and its effects on properties of composite plating are discussed. Finally, improvement of the properties of Ni-W alloy plating by CNT addition and applicability of Ni-W/CNT composite plating as a coating material for PEMFC bipolar plate was discussed.

2.4 Materials, chemicals, and equipment

Materials, chemicals and equipment used in this study are listed in Table 2.3 and 2.4, respectively. All chemicals were used as purchased without any further purifications.

Table 2.3 Materials and chemicals

Materials and chemicals	Company
Tri-ammonium citrate ($(NH_4)_3C_6H_5O_7$, ≥ 95.0%)	Nacalai Tesque, Inc, Japan
Nickel (II) sulfate hexahydrate ($NiSO_4 \cdot 6H_2O$, ≥ 99.0%)	Nacalai Tesque, Inc, Japan
Sodium tungstate dihydrate ($Na_2WO_4 \cdot 2H_2O$, ≥ 98.0%)	Nacalai Tesque, Inc, Japan
Sulfuric acid (H_2SO_4, 98.0%)	Nacalai Tesque, Inc, Japan
Nitric acid (HNO_3, 60-61%)	Nacalai Tesque Inc, Japan
Hydrochloric acid (HCl, 35.0-37.0%)	Nacalai Tesque Inc, Japan
MWCNT (VGCF)	Showa Denko co., Japan
Commercial steel plate (B-60-P01)	Yamamoto-MS Co., Japan
Commercial nickel plate (NI-313374, 99%)	Nilaco, Japan

Table 2.4 Equipment

Equipment	Details	Company
Potentio/galvanostat	HZ-5000	Hokuto-denko, Japan
Electric crucible furnace	VF-3000	SK Medical, Japan
Scanning electron microscope (SEM)	JSM-6330F	JEOL, Japan
Energy-dispersive spectroscopy (EDS)	SEM-EDX Type N	Hitachi, Japan
X-ray diffractometer (XRD)	Ultima IV	Rigaku, Japan
Carbon-sulfur analyzer	EMIA-510	Horiba, Japan
4-probe contact resistance measurement apparatus	SourceMeter 2612A	Keithley, USA
ICP-AES	SPS7800	Seiko instruments, Japan

2.5 Surface modification of CNT

2.5.1 Hydrothermal treatment of CNT

Normally, when single-walled carbon nanotube (SWCNT) is functionally modified, the C=C bond is cleaved during the chemical treatment, causing structural defects and changing the electrical and mechanical properties. However, in the surface modification of MWCNT, only the exterior is chemically modified, so that the characteristics peculiar to CNT are maintained. Moreover, MWCNT has the advantages of easier mass production and lower cost per unit than SWCNT. Therefore, the multi-walled carbon nanotube (MWCNT) was used as CNT source in this study.

Because CNT is hydrophobic, the dispersibility in aqueous solution is insufficient. Surface modification of CNT in acid solution is widely used method for enhancing dispersibility in solution. Therefore, hydrothermal treatment of CNT in acidic solution was performed to enhance its dispersibility in aqueous solution. The CNT was added into 100 mL of constant pressure container with mixed acid solution (volume ratio of sulfuric acid to nitric acid = 3:1) and hydrothermally treated at 100 ℃ for 2 hours. 100 mg of CNT was added in 10 mL of mixed-acid. Hydrothermally treated CNT was rinsed with sulfuric acid solution (pH adjusted: 3.7) by vacuum filtration. The rinsed CNT was added to the plating bath immediately to prevent aggregation.

2.5.2 Characterization of CNT

The effects of hydrothermal treatment of CNT were investigated. The SEM micrographs for the pristine and hydrothermal treated CNT in mixed acid is shown in Figure 2.6. The untreated CNT showed smooth surface with its diameter of about 200 nm while appearance of hydrothermally treated CNT became thinner and shorter than before. From the color of mixed acid solution changed colorless to brown after hydrothermal treatment, it was considered that the reaction proceed as the graphite on the surface of MWCNT peels off and changing the appearance by cutting the CNT during hydrothermal treatment.

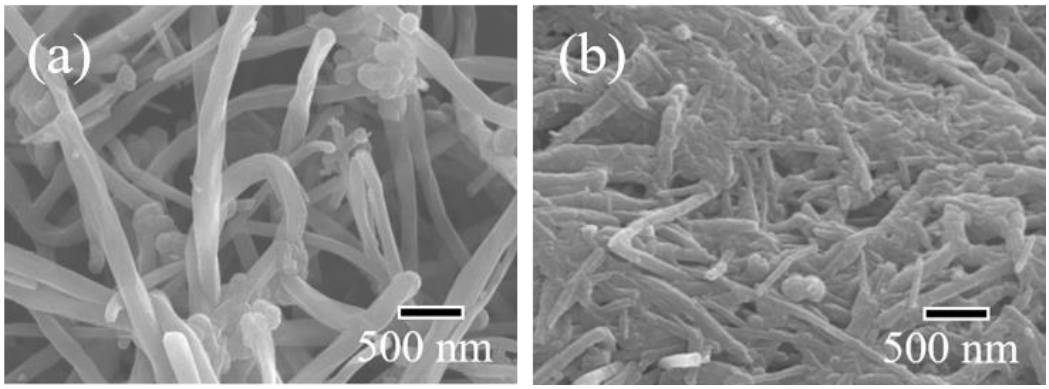

Figure 2.6 SEM micrographs for CNT: (a) pristine and (b) after hydrothermal treatment in mixed acid at 100 °C for 2 hours.

The following Figure 2.7 shows the photographs of Ni-W plating bath containing 10 g/L of pristine CNT and hydrothermal treated CNT 10 g/L, respectively.

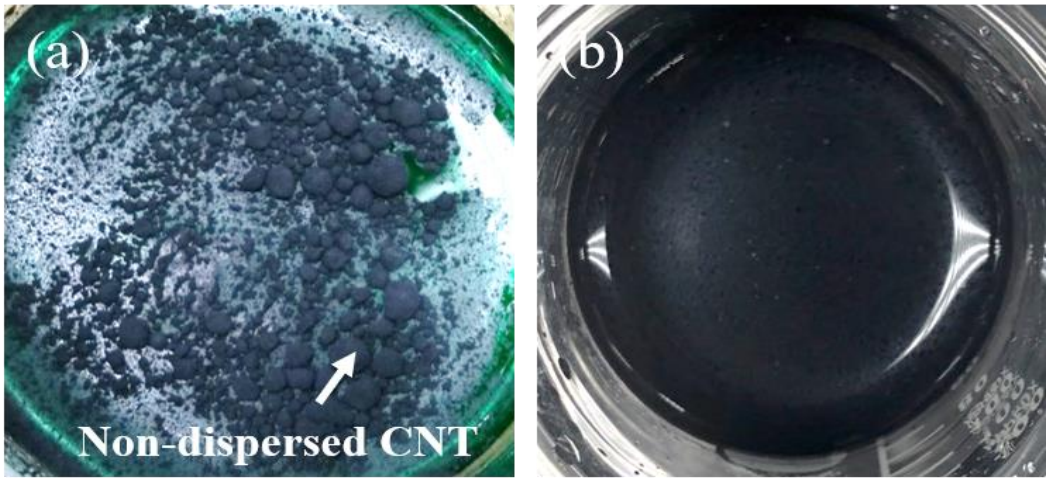

Figure 2.7 Photographs for Ni-W plating bath with the addition of CNT: (a) pristine CNT 10 g/L and (b) hydrothermal treated CNT 10 g/L.

While Ni-W plating bath with 10 g/L of pristine CNT showed bad dispersibility and aggregation of CNT at the bath surface, the bath with hydrothermal treated CNT showed well-dispersed plating bath. It was confirmed that a Ni-W plating bath with well-dispersed CNT could be prepared through the hydrothermal treatment of CNT in mixed acid solution.

2.6 Electrodeposition of Ni-W/CNT composite plating

2.6.1 Bath preparation

Electrodeposition of Ni-W and Ni-W/CNT composite plating were prepared by galvanostatic deposition at citrate-ammonia baths. The bath was prepared with 0.3 mol/L of $(NH_4)_3C_6H_6O_7$, 0.2 mol/L of $Na_2WO_4 \cdot 2H_2O$ and 0.1 mol/L of $NiSO_4 \cdot 6H_2O$ and the total volume of bath was adjusted to 100 ml. The pH of plating bath was set to 7.0 with diluted H_2SO_4 solution and bath temperature was kept at 40 °C using water bath. The addition amount of hydrothermal treated CNT to plating bath was 1, 5 or 10 g/L.

2.6.2 Cathodic polarization measurement

Cathodic polarization measurement was conducted to investigate the electrodeposition behavior of Ni-W/CNT composite. The Ni plates was used as cathode and surface area was fixed to 1×1 cm^2 by masking extra area with insulating tape. Before use, the Ni plates were degreased with ethanol and chemically etched with hydrochloric acid. Polarization measurements was conducted with a scan rate of 5 $mV \cdot s^{-1}$ from open circuit potential (OCP) to -1.4 V (vs. Ag/AgCl in sat. KCl solution) under magnetic stirring at 500 rpm for preventing aggregation of CNT in plating bath. Cathodic polarization curves measured using plating baths with various CNT concentration are shown in Figure 2.8.

For the pristine Ni-W plating, the increasement of current density from about -700 mV was confirmed. However, the Ni-W plating bath with hydrothermal CNT exhibited increased current density from near -900 mV. The addition of hydrothermal treated CNT in Ni-W plating bath shifted the deposition potential of Ni-W to a more cathodic value. At the initial step of the deposition, CNT is anticipated to be adsorbed onto cathode surface. Adsorption of composite materials or plating additives on cathode surface can inhibit the deposition reaction and can increase the electrodeposition overvoltage [24,25]. Although CNT has good electric conductivity, the absorption of CNT in such electrodeposition condition may occurred as parallel to the cathode. Therefore, this absorption may obstruct the electrodeposition of Ni-W alloy. This may be the reason for the shift in deposition potential of Ni-W alloy to

more cathodic potential direction. The decrease in slopes of the cathodic polarization curves along with the increase in CNT concentration of plating bath was expected to be due to the increase in CNT amount absorbed on cathode surface, leading to increased overvoltage for deposition of Ni-W alloy.

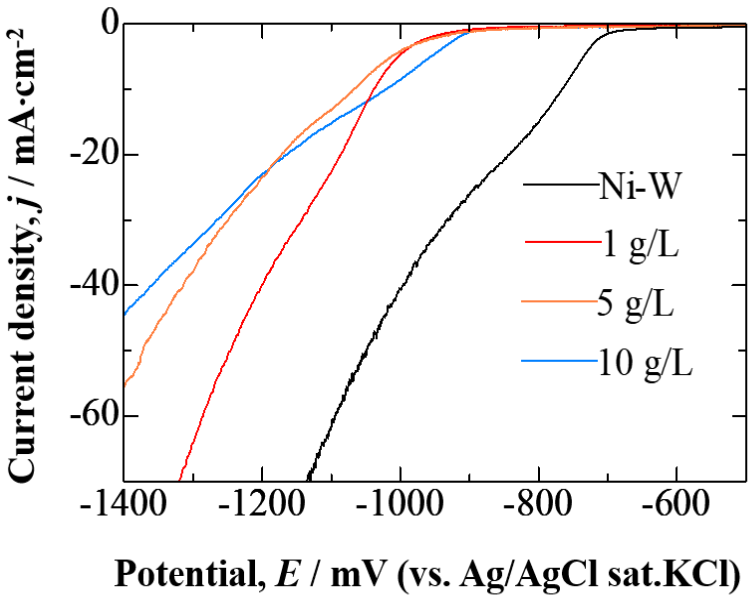

Figure 2.8 Cathodic polarization curves for Ni-W and Ni-W/CNT composite plating as CNT concentration of 1, 5 and 10 g/L. Scan rate was 5 $mV \cdot s^{-1}$ under continuous magnetic stirring at 500 rpm.

2.6.3 Electrodeposition

A HZ-5000 potentio/galvanostat was utilized for electrodeposition process. The commercial steel plates with exposed area of 2×2 cm^2 was used as cathode. A Pt coil and Ag/AgCl electrode was used as anode and auxiliary electrode, respectively. The steel plates were rinsed with ethanol for 10 sec and chemically etched with 10 wt.% H_2SO_4 solution for 10 sec before use. Constant current density of -50 $mA \cdot cm^{-2}$ with fixed coulomb amount of 25 $C \cdot cm^{-2}$ was applied for electrodeposition. Continuous magnetic agitation at 500 rpm was conducted to inhibit aggregation of CNT in plating bath during electrodeposition process. Hereafter, Ni-W/CNT composite plating specimens deposited using plating bath with hydrothermal treated

CNT of 1, 5 or 10 g/L is denoted as Ni-W/CNT 1 g/L, Ni-W/CNT 5 g/L or Ni-W/CNT 10 g/L, respectively. The bath composition is presented in Table 2.5.

Table 2.5 Bath compositions for Ni-W and Ni-W/CNT composite plating.

Regent	**Concentration**
$(NH_4)_3C_6H_5O_7$	0.3 mol/L
$Na_2WO_4 \cdot 2H_2O$	0.2 mol/L
$NiSO_4 \cdot 6H_2O$	0.1 mol/L
CNT (Hydrothermal treated)	0, 1, 5 and 10 g/L
Temperature	40 °C
Adjusted pH	7.0

2.7 Characterization of Ni-W/CNT composite plating

2.7.1 Morphology and crystalline structure analysis

Surface microstructures of Ni-W plating and Ni-W/CNT composite plating were observed by using FE-SEM. The elemental composition of deposited plating was analyzed by EDS. The crystalline phases of plating were analyzed using XRD equipped with a Cu-Kα radiation source (λ = 0.154056 nm). The measurement range, scanning speed, accelerating voltage and accelerating current were $20° \leq 2\theta \leq 80°$, 2.0°/min, 40 kV and 30 mA, respectively.

Figure 2.9 shows the optical photographs along with the surface FE-SEM micrographs for Ni-W and Ni-W/CNT composite plating with various CNT addition amount. Ni-W plating presented a metallic luster plating appearance (Figure 2.9 (a-1)) and fine morphology (Figure 2.9 (a-2)). As CNT concentration in Ni-W plating bath increased, metallic luster at plating surface gradually disappeared. In the Ni-W/CNT 1 g/L specimens, metallic luster was only partially confirmed (Figure 2.9 (b-1)). Ni-W/CNT 5 g/L and Ni-W/CNT 10 g/L showed no metallic luster. The reason why the distribution of CNT at the surface of Ni-W/CNT 1 g/L was non-uniform is considered to be due to the insufficient concentration of CNT in plating bath. It was anticipated that the required CNT concentration of plating bath for depositing uniform Ni-W/CNT matrix was 10 g/L. The incorporation of CNT to Ni-W plating formed particles of around 1 μm or less onto the plating surface observed by SEM images. The number of these particles on plating surface increased as the concentration of CNT in plating bath increased. CNTs could be observed near these particles for Ni-W/CNT composite plating prepared with CNT concentration of 5 g/L (Figure 2.9 (c-2)) and 10 g/L (Figure 2.9 (d-2)).

In the CNT concentration of 1 and 5 g/L, uniform plating could not be obtained, and non-metallic luster areas were mainly presented at the edge of plating surface. SEM images shown in Figure 2.10 shows that CNT was incorporated into non-metallic luster areas of Ni-W plating. The cross-sectional SEM images of Fig. 2.11 and Fig. 2.12 also show that the surface roughness increases as the CNT concentration in plating bath increases, and the CNT dispersed in the plating layer also increase. If the plating surface is uneven due to insufficient incorporation of CNT into the plating,

corrosion acceleration may be induced due to the formation of partial macro corrosion cell. Therefore, CNT concentration of 10 g/L was considered as the optimal plating condition.

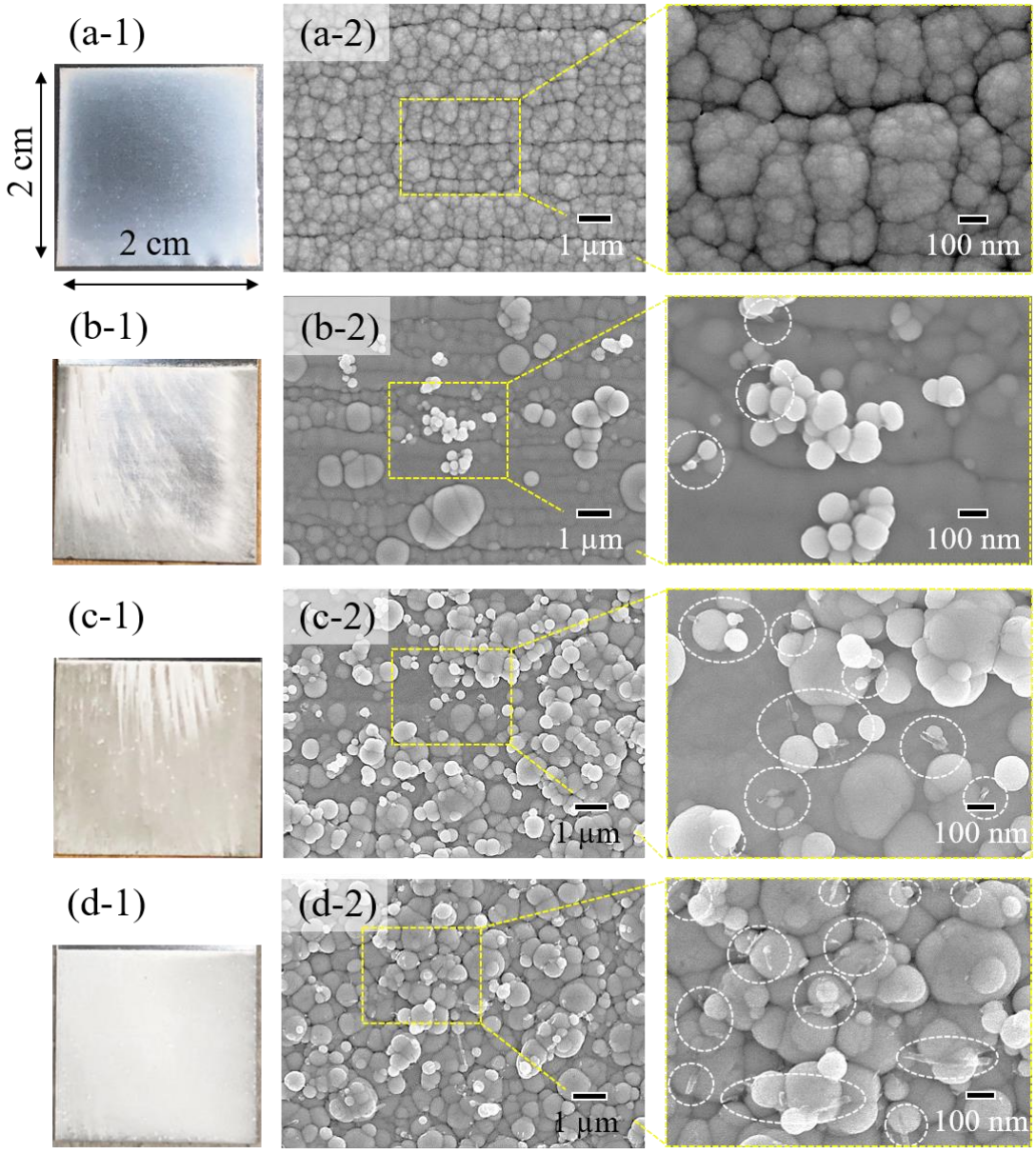

Figure 2.9 Optical photographs and surface SEM images: (a) Ni-W plating, (b) Ni-W/CNT 1 g/L, (c) Ni-W/CNT 5 g/L and (d) Ni-W/CNT 10 g/L.

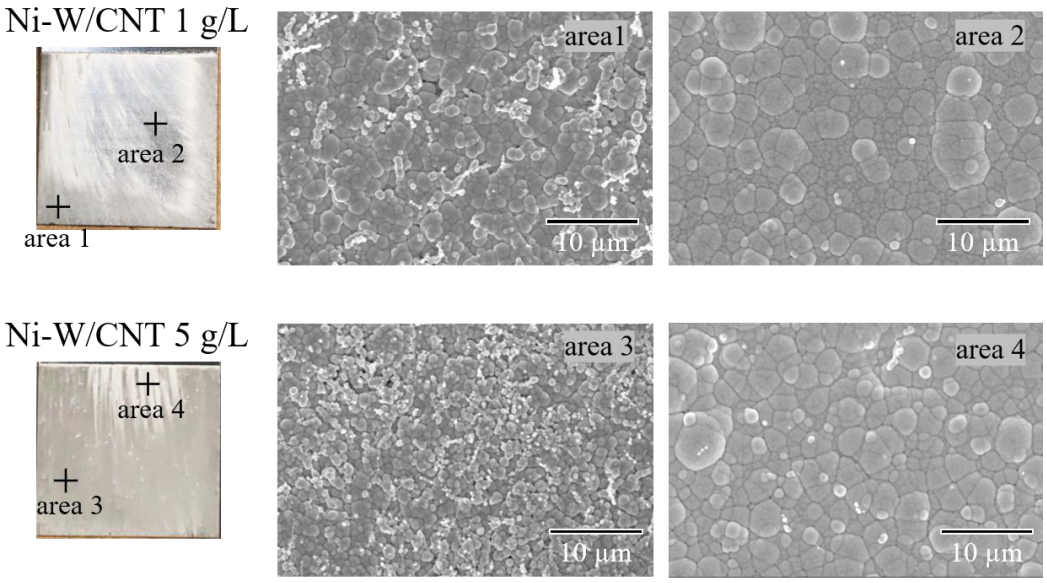

Figure 2.10 Optical photographs and surface SEM images for Ni-W/CNT 1 g/L and Ni-W/CNT 5 g/L.

The increases of surface roughness of Ni-W plating by CNT incorporation also can be observed in the cross-sectional SEM images presented in Figure 2.11.

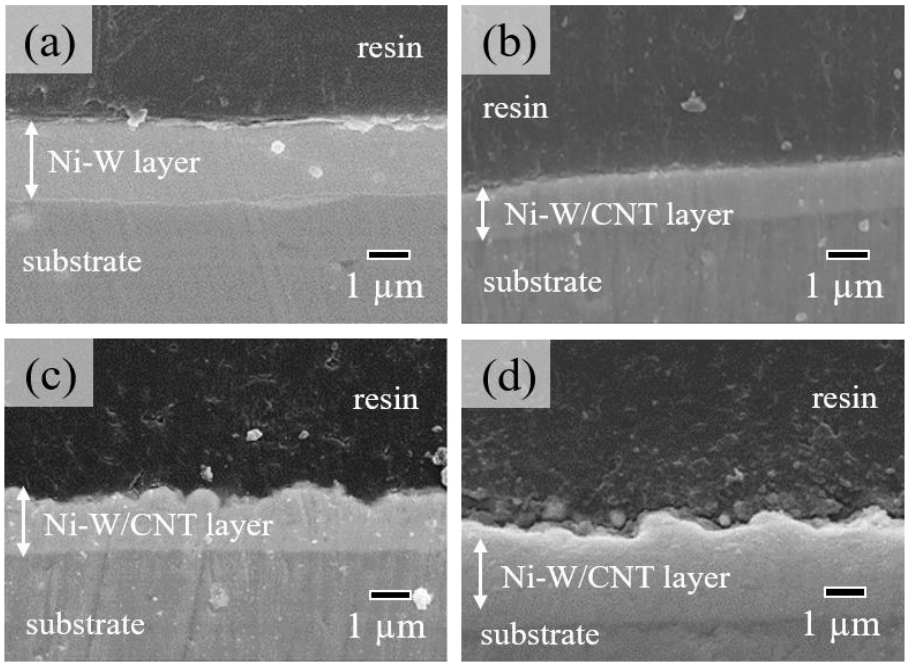

Figure 2.11 Cross-sectional SEM micrographs: (a) Ni-W plating, (b) Ni-W/CNT 1 g/L, (c) Ni-W/CNT 5 g/L and (d) Ni-W/CNT 10 g/L.

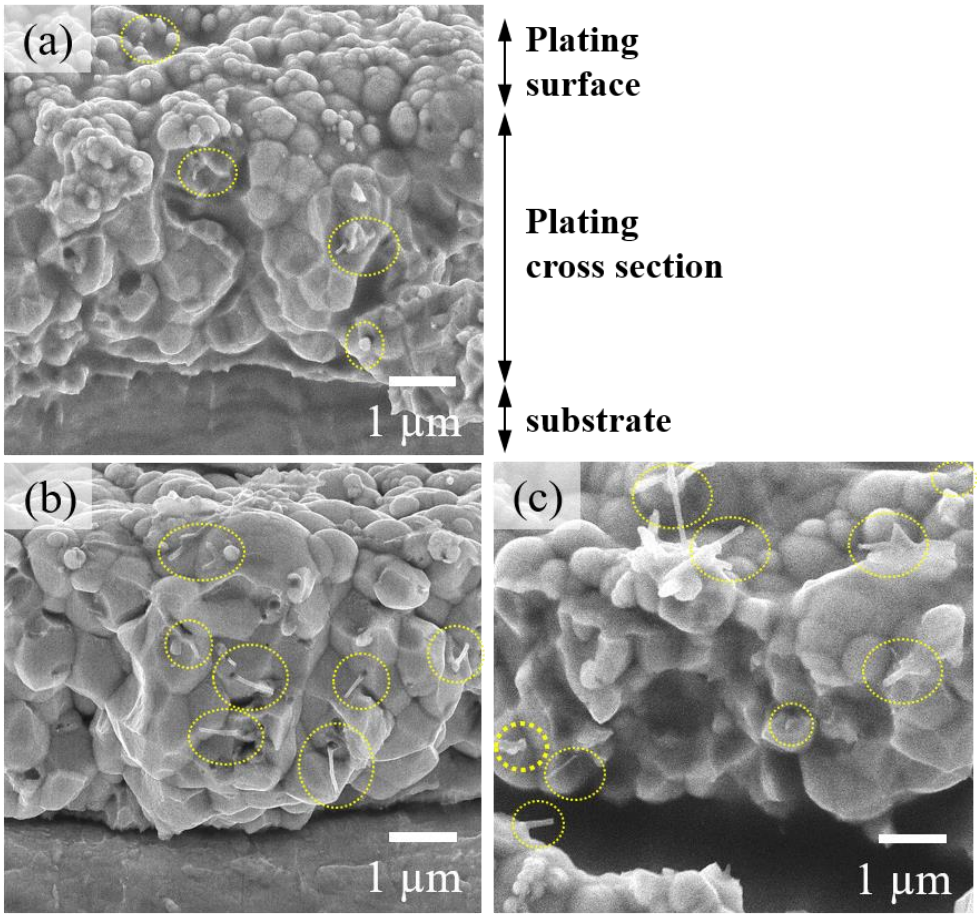

Figure 2.12 SEM micrographs of fractured cross-section of composite plating : (a) Ni-W/CNT 1 g/L, (b) Ni-W/CNT 5 g/L and (c) Ni-W/CNT 10 g/L.

Elemental composition and crystalline structure of Ni-W and Ni-W/CNT 10 g/L were analyzed by EDS and XRD, respectively. The W content of the Ni-W plating was about 15.2 at.% and that of Ni-W/CNT 10 g/L exhibited the similar content of 15.0 at.%. Normally, the W content of binary Ni-W plating is influenced by various plating parameters such as bath temperature, pH and current density [26,27]. It was assumed that no significant difference in the W content of both plating was caused by the same plating conditions (bath temperature, pH and current density).

The X-ray diffractograms for Ni-W and Ni-W/CNT 10 g/L are presented in Figure 2.13. The FCC-structured Ni-W peaks, corresponding to (111), (200) and (220) at near 2θ= 44, 50 and 75° [28], respectively were confirmed at both Ni-W and Ni-W/CNT 10 g/L. The intensity of these Ni-W peaks decreases in Ni-W/CNT 10 g/L

compared to Ni-W plating. The incorporation of CNT to Ni-W alloy structure may cause the refinement in crystal size, which is considered to be due to the increased electrodeposition overvoltage of the Ni-W alloy by the addition of CNT in the plating bath [29].

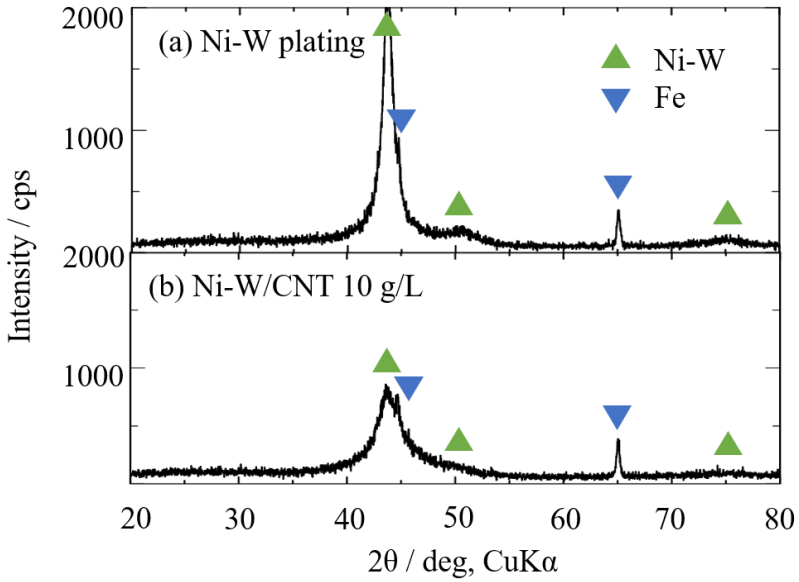

Figure 2.13 X-ray diffractograms for (a) Ni-W plating and (b) Ni-W/CNT 10 g/L.

2.7.2 Carbon content measurement

The incorporated CNT amount in the composite plating was calculated by measuring the carbon content in the composite plating using carbon-sulfur analyze equipment [30,31]. Plating specimens containing carbon were burned in an oxygen-containing atmosphere and quantified by measuring formed carbon monoxide or dioxide with infrared adsorption method. The carbon mass of the plating specimen M_c (g) was calculated as mass.%. M_c (g) of the plating specimen is calculated as follows:

$$M_c = \frac{M_v \times M_f}{100} \quad (2.3)$$

where, M_v is the measured carbon mass value from carbon/sulfur analyzer and M_f is the mass of the plating specimen (g). The carbon content, C_c (mass.%) of the plating specimen can be calculated by using the equation as follows:

$$C_c = \frac{M_c}{M_p} \times 100 \quad (2.4)$$

where, M_p is the mass of plating specimen (g). Measurement of carbon content of plating specimen was conducted at least 2 times for each deposition condition.

The carbon contents of the prepared platings are shown in Figure 2.14. The Ni-W plating exhibited the carbon content of 0.02 mass.%. Ni-W/CNT 1 g/L specimen exhibited 0.22 mass.% of carbon content, which was nearly 8 times than that of composite platings prepared with non-treated CNT 1 g/L (carbon content 0.03 mass.%). This result shows the surface modification of CNT by hydrothermal treatment had a great influence on the amount of CNT incorporation to Ni-W plating. With the increase of the concentration of hydrothermal treated CNT, the carbon content in the composite plating increased proportionally, showing a maximum content of 0.33 mass.% in the case of 10 g/L.

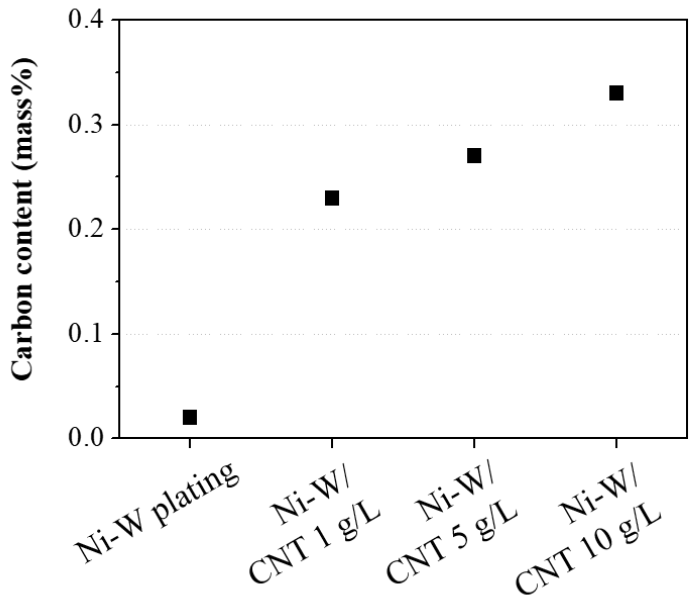

Figure 2.14 Carbon content of plating specimens measured by EMIA-510 carbon-sulfur analysis apparatus.

2.7.3 Proposed layer growth mechanism

Figure 2.15 shows a proposed schematic diagram of the layer-growth model for Ni-W/CNT composite plating in this study. In early step of composite plating, the CNT is absorbed onto the cathode substrate. The local current density at cathode surface may be high in areas where CNT was absorbed. This causes the preferential reduction of Ni-W alloy close to absorbed CNT, results in irregular and granular shaped morphology. At high CNT concentration in plating bath, the sites of the locally high current density on the cathode surface increase and the particles may increase, causing rough plating surface. Because the CNT protruding at the plating surface is a part where the oxide film of the Ni-W plating is not existed, it is considered that the electric conductivity of Ni-W/CNT composite plating can be enhanced by configuring a conductive pathway.

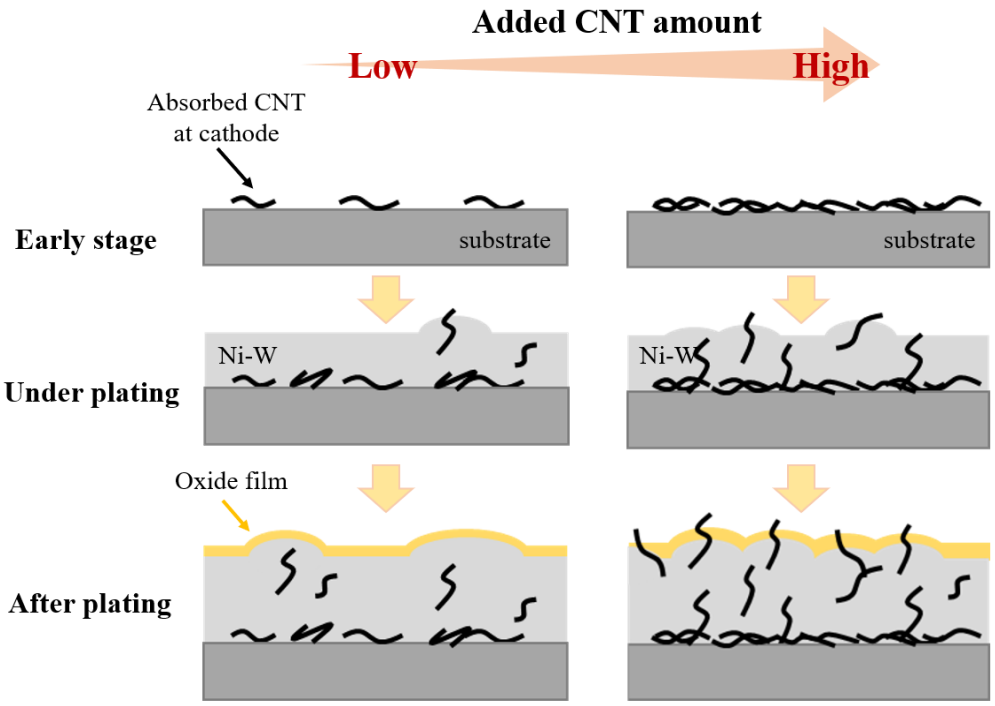

Figure 2.15 Schematic illustrations of the layer growth model for Ni-W/CNT composite plating as a function of CNT concentration in plating bath.

2.8 Contact resistance measurement

Contact resistance of plating specimens was measured by using 4-probe contact resistance measurement apparatus. The plating specimens for measurement were deposited on steel plate of 2×2 cm^2 dimension with coating thickness of approximately 3 μm. The measured contact resistance of Ni plating (deposited using Watts Ni bath), Ni-W plating and Ni-W/CNT 10 g/L composite plating were measured. The average value of 5 measurements in different points for each specimen was calculated.

Figure. 2.16 presents the measured contact resistance of Ni plating, Ni-W plating and Ni-W/CNT 10 g/L composite plating.

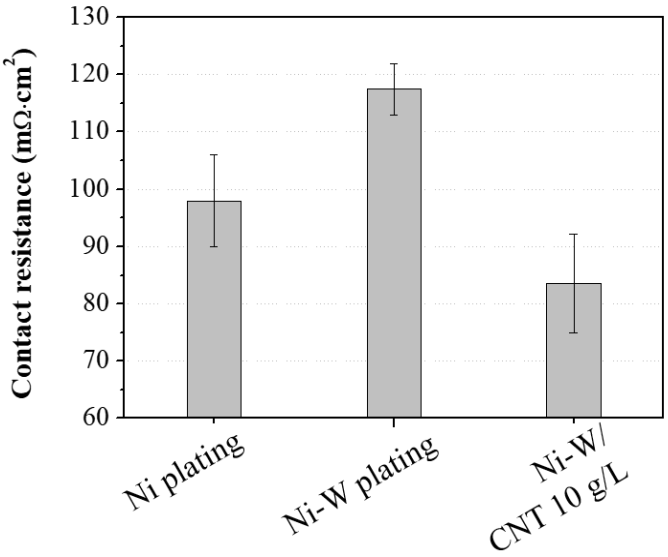

Figure 2.16 Measured contact resistance of Ni plating, Ni-W plating and Ni-W/CNT 10 g/L specimens by 4-probe contact resistance measurement apparatus. (Measurement number: 5 different areas for each specimen).

Since the Ni-W/CNT 1 g/L and Ni-W/CNT 5 g/L exhibited non-uniformed plating appearance, contact resistance measurement for Ni-W/CNT composite platings was conducted only for the Ni-W/CNT 10 g/L, which shows uniform plating appearance and CNT distribution. Ni-W plating exhibited higher contact resistance of average 117.5 mΩ·cm^2, which is a little higher than that of Ni plating (average: 98.0 mΩ·cm^2). Increased contact resistance in Ni-W plating was possibly due to the

formation of tungsten oxide (WO_3) on plating surface, which can increase the contact resistance than Ni plating. This value was close to that of austenitic stainless steel, which is widely used as the base metal material of bipolar plate for PEMFC [5,32]. However, Ni-W/CNT 10 g/L exhibited an average contact resistance of 83.6 $m\Omega \cdot cm^2$, which is approximately 30 and 15 % lower than that of Ni-W plating and Ni plating, respectively. The contact resistance of the Ni-W/CNT 10 g/L was possibly decreased by incorporation of highly conductive CNT into metal plating layer [33]. Considering the relationship between the measured contact resistance and proposed layer growth process of the Ni-W/CNT composite plating, the following assumption can be suggested. At the early stage of electrodeposition, CNT was adsorbed horizontally on the cathode surface. During the plating process, the incorporation of CNT into plating layer can varied in various directions because CNT was included in the plating layer at the same times as it contacts the cathode surface. Therefore, when concentration of CNT in plating bath was sufficiently high, there are sufficient CNT that were vertically incorporated in the plating layer and serve as an appropriate conductive pathway between the inside and surface oxide layer of the Ni-W plating layer, resulting in lower contact resistance than pristine Ni-W plating.

2.9 Corrosion test

2.9.1 Anodic polarization measurement

Considering the acidic corrosion environment of PEMFC, anodic polarization measurements were performed in 100 ml of 0.5M H_2SO_4 solution at room temperature for evaluating the corrosion resistance of plating specimens [18]. The area for polarization measurement was fixed to 1×1 cm^2 by masking with insulating tape. Polarization parameters, the corrosion potential (E_{corr}) and corrosion current density (I_{corr}) of plating specimens were calculated by Tafel's extrapolation method. Polarization measurement was conducted as a scan rate of 1 $mV \cdot s^{-1}$ from -0.4 V (vs. OCP) to +2.0 V (vs. Ag/AgCl) range. The open circuit potential (OCP) of plating specimens were stabilized before conducting measurement at least 30 min.

Measured anodic polarization curves are plotted in Figure 2.17 All plating specimens showed a typical active-passivation-trans passive behaviors. The I_{corr} of Ni-W plating was 76.13 $\mu A \cdot cm^{-2}$, which is similar values with that of Ni plating (77.62 $\mu A \cdot cm^{-2}$). However, Ni-W/CNT composite plating exhibited lower I_{corr} (40.78 $\mu A \cdot cm^{-2}$) than that of Ni-W and Ni plating.

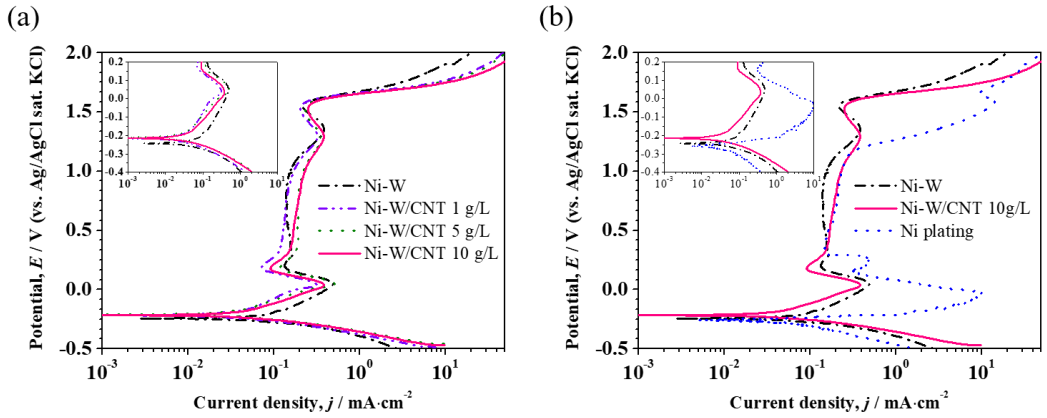

Figure 2.17 Measured anodic polarization curves at 0.5M H_2SO_4 solution: (a) Ni-W and Ni-W/CNT composite plating with various CNT concentration and (b) comparison with Ni plating.

This result indicates that the incorporation of CNT into Ni-W plating was effective to improve the corrosion resistance. Since carbon materials are has high corrosion resistance, the incorporation of this CNT into Ni-W plating layer may be effective in

decreasing the I_{corr} of composite plating. In addition, it was confirmed that the E_{corr} of the plating shifts to the noble potential direction because of the incorporation of CNT into Ni-W plating layer. Additional polarization measurement was performed to confirm the effect of the CNT concentration in plating bath to improving the corrosion resistance, and the obtained polarization parameters are shown in the Figure 2.18 presented below. The CNT content in the composite plating can be expected to increase as the CNT concentration in the plating bath increase as shown in Figure 2.14 of the manuscript. Therefore, perhaps the corrosion resistance might be further improved as the CNT content in the composite plating increased. When the CNT concentration increased up to 1 g/L, E_{corr} increased proportionally and I_{corr} decreased significantly compared to Ni-W plating. However, when the CNT concentration in the plating bath reached 1 g/L or more, the variation of E_{corr} and I_{corr} of the Ni-W/CNT composite plating seemed to reach a plateau.

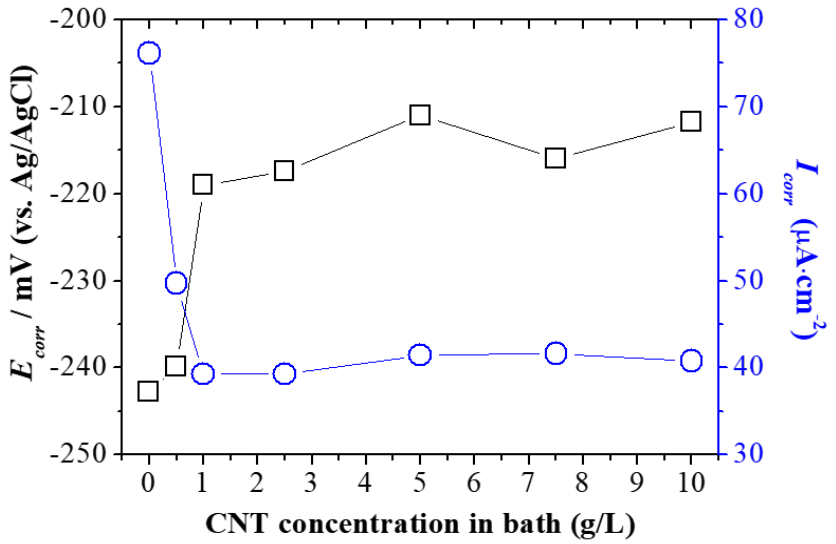

Figure 2.18 Measured polarization test parameters, E_{corr} and I_{corr} as CNT concentration in plating bath.

The reason for this may be because increased CNT content in the plating layer cause surface roughening and enlarged the specific surface area (shown in Figure 2.9), which increases the contact area with corrosive solution and can increase the corrosion rate of coating. The amount of CNT prominent at the composite plating surface may

increase owing to the increase of the CNT amount in the composite plating, However, the area of the exposed Ni-W plating can also enlarge as the surface roughness increases. For this reason, it is estimated that the corrosion resistance can be further increased by realizing both small surface roughness and high CNT content in the plating.

2.9.2 Acid immersion test

The acid immersion test was conducted for verifying the corrosion resistance of plating specimens at the similar acidic environment of PEMFC operation. The dissolution amount of metal ions eluted from plating was measured as by ICP-AES as various immersion times. Plating samples exposing area of 1×1 cm^2 were immersed in 50 mL of 0.5M sulfuric acid solution with temperature kept at 80 °C. The concentration of eluted amount of metal ions in corrosion test solution was measured by ICP-AES. SEM observation, EDS elemental analysis and XRD measurements were conducted after the immersion test for observing corrosion progression of Ni-W composite plating.

Measured ICP-AES results are shown in Figure 2.19 The dissolution amount of Ni ion from Ni plating was higher than that of Ni-W plating and Ni-W/CNT 10 g/L. This seems reached a plateau after 3 h of immersion times, which may be caused by rapid corrosion of Ni plating within a short time. However, the Ni dissolution amount from Ni-W plating and Ni-W/CNT 10 g/L showed further low value than that of Ni plating. And the dissolution rate of Ni ion from Ni-W and Ni-W/CNT 10 g/L gradually increased as immersion times. However, W ion was hardly detected at both plating until 12 h. Since tungsten oxide (WO_3) is stable under acidic pH, the W in Ni-W and Ni-W/CNT composite plating hardly eluted and may have remained as WO_3 on the surface of plating. In the Ni-W and Ni-W/CNT composite plating, the selective elution of Ni ions was confirmed in common. Similar phenomenon of selective elution of Ni ions from Ni-based Ni-Mo and Ni-Mo-P alloy plating in acidic environment has been reported [32].

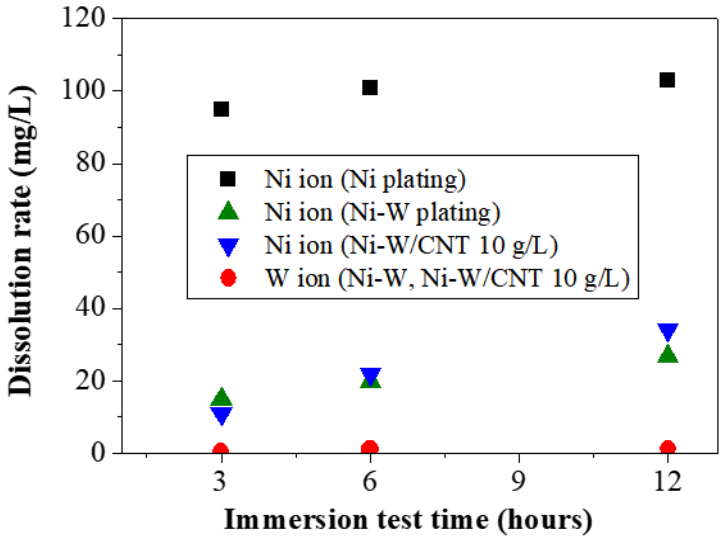

Figure 2.19 Measured dissolution amount of Ni and W ions as immersion test times by ICP-AES.

2.9.3 Analysis of coating after corrosion test

XRD measurement was conducted to confirm the formed corrosion products during acid immersion test. X-ray diffractograms for Ni-W and Ni-W CNT 10 g/L after 3 h of immersion test are presented in Figure 2.20.

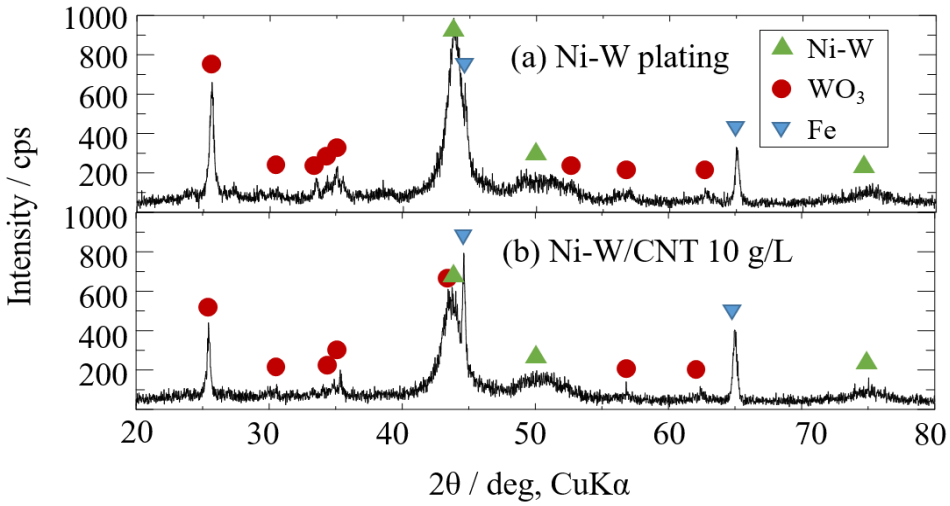

Figure 2.20 X-ray diffractograms for (a) Ni-W plating and (b) Ni-W/CNT 10 g/L after 3 h of immersion test.

The WO_3 peaks were detected in both plating specimens, which corresponds to the formation of corrosion product of W in Ni-W plating. The ICP-AES results showed only Ni ion were gradually eluted from the Ni-W plating and the XRD measurement result verifies W remained in the plating layer as WO_3 over immersion times.

The variation of surface morphology of Ni-W/CNT 10 g/L according to immersion test are presented in Figure 2.21. Globular-shaped particles of plating surface gradually transformed to more angled shape as corrosion progressed. When the Ni-W/CNT composite plating started to corrode, Ni ion gradually eluted and W remained as WO_3 at the surface. Thus, thus angled shape layer was considered to be the remaining WO_3 layer. EDS elemental mapping and point-analysis results of outside and inside of the crack appeared in 6 hours of immersion test are presented in Figure 2.21(d). Elemental composition of the inside of the cracked portion showed similar results (75.71 at.% Ni, 11.30 at.% W) with Ni-W plating before the corrosion, which correspond the remained uncorroded Ni-W/CNT composite plating layer.

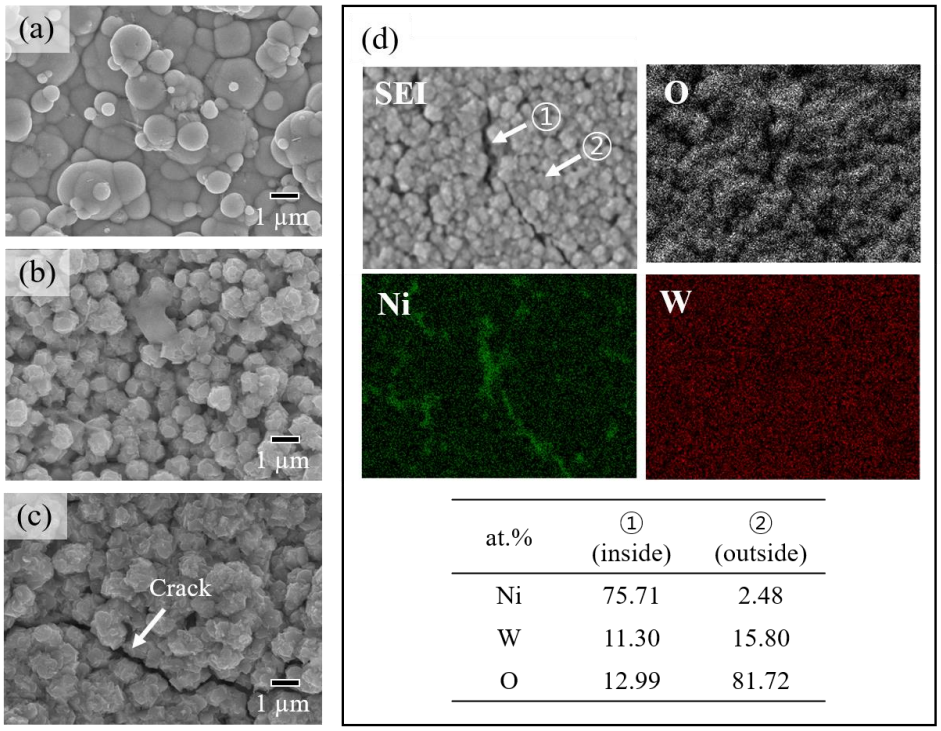

at.%	① (inside)	② (outside)
Ni	75.71	2.48
W	11.30	15.80
O	12.99	81.72

Figure 2.21 Observation results for corrosion progress of Ni-W/CNT 10 g/L according to immersion test times: (a) SEM image before immersion test, (b) after 3h, (c) after 6h and (d) EDS map analysis result after immersion test 6 h.

But at the outside portion of the crack, Ni was hardly detected (2.48 at.%) and W and O were found as the main component. Formed WO_3 layer seems to contribute to enhancing corrosion resistance by retarding corrosion progress of underlying Ni-W/CNT plating; however, suppression in cracks seemed to be a remaining issue. Furthermore, it should be considered that the WO_3 layer formed by corrosion of Ni-W/CNT plating has the potential to increase the contact resistance [34], thus the existence of conductive pathway by CNT is of importance.

Cross-sectional SEM images with EDS line analysis results of Ni-W/CNT 10 g/L after 6 h of immersion test are shown in Figure 2.22. About 1μm thickness of WO_3 layer existed on the top surface and uncorroded Ni-W/CNT composite layer was remaining underneath. The elemental distribution of Ni showed a lower intensity at outmost surface of WO_3 layer. The concentration gradient of Ni ions proves that Ni ions were gradually eluted from the outermost surface of the plating. The distribution of C was high between the WO_3 layer and remained Ni-W/CNT composite plating layer, which is assumed to be due to the remaining CNT together with WO_3 film.

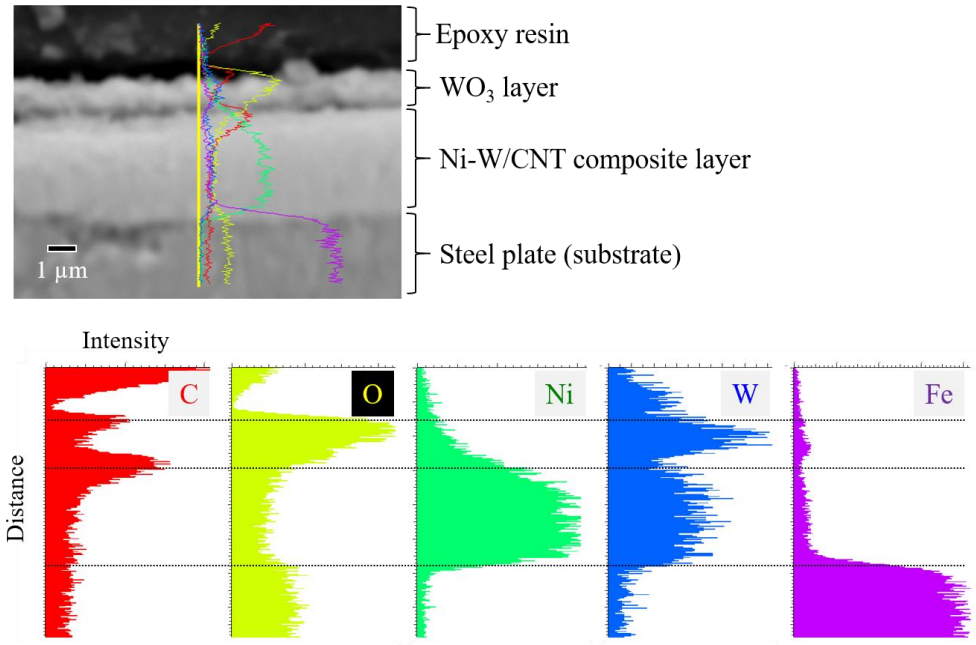

Figure 2.22 Cross-sectional SEM image with EDS line analysis result after immersion test 6 h.

2.10 Conclusion

In this research, Ni-W/CNT composite plating was prepared onto steel plate by electrodeposition and the potential of Ni-W/CNT composite plating as a new candidate coating for bipolar plate of PEMFC was examined from the perspective of contact resistance and corrosion resistance.

Hydrophobic CNT can be well dispersed in plating bath by hydrothermal treatment in mixed acid solution, and uniform Ni-W/CNT composite plating with low contact resistance and improved corrosion resistance were obtained when the sufficient concentration of CNT (10 g/L) was added in plating bath. The conductive pathway formed by incorporating conductive CNT into the Ni-W plating lowered the contact resistance of the plating by about 30% from 117.5 to 83.6 on average. Also, corrosion test results confirmed that the incorporation of CNT into Ni-W plating enhanced corrosion resistance. The addition of CNT was effective in lowering the corrosion current density of composite plating; however, the corrosion resistance was not improved in proportion to the CNT addition amount. It is considered that the corrosion resistance is determined by the surface structural as well as the CNT composite amount of the composite plating.

In this study, the properties of the platings could be improved by structural control of plating by alloying of W with Ni and incorporation of inert CNT. The two approaches were found to be effective in enhancing the corrosion resistance while preserving the electrical conductivity. Although further improvement is still necessary, electrodeposited Ni-W/CNT composite plating were shown to be a possible coating material for PEMFC bipolar plate.

References

[1] D.A. Boysen, T. Uda, C.R.I. Chisholm, S.M. Haile, High-performance solid acid fuel cells through humidity stabilization, Science. 303 (2004) 68–70.

[2] R.W. Lashway, Fuel cells: the next evolution, MRS Bull. 30 (2005) 581–586.

[3] D.P. Davies, P.L. Adcock, M. Turpin, S.J. Rowen, Bipolar plate materials for solid polymer fuel cells, J. Appl. Electrochem. 30 (2000) 101–105.

[4] K.S. Dhathathreyan, N. Rajalakshmi, Polymer electrolyte membrane fuel cell, in: Recent Trends Fuel Cell Sci. Technol., Springer, 2007

[5] N. De Las Heras, E.P.L. Roberts, R. Langton, D.R. Hodgson, A review of metal separator plate materials suitable for automotive PEM fuel cells, Energy Environ. Sci. 2 (2009) 206–214.

[6] 西川尚男, 燃料電池の技術: 固体高分子形の課題と対策, 東京電機大学出版局, 2010.

[7] H. Tawfik, Y. Hung, D. Mahajan, Metal bipolar plates for PEM fuel cell—a review, J. Power Sources. 163 (2007) 755–767.

[8] V.O. Mittal, H.R. Kunz, J.M. Fenton, Membrane degradation mechanisms in PEMFCs, J. Electrochem. Soc. 154 (2007) 652.

[9] R. Singh, P.C. Sui, K.H. Wong, E. Kjeang, S. Knights, N. Djilali, Modeling the effect of chemical membrane degradation on PEMFC performance, J. Electrochem. Soc. 165 (2018) 3328.

[10] H. Wang, M.A. Sweikart, J.A. Turner, Stainless steel as bipolar plate material for polymer electrolyte membrane fuel cells, J. Power Sources. 115 (2003) 243–251.

[11] R.C. Makkus, A.H.H. Janssen, F.A. de Bruijn, R.K.A.M. Mallant, Stainless steel for cost-competitive bipolar plates in PEMFCs, Fuel Cells Bull. 3 (2000) 5–9.

[12] S.A.A. El-Enin, O.E. Abdel-Salam, H. El-Abd, A.M. Amin, New electroplated aluminum bipolar plate for PEM fuel cell, J. Power Sources. 177 (2008) 131–136.

[13] C.-H. Lin, S.-Y. Tsai, An investigation of coated aluminium bipolar plates for PEMFC, Appl. Energy. 100 (2012) 87–92.

[14] D. Zhang, L. Duan, L. Guo, Z. Wang, J. Zhao, W.-H. Tuan, K. Niihara, TiN-coated titanium as the bipolar plate for PEMFC by multi-arc ion plating, Int. J. Hydrogen Energy. 36 (2011) 9155–9161.

[15] S.-H. Wang, J. Peng, W.-B. Lui, J.-S. Zhang, Performance of the gold-plated titanium bipolar plates for the light weight PEM fuel cells, J. Power Sources. 162 (2006) 486–491.

[16] R. Tian, J. Sun, L. Wang, Plasma-nitrided austenitic stainless steel 316L as bipolar plate for PEMFC, Int. J. Hydrogen Energy. 31 (2006) 1874–1878.

[17] D.-H. Han, W.-H. Hong, H.S. Choi, J.J. Lee, Inductively coupled plasma nitriding of chromium electroplated AISI 316L stainless steel for PEMFC bipolar plate, Int. J. Hydrogen Energy. 34 (2009) 2387–2395.

[18] S.-J. Lee, C.-H. Huang, Y.-P. Chen, Investigation of PVD coating on corrosion resistance of metallic bipolar plates in PEM fuel cell, J. Mater. Process. Technol. 140 (2003) 688–693.

[19] W.-Y. Ho, H.-J. Pan, C.-L. Chang, D.-Y. Wang, J.J. Hwang, Corrosion and electrical properties of multi-layered coatings on stainless steel for PEMFC bipolar plate applications, Surf. Coatings Technol. 202 (2007) 1297–1301.

[20] A.E. Fetohi, R.M.A. Hameed, K.M. El-Khatib, E.R. Souaya, Ni–P and Ni–Co–P coated aluminum alloy 5251 substrates as metallic bipolar plates for PEM fuel cell applications, Int. J. Hydrogen Energy. 37 (2012) 7677–7688.

[21] S.A. Gamboa, J.G. Gonzalez-Rodriguez, E. Valenzuela, B. Campillo, P.J. Sebastian, A. Reyes-Rojas, Evaluation of the corrosion resistance of Ni–Co–B coatings in simulated PEMFC environment, Electrochim. Acta. 51 (2006) 4045–4051.

[22] Y. Fu, M. Hou, H. Xu, Z. Hou, P. Ming, Z. Shao, B. Yi, Ag–polytetrafluoroethylene composite coating on stainless steel as bipolar plate of proton exchange membrane fuel cell, J. Power Sources. 182 (2008) 580–584.

[23] S.-H. Wang, J. Peng, W.-B. Lui, Surface modification and development of titanium bipolar plates for PEM fuel cells, J. Power Sources. 160 (2006) 485–489.

[24] S. Arai, T. Saito, M. Endo, Cu–MWCNT composite films fabricated by electrodeposition, J. Electrochem. Soc. 157 (2010) 147–153.

[25] L. Shi, C.F. Sun, P. Gao, F. Zhou, W.M. Liu, Electrodeposition and characterization of Ni–Co–carbon nanotubes composite coatings, Surf. Coatings Technol. 200 (2006) 4870–4875.

[26] K.A. Kumar, G.P. Kalaignan, V.S. Muralidharan, Pulse electrodeposition and characterization of nano Ni–W alloy deposits, Appl. Surf. Sci. 259 (2012) 231–237.

[27] N.P. Wasekar, N. Hebalkar, A. Jyothirmayi, B. Lavakumar, M. Ramakrishna, G. Sundararajan, Influence of pulse parameters on the mechanical properties and electrochemical corrosion behavior of electrodeposited Ni-W alloy coatings with high tungsten content, Corros. Sci. 165 (2020) 108409.

[28] R. Juškėnas, I. Valsiūnas, V. Pakštas, R. Giraitis, On the state of W in electrodeposited Ni–W alloys, Electrochim. Acta. 54 (2009) 2616–2620.

[29] Y. Fan, Y. He, P. Luo, T. Shi, H. Li, Pulse current electrodeposition and characterization of Ni-W-MWCNTs nanocomposite coatings, J. Electrochem. Soc. 162 (2015) 270.

[30] Y. Goto, Y. Kamebuchi, T. Hagio, Y. Kamimoto, R. Ichino, T. Bessho, Electrodeposition of copper/carbonous nanomaterial composite coatings for heat-dissipation materials, Coatings. 8 (2018) 5.

[31] Y. Kamimoto, S. Okura, T. Hagio, T. Wada, H. Tanaka, H. Hara, P. Deevanhxay, R. Ichino, Nickel–carbon composite plating using a Watts nickel electroplating bath, SN Appl. Sci. 2 (2020) 170.

[32] N.F. Asri, T. Husaini, A.B. Sulong, E.H. Majlan, W.R.W. Daud, Coating of stainless steel and titanium bipolar plates for anticorrosion in PEMFC: A review, Int. J. Hydrogen Energy. 42 (2017) 9135–9148.

[33] A. Oluwalowo, N. Nguyen, S. Zhang, J.G. Park, R. Liang, Electrical and thermal conductivity improvement of carbon nanotube and silver composites, Carbon. 146 (2019) 224–231.

[34] L. Mendizabal, A. Oedegaard, O.E. Kongstein, S. Lædre, J. Walmsley, J. Barriga, J.J. Gonzalez, TaNX coatings deposited by HPPMS on SS316L bipolar plates for polymer electrolyte membrane fuel cells: Correlation between corrosion current, contact resistance and barrier oxide film formation, Int. J. Hydrogen Energy. 42 (2017) 3259–3270.

CHAPTER 3

Electrodeposition of a novel ternary Fe-W-Zn alloy plating: improvement of corrosion properties of binary Fe-W alloy by Zn addition

3.1 Background of this research

3.1.1 Needs for replacement of Cr plating

3.1.1.1 Cr plating

Cr platings are corrosion resistive coating that have been widely used in numerous applications such as engine parts, pistons, cylinder and decorative for various automotive parts because of their excellent properties, such as high hardness, low friction coefficient, high corrosion resistance and fine appearance [1]. The features of Cr plating are summarized as follows:

1. It has a glossy appearance with a silvery white and hardly corroded by forming a passive film (Cr_2O_3) in the air.
2. The highest hardness of 800 to 1,100 Hv among the metal plating.
3. High wear resistance and low friction coefficient.
4. High corrosion resistance

In general, baths for Cr plating distinguished to hexavalent chromium (Cr^{6+}) plating bath and trivalent chromium (Cr^{3+}) plating bath, but Cr^{6+} plating bath is mainly used for industrial applications because Cr^{3+} plating is difficult to obtain thick plating and management of plating bath is also more complicate than that of Cr^{6+} plating bath. As for the Cr^{6+} plating bath, the Sargent bath, which composed as chromium (VI) oxide (CrO_3) and sulfuric acid (H_2SO_4) has been widely used, which was invented by G.T. Sargent in 1920 [1]. And recently, various baths such as fluoride bath and porous chrome plating bath have been developed and used.

3.1.1.2 Needs for alternative plating

In spite of superior properties of Cr plating, the use of Cr^{6+} is gradually becoming restricted in industrial fields owing to its harmfulness to humans [2,3]. The ELV (End of Life Vehicle) directive issued by the European Union in 2007 restricted the use of heavy metals, including Cd, Pb, Hg and Cr^{6+} in automobiles. And RoHS (Restriction of Hazardous Substance) directive pronounced in 2006 also restricted the use of 6 hazardous substance, Hg, Pb, Cd, Cr^{6+}, PBB (polybrominated biphenyls) and PBDE (polybrominated diphenyl ether) [4]. Accordingly, the need to develop alternative plating that can replace the existing Cr^{6+} plating is increasing.

As a possible alternative coating for harmful Cr^{6+} plating, various types of plating, iron group-metals based plating alloyed with other refractory metals, such as Mo and W are considered as promising and appropriate plating for replacement of Cr plating from the viewpoint of mechanical, thermal and corrosion properties [5-8]. These alloys can be electrodeposited in aqueous solution with iron-group element, based on the principle of induced codeposition, as previously introduced. Among them, increased attention has been paid to the electrodeposited W-based alloy, such as binary Ni-W [9-12], Fe-W [13,14], Co-W [15,16] and ternary Ni-Fe-W [17-23] plating. These alloy platings offer advanced various properties such as high hardness, wear resistance, thermal stability and corrosion resistance. Among these platings, Ni-W alloy plating is the most intensively studied and anticipated as a possible alternative for hard Cr plating. The hardness of the as-deposited Ni-W alloy plating is in the range of 500 to 700 Hv, while heat treated Ni-W plating showed further increased hardness to near 1,200 Hv due to the precipitation hardening. Nevertheless, Ni has been recently reported as a major factor in triggering skin allergies to humans, and eluted Ni ion can trigger skin inflammation [24-26]. Therefore, the needs for replacement of Ni are increased owing to restriction of harmful element and also environmental issues. Therefore, the development of harmless and environmentally friendly plating is great interest.

3.1.2 Binary Fe-W alloy plating

3.1.2.1 Properties and applications

As described above, the development of harmless and environmental-friendly plating materials is increasingly required. In this perspective, Fe-based W alloy plating is of great interest. Fe is a metal that has abundant, affordable and does not cause environmental problems, but plating materials using Fe have insufficient corrosion resistance. Electrodeposited binary Fe-W alloy plating has some superior properties, such as high hardness and thermal properties. Different with Cr plating which hardness decrease gradually at temperature above 400 °C [8], the hardness of binary Fe-W alloy plating is retained or even further increased close to 1,200 Hv at high temperature, possibly due to the formation of stable intermetallic phase (Fe_2W) [27,28]. Considering the operating thermal condition of Cr plating, thermal stability is considered as an important property along with corrosion resistance. In addition, the abrasion resistance of Fe-W alloy plating is similar to that of Cr plating, so it is considered as a possible alternative for harmful Cr^{6+} plating.

3.1.2.2 Electrodeposition of Fe-W alloy

According to the classification of alloy plating, Fe-W alloy plating is classified as induced codeposition typed alloy. This induced codeposition is a phenomenon in which elements such as W and Mo, which are difficult to electrodeposited alone in an aqueous solution, are codeposited as an alloy through electrodeposition with iron-group metals such as Fe, Ni and Co in a plating bath. In the past, various studies have focused on the electrodeposition of binary Ni-W and Co-W alloy plating [9-12,15,16], while the research on electrodeposition of binary Fe-W alloy plating are still scarce. However, it is considered that the electrodeposition mechanism may be similar to the that of Ni-W alloy. Therefore, it is necessary to understand the electrodeposition mechanism of Fe-W alloy plating based on the known mechanism of Ni-W alloy plating.

As a plating bath for Ni-W alloys, several types of baths using organic acids as a complexing agent have been reported. Among them, many studies have been focused on citric acid-ammonia baths that can expect high W content deposits.

However, proposed electrodeposition mechanism of Ni-W alloys deposited in citric acid-ammonia bath are not absolute results, but conjectured results obtained through trial and error based on obtained experimental results. The following describes the recently announced research results about the proposed electrodeposition mechanism of Ni-W alloys in citrate-ammonia bath.

3.1.2.2.1 Complexing agent

Many metal ions in solution form complex ions by coordination bonds with one or more chemical species groups (called ligands or complexing agents). In a practical metal plating baths, various complexing agents are utilized to enhance the quality and property of the deposits, in particular to prepare smooth and metallic bright deposits. Until the 20th century, cyanide was widely used for complexing agent for metal deposition such as Au, Ag, Cu, Ni, Co, Zn and Cd. Even though cyanide was most satisfactory from the perspective of engineering, the use of it was gradually abandoned because of environmental considerations. Therefore, cyanide has been gradually replaced by other complexing agents, mostly organic poly-acids, such as citrate, malate, oxalate, etc. The main purpose of formation of metal-complex ions is to slow down the kinetics of the deposition reaction. This normally leads to improvement in the uniformity and enhancement of smoothness and brightness of obtained deposits.

Figure 3.1 shows the molecular structure of citric acid, which is a commonly used complexing agent and Figure 3.2 shows speciation diagrams for citric acid and citrate-metal complexes taking Ni as an example. Citrate ions can exist in aqueous solution as the neutral molecular or negative ions carrying a charge of 1 to 4, depending on bath pH. The purpose of using the citrate or other complexing agent is to form a stable metal-complexes and prevent the deposition of metal hydroxides. The corresponding pK_a values are presented in Table 3.1. In the pH range of 7 to 10, the predominant species of citric acid is triple-charged anion, Cit^{3-} ($C_6H_5O_7^{3-}$). The distribution of Cit-Ni complexes as a function of citrate concentration at bath pH of 8.0 is shown in Figure 3.2(b). The corresponding log(β_n) values, where β_n correspond to the equilibrium constants for the reaction are presented in Table 3.1. The concentration of Ni^{2+} ion decreases, and almost to zero when concentration ratio

become to Cit/Ni = 1. As concentration of citrate increase further, $[Ni(Cit)_2]^{4-}$ becomes predominant species, which is very stable, and electrodeposition of Ni from this is strongly suppressed. Thus, although citrate is a useful complexing agent for plating baths, a large stoichiometric excess can be detrimental to performance of plating process. Ammonia is also often added to plating bath to increase current efficiency and pH adjustment. NH_3 can form metal-NH_3 complexes with most transition metals. For example, Ni forms NH_3 complexes of $[(Ni)(NH_3)_n]^{2+}$ (where, n = 1 to 6). And, because the stability constant for each complex is known, the relative concentrations of all complexes can be calculated.

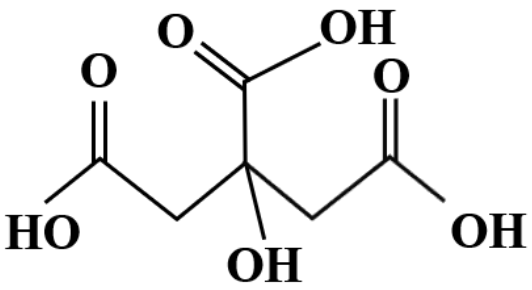

Figure 3.1 Molecular structure of citric acid.

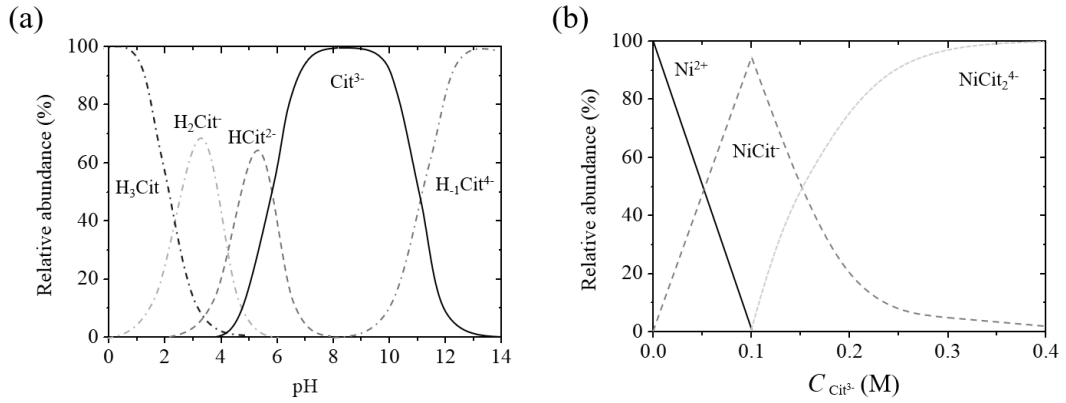

Figure 3.2 Speciation diagrams for citric acid and citrate-metal complexes: (a) deprotonation of citric acid as a bath pH and (b) concentration distribution of Cit-Ni complexes as various concentration of citrate (pH 8.0, 0.1M of $NiSO_4$) [29,30].

Table 3.1 Equilibrium constants for citric acid, ammonium ion and each of Ni complexes.

Species/Complex	pK_a	log(β_n)	Ref.
$[(H)_n(Cit)]^{-(3-n)}$	pK_1 = 2.96	log(β_1) = 2.96	[29]
	pK_2 = 4.38	log(β_2) = 7.34	
	pK_3 = 5.68	log(β_3) = 13.02	
	pK_4 = 10.82	log(β_4) = 23.84	
$Ni(Cit)_n^{-(3n-2)}$	pK_1 = 5.50	log(β_1) = 5.50	[30]
	pK_2 = 2.30	log(β_2) = 7.80	
$[Ni(NH_3)_n]^{2+}$	pK_1 = 2.80	log(β_1) = 2.80	[31]
	pK_2 = 2.24	log(β_2) = 5.04	
	pK_3 = 1.73	log(β_3) = 6.77	
	pK_4 = 1.19	log(β_4) = 7.96	
	pK_5 = 0.75	log(β_5) = 8.71	
	pK_6 = 0.03	log(β_6) = 8.74	
NH_4^+ / NH_3	pK_1 = 9.25	log(β_1) = 9.25	[29]

3.1.2.2.1 Electrodeposition mechanism

Until now, various studies have been conducted on the electrodeposition of binary Ni-W alloy plating, especially plating bath using citric acid as a complexing agent. Citric acid can exist as various forms depending on pH. The forms of complexes of citrate and tungstate ions depending on bath pH and relative concentrations of tungstate and citrate ions as follows [32]:

$$[(WO_4)_k(Cit)_l(H)_m]^{-(2k+3l-m)} \qquad (3.1)$$

The corresponding log(βn) for complexes are given in Table 3.2 presented below.

Table 3.2 Equilibrium constants for citrate-tungstate complexes.

Species/Complex	pK_a	log(β_n)	Ref.
$[(WO_4)(Cit)(H)_m]^{-(5-m)}$	pK_1 = 4.64	log(β_1) = 4.64	[32]
	pK_2 = 6.82	log(β_2) = 11.45	
	pK_3 = 10.21	log(β_3) = 21.67	

Gileadi and coworkers reported the induced codeposition of Ni-W alloy containing citrate as a complexing agent [33,34]. They suggest the following hypothesis from the results:

1. A citrate-tungstate complex ion reacts with a citrate-nickel complex, forming a mixed-metal complex, $[(Ni)(HWO_4)(Cit)]^{2-}$.
2. $[(Ni)(HWO_4)(Cit)]^{2-}$ act as the deposition precursor for the Ni-W alloy.
3. W can only be deposited from the mixed-metal complex, Ni can be deposited from citrate-nickel complex and also from ammonia-nickel complexes; $[Ni(NH)_3]^{2+}$, where n= 1 to 6.

Though there is no direct evidence for the formation of the mentioned mixed-metal complex ion, the following experimental results support the suggested assumption that this mixed-metal complex is indeed formed and serves as the deposition precursor for electrodeposition of Ni-W alloy.

1. The mutual synergistic effect of each Ni^{2+} and WO_4^{2-} was observed, where increasing the concentration of either metal ions in plating bath increases the partial current density of the other.
2. The W content of the alloy increase when removing ammonia.
3. The W content of the alloy deposits drastically decreases as the bath pH over 8.0.

Figure 3.3 shows the calculated relative abundance of citrate-tungstate complex ions as a function of bath pH. According to this, the predominant species is $[(WO_4)(Cit)(H)_1]^{-4}$ (mentioned as $[1,1,1]^{4-}$) in the pH range of 7.0 to 9.0. It is assumed that this complex is the deposition precursor of the formation of the as mentioned mixed-metal complex with citrate-Ni complex, $[(Ni)(HWO_4)(Cit)]^{2-}$ as following reaction:

$$[(WO_4)(Cit)(H)]^{4-} + [(Ni)(Cit)]^{-} \rightarrow [(Ni)(HWO_4)(Cit)]^{2-} + Cit^{3-} \quad (3.2)$$

When the bath pH is further increased, $[1,1,1]^{4-}$ becomes deprotonated. As a result, the concentration of mixed-metal complex in bath decreased and consequently W content of the deposits decrease. The electrodeposition of Ni-W alloy from mixed-metal complex can be occurred as follows:

$$[(Ni)(HWO_4)(Cit)]^{2-} + 8e^- + 3H_2O \rightarrow NiW + 7(OH)^- + Cit^{3-} \qquad (3.3)$$

In ammoniacal citrate baths, Ni^{2+} can also form complex ions with NH_3, of the form $[Ni(NH_3)_n]^{2+}$, where n= 1 to 6. The log(βn) for these complex ions is presented in Table 3.1. The formation of these complex ions can lead to lower concentration of other Ni^{2+} complexes, including mixed-metal complex, $[(Ni)(HWO_4)(Cit)]^{2-}$. Consequently, the W content of deposited Ni-W alloy decreased. Therefore, the W content in Ni-W alloy plating deposited in ammoniacal citrate bath could not exceed 25 at.%. This indirectly implies the electrodeposition of Ni from Ni-NH_3 complexes is faster than that of citrate-Ni complexes.

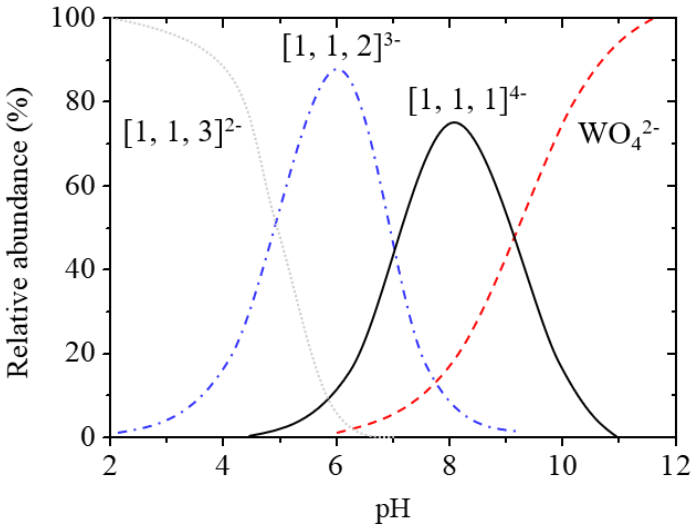

Figure 3.3 The relative abundance of citrate-tungstate complexes at $[Cit^{3-}]/[WO_4^{2-}]= 1$ according to Younes et al [34]. $[1, 1, x]^{x-5}$ indicates $[(WO_4)(Cit)(H)_x]^{x-5}$, and x is number of protons.

3.1.2.3 Problems in electrodeposition process

The problems on electrodeposition of binary Fe-W alloy plating are usually associated with low faraday efficiency. This could be attributed to the oxidation of Fe^{2+} to Fe^{3+} and higher cathodic polarization of deposition for Fe-W alloy (about -1.00 V), which results in a higher partial current density for hydrogen evolution reaction [13]. Therefore, the current efficiency of electrodeposited Fe-W alloy plating did not exceed 35 % [6]. Normally, the baths for Fe-W alloy platings use complexing agent to forma mixed-metal complexes. However, organic complexing agent may be decomposed at the insoluble anode during the plating process [35,36]. In addition, oxidation of Fe^{2+} in plating bath to Fe^{3+} gradually proceeds due to the generated oxygen at the insoluble anode [37,38]. This causes degradation of plating bath by insufficient formation of stable-state metal-citrate complex ions, which causes the precipitation of metal-hydroxides in alkaline bath and degrades the stability of the plating bath. Therefore, development of a plating process that can prevent both oxidation of Fe ions and decomposition of complexing agents at the insoluble anode is required.

3.2 Proposed structure design of plating

In accordance with the strict regulations on the use of harmful Cr^{6+} in industry, the need to prepare a new plating that can replace Cr plating has emerged. Ni-W alloy plating was considered as a promising alternative for Cr plating, but the use of Ni is also gradually becoming avoided owing to environmental issues and harmfulness to the human body. Therefore, we paid attention to the Fe-W alloy plating, which uses Fe: an affordable, harmless and eco-friendly element. However, despite its strongpoints such as excellent mechanical and thermal properties at high W contents, the Fe-W alloy has insufficient corrosion resistance. To overcome this issue, we tried to improve the corrosion resistance through the design of the plating structure by incorporating the third element. The addition of third element was expected to be effective in improving corrosion resistance by refining the crystalline size and transforming the Fe-W alloy structure with columnar structure to more dense structure. Generally, noble elements are selected as the additional element to increase corrosion resistance; however, a base element was selected from the viewpoint of structure control and protection of Fe. The selected third element is Zn, which can act as a sacrificial anode for Fe. By incorporating Zn into binary Fe-W alloy plating, a challenge to improve the corrosion resistance of iron-based alloys is carried out. The graphical overview of the designed plating structure is shown in Figure 3.4.

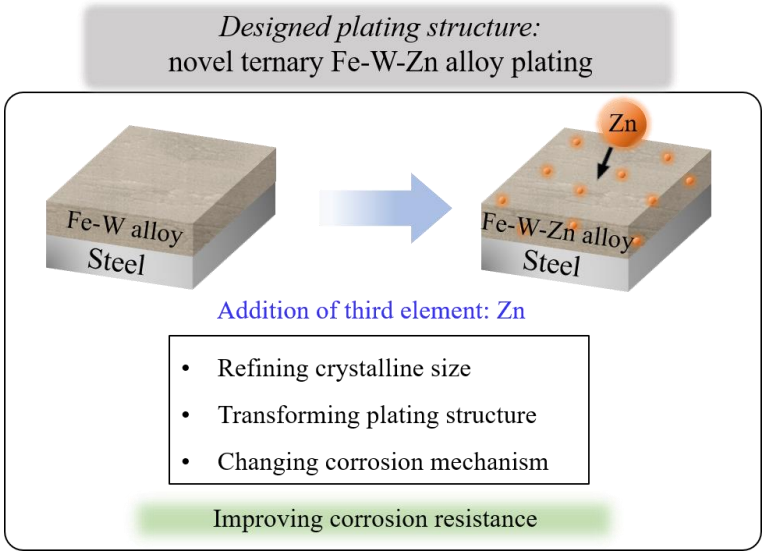

Figure 3.4 The graphical overview of the designed plating structure.

3.3 Objective of this work

This study aims to prepare a novel ternary Fe-W-Zn plating that improves the corrosion resistance of binary Fe-W alloy plating. The effect of improving corrosion properties by the structural change of the binary Fe-W plating with Zn addition is investigated.

The influence of the Zn addition to the electrodeposition behavior of binary Fe-W alloy system is examined and discussed to understand the underlying mechanism. Since the electrodeposition of binary Fe-W alloy is obtained from a mixed-metal complex with citrate ions by induced codeposition, ammonia was further added to form Zn-ammonia complex ion in separate for electrodeposition of Zn, and the effect was investigated. Through the elemental composition analysis and observation of the structure of the electrodeposited Fe-W-Zn alloy, the effect of the Zn addition on the structural change of the Fe-W alloy plating was investigated.

The corrosion resistance of ternary alloy plating is evaluated, and the plating structure with improved corrosion resistance are investigated to optimum the Zn content. Corrosion resistance of ternary alloy plating was compared with binary Fe-W and Ni-W alloy plating and the possibility of electrodeposited ternary Fe-W-Zn plating as an alternative plating for hard Cr and Ni-W plating are discussed.

3.4 Materials, chemicals, and equipment

Materials, chemicals and equipment used in this study are listed in Table 3.3 and 3.4, respectively. All chemicals were used as purchased without any further purifications.

Table 3.3 Materials and chemicals

Materials and chemicals	Company
Tri-sodium citrate ($Na_3C_6H_5O_7$, ≥ 99.0%)	Nacalai Tesque, Inc, Japan
Iron (II) sulfate heptahydrate ($FeSO_4 \cdot 7H_2O$, ≥ 99.0%)	Nacalai Tesque, Inc, Japan
Sodium tungstate dihydrate ($Na_2WO_4 \cdot 2H_2O$, ≥ 98.0%)	Nacalai Tesque, Inc, Japan
Zinc sulfate heptahydrate ($ZnSO_4 \cdot 7H_2O$, ≥ 99.5%)	Nacalai Tesque, Inc, Japan
Ammonium sulfate ($(NH_4)_2SO_4$, ≥ 99.0%)	Nacalai Tesque, Inc, Japan
Sulfuric acid (H_2SO_4, 98.0%)	Nacalai Tesque, Inc, Japan
Sodium hydroxide (NaOH, ≥ 97.0%)	Nacalai Tesque, Inc, Japan
Sodium chloride (NaCl, ≥ 99.0%)	Nacalai Tesque, Inc, Japan
Cation exchange membrane (Nafion ® NRE-212)	Dupont, USA
Commercial copper plate (B-60-P05, 99%)	Yamamoto-MS Co., Japan
Commercial steel plate (B-60-P01)	Yamamoto-MS Co., Japan
Commercial nickel plate (NI-313381, 99%)	Nilaco., Japan

Table 3.4 Equipment

Equipment	Details	Company
Potentio/galvanostat	SP-150	Bio-Logic, France
Electrochemical quartz crystal microbalance (EQCM)	HQ-601DK	Hokuto denko, Japan
Scanning electron microscope (SEM)	JSM-6330F	JEOL, Japan
Energy-dispersive spectroscopy (EDS)	SEM-EDX Type N	Hitachi, Japan
X-ray diffractometer (XRD)	RINT2500TTR	Rigaku, Japan
X-ray photoelectron spectroscope (XPS)	ESCALAB 250Xi	Thermo Fisher Scientific, USA

3.5 Electrodeposition of ternary Fe-W-Zn plating

3.5.1 Bath preparation

Plating baths for ternary Fe-W-Zn alloys were prepared with 0.26M of $Na_3C_6H_5O_7$, 0.8M of $(NH_4)_2SO_4$, 0.01M of $ZnSO_4 \cdot 7H_2O$, 0.2M of $FeSO_4 \cdot 7H_2O$ and 0.05M of $Na_2WO_4 \cdot 2H_2O$. Temperature of plating bath was kept at 80 °C with water bath during plating process. The volume of the bath was set to 200 ml and pH was controlled to 8.0 by using sulfuric acid and sodium hydroxide.

3.5.2 Application of anodic chamber

Normally, baths for Fe-W alloy platings use citrate ions (Cit^{3-}) as a complexing agent for iron and tungstate ions [39-41]. However, organic complexing agent may be decomposed at the insoluble anode during the plating process [35,36]. In addition, oxidation of Fe^{2+} in plating bath to Fe^{3+} gradually proceeds due to the generated oxygen at the insoluble anode. This causes degradation of plating bath by insufficient formation of stable metal-citrate complex ions, which causes the precipitation of metal hydroxides in alkaline plating bath and degrades the stability of the plating bath. In iron and iron-based alloy plating, chemical additives such as ascorbic acid or extra plating additives are often used for avoiding the oxidation problem of iron ion [42]. However, the use of plating additives such as grain refiner, brightener and stress reliver were avoided to minimizing the effect of other chemicals on the electrodeposition of ternary Fe-W-Zn plating. To avoid possible problems to occur, an anode chamber was adapted instead of the aforementioned techniques. Separation of the anode and plating solution by an anode chamber prevents the decomposition of organic complexing agent at the anode, and also delays the oxidation of Fe^{2+}. A commercially available cation-exchange membrane was applied and the electrolyte for anode room was a diluted H_2SO_4 solution. By this method, metal ions and organic complexing agents in plating solution cannot reach the anode because only protons can penetrate from the anode room to the plating solution. The schematic illustration of plating system equipped with anode chamber is shown in Figure 3.5.

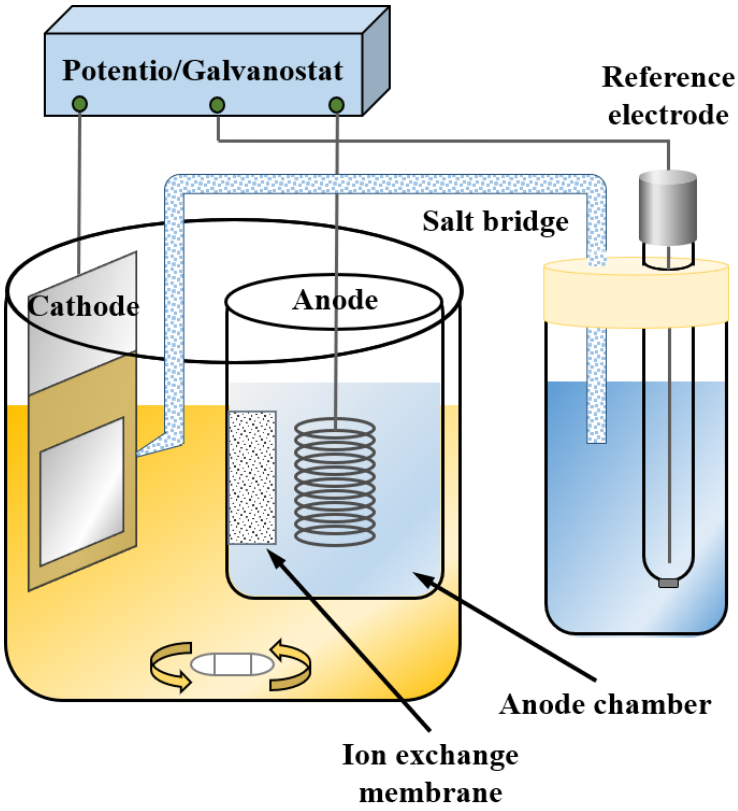

Figure 3.5 Schematic illustration of plating system equipped with anode chamber used in this study.

3.5.3 Cyclic voltammetry (CV) and EQCM measurement

The electrodeposition behaviors of ternary alloys were studied by CV. The measurements were performed using a SP-150, Bio-Logic potentio/galvanostat. Typical 3-electrode electrochemical measurement systems were used for the measurement. A commercially available Cu sheet with a surface area of 1×1 cm^2 as a working electrode (W.E.), Platinum coil as a counter electrode (C.E.) and Ag/AgCl electrode were used as auxiliary electrode (R.E.). The Cu sheet was etched with 8 wt.% nitric acid (HNO_3) solution. The CV measurements were conducted from the open circuit potential to -1.4 V (vs. Ref.) and then reversed until -0.1 V (vs. Ref.) with scan rate of 50 $mV \cdot s^{-1}$. The plating bath compositions for CV measurements are presented in Table 3.5.

Table 3.5 Bath compositions for CV measurements.

Bath	Concentration ($mol \cdot dm^{-3}$)				
	$Na_3C_6H_5O_7$	$FeSO_4$	$ZnSO_4$	Na_2WO_4	$(NH_4)_2SO_4$
Cit–Zn	0.31	–	0.01	–	0.8
Cit–W	0.31	–	–	0.05	0.8
Cit– Fe	0.31	0.2	-	–	0.8
Cit–Fe–W	0.31	0.2	-	0.05	0.8
Cit–Fe–Zn	0.31	0.2	0.01	–	0.8
Cit–Fe–W–Zn	0.31	0.2	0.01	0.01, 0.05, 0.1	0.8

The EQCM measurements were conducted for in-situ investigation of the electrodeposition behaviors of alloys along with linear sweep voltammetry. The frequency variation (Δf) caused by the mass change (Δm) of the electrode was measured. The mass change of electrode owing to the precipitation of metal on a surface of quartz crystal induces the decrease of resonance frequency according to following Sauerbrey's equation:

$$\Delta f = -C_f \cdot \Delta m \quad (3.4)$$

Where, Δf indicates the variation in resonance frequency, Δm indicates the mass change at unit area, and C_f corresponding to the specific constants of oscillator. An Au-coated quartz crystal electrode (area: 0.07 cm^2) and resonance frequency of 10 MHz was used in this study. The scan rate of linear sweep voltammetry (LSV) was set as 20 $mV \cdot s^{-1}$.

3.5.3.1 Effect of bath composition

Figure 3.6 shows a series of cyclic voltammograms measured using each plating bath appearing in Table 3.5. Figure 3.6 (a) shows the effect of the addition of $(NH_4)_2SO_4$ in Cit-Zn bath to electrodeposition behavior of Zn. Near the pH value of 8.0, the predominant ionic state of the citrate species is Cit^{3-}, which forms a stable complex ion with Zn ions. In Cit-Zn bath without the addition of $(NH4)_2SO_4$, an increase in cathode current density was appeared near -1.2 V, which induced by the electrodeposition of metal Zn from the Cit-Zn complex, while anodic current at -1.1 to -0.8 V correspond to dissolution of metallic Zn. However, a plateau was confirmed from -1.25 to -1.4 V range, which was caused by the diffusion limitation of the Cit-Zn complex ion. This diffusion-controlled region almost disappeared by adding 0.8 $mol \cdot dm^{-3}$ of $(NH_4)_2SO_4$ to the Cit-Zn bath, and the increasement of cathodic and anodic current were also observed. Increase in the cathodic current indicates the enhanced deposition rate of metallic Zn by adding $(NH_4)_2SO_4$ in Cit-Zn bath. This is well supported by EQCM measurement results shown in Figure 3.7. EQCM results confirmed that the amount of frequency change (Δf), which correspond to mass gain at cathode was further increased in the bath with 0.8M of $(NH_4)_2SO_4$. Considering the plating bath pH and speciation diagram of ammonium ions (pK_a = 9.26) shown in Figure 3.8, a small portion of ammonia existed in NH_3 state at pH 8.0. This shall enable the formation of stable Zn-NH_3 complex ions, $[Zn(NH_3)_n]^{2+}$ (n=1 to 4). Among these complex ions, $[Zn(NH_3)_4]^{2+}$ was anticipated to be the predominant state considering the equilibrium of the Zn-NH_3-H_2O system [43]. Since the stability constant of $[Zn(NH_3)_4]^{2+}$ complex ion ($\log \beta$ = 9.34 [44]) is higher than that of possible Cit-Zn complex ions, $[Zn(Cit)]^-$ ($\log \beta$ = 5.02 [45]) and $[Zn(Cit)_2]^{4-}$ ($\log \beta$ = 6.76 [45]), Zn ion is anticipated to exist mainly as $[Zn(NH_3)_4]^{2+}$ in plating bath.

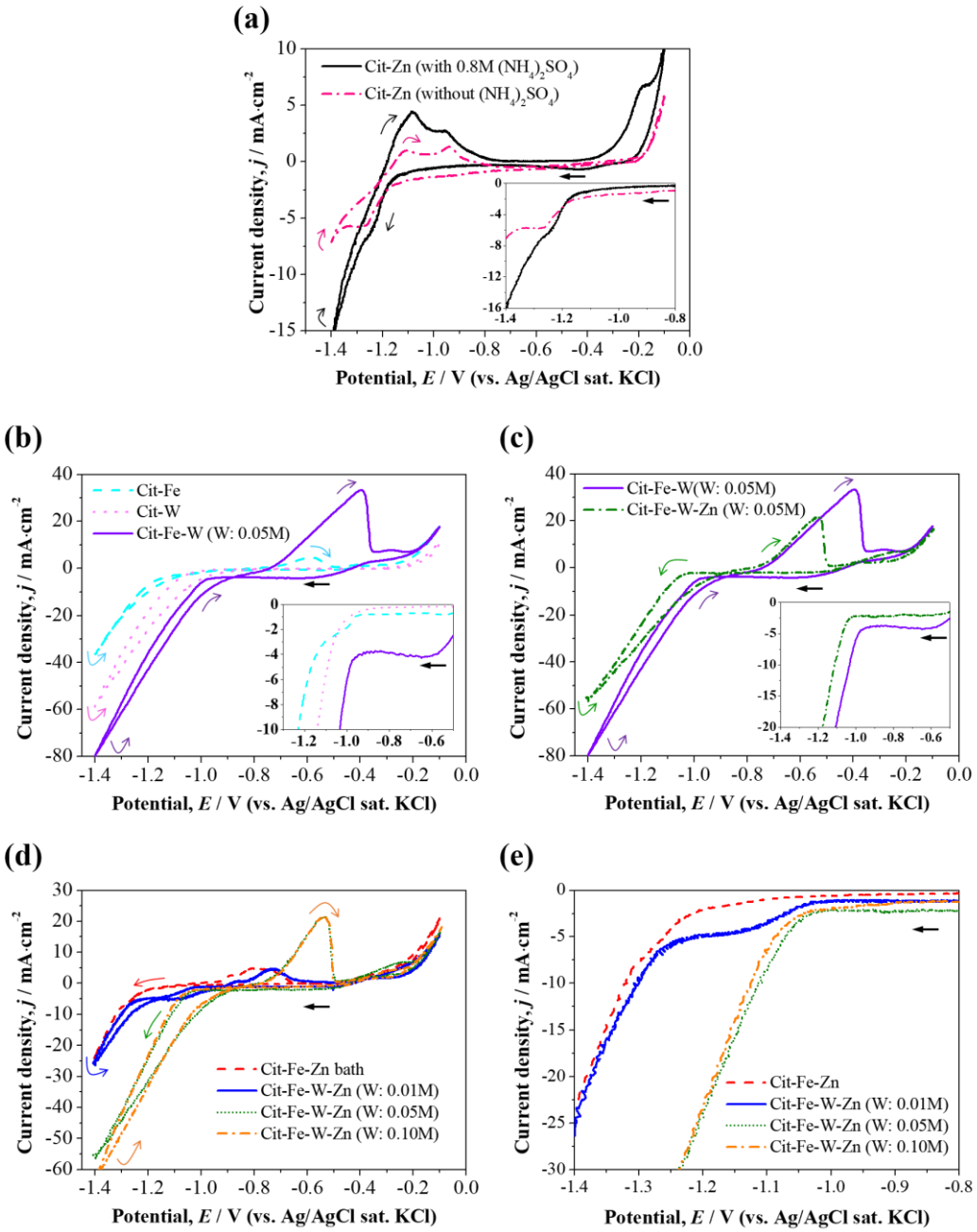

Figure 3.6 Cyclic voltammograms measured: (a) Cit-Zn bath, (b) Cit-Fe, Cit-W, and Cit-Fe-W bath, (c) effect of Zn addition on Cit-Fe-W bath, (d) effect of Na_2WO_4 in Cit-Fe-Zn bath, and (e) selective cathodic areas of (d). The scan direction is indicated as black arrows in plots. The scan rate was 50 $mV \cdot s^{-1}$.

Because the pH of 8.0 is lower than the pK_a of ammonium ions, metallic Zn from $[Zn(NH_3)_4]^{2+}$ can be electrodeposited as follows [46]:

$$[Zn(NH_3)_4]^{2+} + 4H^+ + 2e^- \rightarrow Zn + 4NH_4^+ \qquad (3.5)$$

Therefore, the formation of Zn-NH_3 complex enables Zn to be electrodeposited over a wide potential range without the diffusion-limitation.

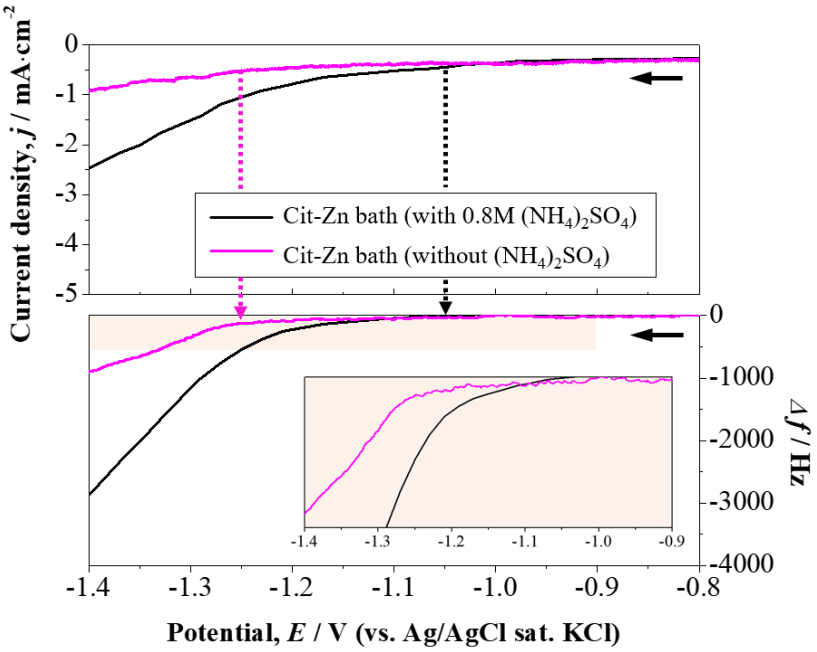

Figure 3.7 LSV curve (upper plot) and frequency variation measured by EQCM (lower plot) for Cit-Zn bath with and without addition of 0.8M of $(NH_4)_2SO_4$. The scan rate was 20 $mV \cdot s^{-1}$.

The induced codeposition of Fe-W alloy plating was confirmed by CV, as demonstrated in Figure 3.6 (b). At the Cit-Fe bath, the electrodeposition of metallic Fe from Cit-Fe complex ion, $[(Fe)(Ct)]^-$ occurred according to the following reaction.

$$[(Fe)(Cit)]^- + 2e^- \rightarrow Fe + Cit^{3-} \qquad (3.6)$$

Therefore, increased cathodic current from -1.2 V and anode current at -0.6 V was owing to the electrodeposition and dissolution of metallic iron, respectively. The addition of 0.05 $mol \cdot dm^{-3}$ $Na_2WO_4 \cdot 2H_2O$ into the Cit-Fe bath increased both cathodic and anodic current drastically, indicating that induced codeposition of Fe with W took place. Based on mechanism for the induced codepeposition of Ni-W alloy as

previously reported [47,48] and speciation diagram for Cit-WO_4^{2-} complex ion at pH 8.0 presented in Figure 3.5 [34], the induced codeposition of Fe-W alloy is likely to occur from the following reactions:

$$[(Fe)(Cit)]^{-} + [(WO_4)(Cit)(H)]^{4-} \rightarrow [(Fe)(WO_4)(Cit)(H)]^{2-} + Cit^{3-} \quad (3.7)$$

$$[(Fe)(WO_4)(Cit)(H)]^{2-} + 8e^{-} + 3H_2O \rightarrow FeW + 7(OH)^{-} + Cit^{3-} \quad (3.8)$$

Based on above-mentioned reactions, $[(Fe)(WO_4)(Cit)(H)]^{2-}$ complex ion was considered as the deposition precursor of the Fe-W alloy [48]. In addition, cathodic parts of CV curves presented in Figure 3.6 (b) showed that the induced codeposition of the Fe-W alloy start at near -1.0 V, which slightly lower than reduction potential of Fe from Cit-Fe complex. However, the anodic current peak in the CV curves of Cit-W bath did not appear, indicating that the reduction of metallic W from Cit-WO_4^{2-} complex ions (estimated as $[(WO_4)(Cit)(H)_1]^{4-}$) did not occur. Figure 3.6 (c) shows that the addition of 0.01 mol·dm^{-3} $ZnSO_4 \cdot 7H_2O$ into the Cit-Fe-W bath slightly shifts the deposition potential and peak position of anode current toward more base potential direction. Moreover, the decrease in anodic peak current indirectly implies that the existence of Zn in the plating bath inhibits the induced codeposition of Fe-W alloy. Figure 3.6 (d) and Figure 3.6 (e) demonstrate the influence of the addition amount of $Na_2WO_4 \cdot 2H_2O$ on the electrodeposition behavior of the ternary Fe-W-Zn alloy plating. As the addition amount of $Na_2WO_4 \cdot 2H_2O$ to the Cit-Fe-Zn bath increased, the CV curves gradually changed. The peak potential of anode current gradually shifted to a more noble potential direction, while the anode current significantly increased when 0.05 mol·dm^{-3} of $Na_2WO_4 \cdot 2H_2O$ was added. In the cathodic region, the addition of 0.01 mol·dm^{-3} $Na_2WO_4 \cdot 2H_2O$ to the Cit-Fe-Zn bath formed a diffusion-controlled region ranging from -1.10 to -1.25 V, as presented in Figure 3.6 (e). Meanwhile, the cathode current and this diffusion-controlled region disappeared when the $Na_2WO_4 \cdot 2H_2O$ content was increased to 0.05 mol·dm^{-3}. However, almost no further change in CV curves was observed when the $Na_2WO_4 \cdot 2H_2O$ addition amount was further increased to 0.10 mol·dm^{-3}. This results indirectly proves that the aforementioned deposition precursor necessary for the electrodeposition of Fe-W alloys, $[(Fe)(WO_4)(Cit)(H)]^{2-}$, are successfully formed when the addition amount of $Na_2WO_4 \cdot 2H_2O$ exceeds 0.05 mol·dm^{-3}.

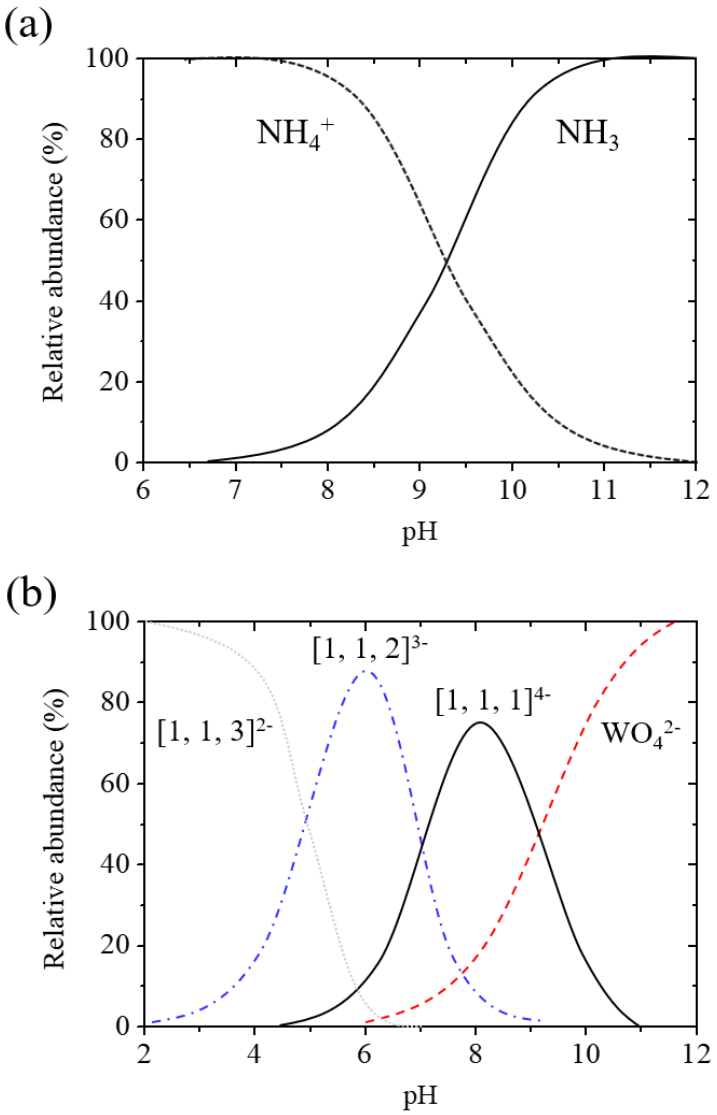

Figure 3.8 Speciation diagrams: (a) Ionization of ammonium ion ($pK_a = 9.26$) and (b) relative abundance for citrate-tungstate complexes at $[Cit^{3-}]/[WO_4^{2-}]= 1$ according to Younes et al [34]. $[1, 1, x]^{x-5}$ indicates $[(WO_4)(Cit)(H)_x]^{x-5}$, and x is number of protons.

Two feasible theories on the mechanism about the induced codeposition of Fe-W ally are derived from this result. The first is the electrodeposition of metal W does not occur via tungstate ions (WO_4^{2-}) or Cit-W complex ions, but from deposition precursor such as $[(Fe)(WO_4)(Cit)(H)]^{2-}$. The second is the ratio of complexing agent; Cit with Fe, and W ions is important for the generation of the aforementioned deposition precursor, thus determining the deposition reaction rate.

EQCM measurements were conducted along with LSV to confirm the deposition behavior more clearly. The upper plots of Figure 3.9 indicate the LSV curves, while the lower plots show the corresponding measured frequency variation (Δf). In the Cit-Zn bath with addition of 0.8 mol·dm^{-3} of $(NH_4)_2SO_4$, the electrodeposition of metal Zn from $[Zn(NH_3)_4]^{2+}$ occurred at -1.05 V. However, the deposition rate was relatively low until -1.2 V, and drastically increase at potential below -1.25 V. The induced codeposition of the binary Fe-W alloy in the Cit-Fe-W bath include 0.05 mol·dm^{-3} of $Na_2WO_4{\cdot}2H_2O$ occurred at near -1.00 V, while the electrodeposition of ternary Fe-W-Zn alloy in the Cit-Fe-W-Zn bath with 0.01 mol·dm^{-3} of $ZnSO_4{\cdot}7H_2O$ started at -1.08 V, showing that the deposition potential shifts toward the base potential direction owing to the addition of Zn in plating bath. This means the adsorption of $[Zn(NH_3)_4]^{2+}$ to the cathode inhibits the induced codeposition process of Fe-W alloy. In addition, a gap in Δf between the binary Fe-W alloy and ternary Fe-W-Zn alloy gradually increased. This means that the addition of Zn in Fe-W bath decreases the current efficiency.

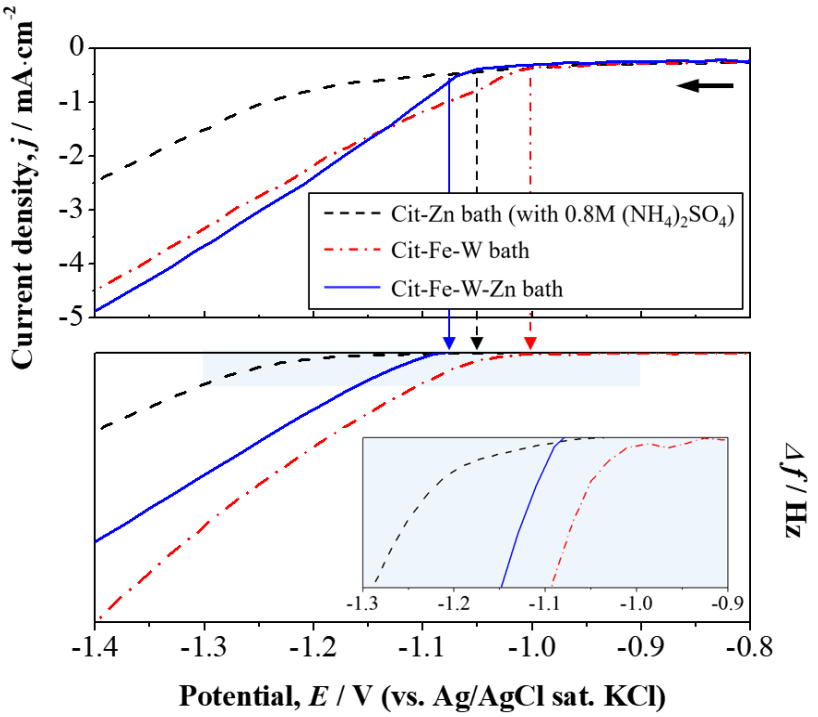

Figure 3.9 LSV curve (upper plot) and frequency variation measured by EQCM (lower plot). The scan rate was 20 mV·s^{-1}.

3.5.3.2 Effect of bath temperature

Figure. 3.10 exhibits cyclic voltammograms for Cit-Fe-W-Zn bath (W: 0.05 mol·dm^{-3}) at various bath temperatures of 20 to 80 °C. As the bath temperature increases, the anode peak position gradually shifted to noble potential direction and the anodic current also increased. It has been reported that the induced codeposition of W occurs more actively at the higher current densities, higher bath temperatures and higher concentrations of tungstate ions [13,38]. In the electrodeposition process of iron-group metal-W alloys, increasing the plating bath temperature lowers the overvoltage of the iron-group metal elements, which may shift the deposition potential to a noble potential direction. Therefore, reduced overvoltage can increase the current efficiency of binary Fe-W alloys and also can increase the W content of the plating [49]. Thus, it is supposed that Zn can be incorporated into the structure of binary Fe-W alloys at higher bath temperatures, while Zn-based deposits will be dominant at lower bath temperatures.

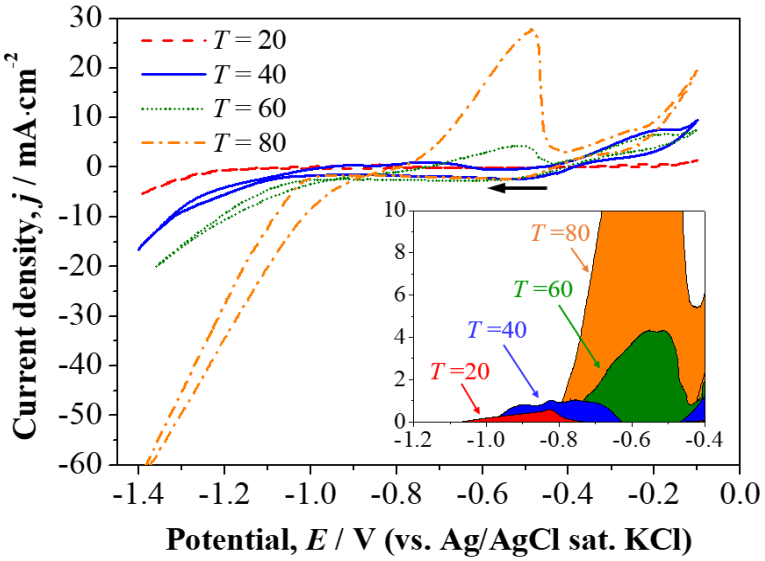

Figure 3.10 LSV curve (upper plot) and frequency variation measured by EQCM (lower plot) for Cit-Zn bath with and without addition of 0.8M of $(NH_4)_2SO_4$. The scan rate was 20 mV·s^{-1}.

3.5.4 Electrodeposition process

The bath compositions of the Fe-W-Zn plating bath are shown in Table 3.6. Binary Fe-W plating was also prepared for comparison of the microstructures and grain sizes with ternary Fe-W-Zn plating. Binary Fe-W alloy were deposited in the same bath as the ternary plating but without the addition of $ZnSO_4 \cdot 7H_2O$. The prepared plating baths were degassed with high purity Ar gas for 30 min before the electrodeposition to eliminate dissolved oxygen in the baths. Commercial steel plate with an area of 2×2 cm^2 was used as cathode for electrodeposition. A Pt coil placed in the anode chamber filled with diluted H_2SO_4 solution was used as anode. The steel plates were cleaned by ethanol and chemically dipped in 10 wt.% H_2SO_4 solution before use. Chronoamperometry was conducted for electrodeposition of ternary alloy with a potential of -1.1, -1.2, -1.3 and -1.4 V (vs. Ag/AgCl). A 50 $C \cdot cm^{-2}$ of fixed amount of electric charge was applied for electrodeposition. Continuous magnetic stirring at 500 rpm was conducted during plating process.

Table 3.6 Bath compositions for ternary Fe-W-Zn plating.

Composition	Concentration ($mol \cdot dm^{-3}$)
$Na_3C_6H_5O_7$	0.26
$ZnSO_4 \cdot 7H_2O$	0.01
$FeSO_4 \cdot 7H_2O$	0.2
$Na_2WO_4 \cdot 2H_2O$	0.05
$(NH_4)_2SO_4$	0.8

The current efficiency (C_{eff}) was measured by calculating the gained mass of the cathode after plating and the elemental compositions of the ternary alloys analyzed by EDS using following Faraday's Law:

$$C_{\text{eff}} = \frac{\text{mass of the deposits}}{\text{theoretical mass gain}} \times 100$$

$$= \frac{w \cdot F}{Q} \sum \frac{C_x \cdot N_x}{M_x} \times 100 \quad (3.9)$$

where w is the weight of deposited alloys (g), F is Faraday's constant (normally 96,485 C·mol^{-1}), Q is the applied electric charge (C), C_x (x = Fe, W and Zn) is the weight fraction of each metals in the deposited alloys, N_x is the ionic valence of each metals, and M_x is the atomic weight of each metal element (g·mol^{-3}) [50].

The current efficiencies and applied current densities at various electrodeposition potential range of -1.1 to -1.4 V (vs. Ag/AgCl) are presented in Figure 3.11. The elemental compositions of the ternary Fe-W-Zn alloy plating are given in Table 3.7.

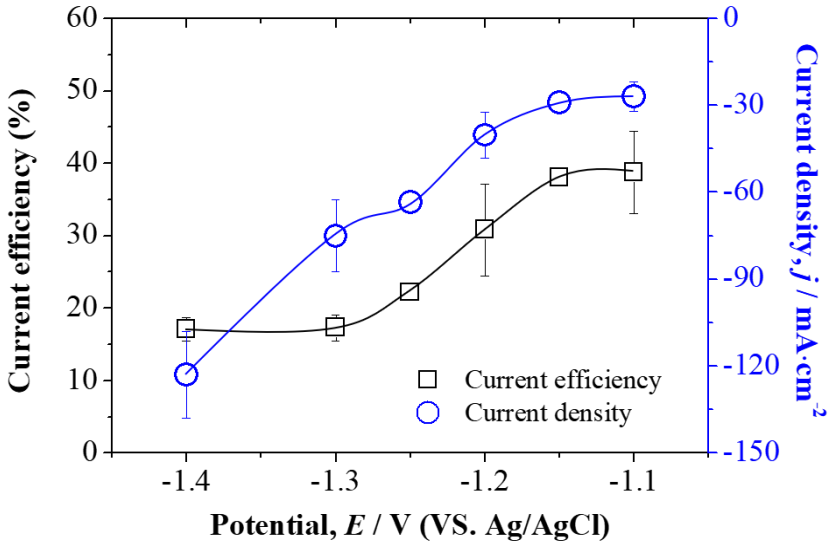

Figure 3.11 Current efficiencies and applied current densities of the electrodeposition of ternary Fe-W-Zn alloy plating. (Bath temperature, T = 80 °C)

Table 3.7 Elemental compositions of ternary Fe-W-Zn alloy plating obtained at various electrodeposition potentials.

Deposition Potential	Composition (at.%)		
	Fe	W	Zn
−1.10 V	69.19	29.08	1.73
−1.20 V	66.17	31.17	2.12
−1.30 V	61.76	34.22	4.03
−1.40 V	55.88	35.96	8.16

Decrease in the current efficiency was accompanied by an increasing the Zn content in the ternary alloy plating. The current efficiency gradually decreased and current density increased as the electrodeposition potential become negative direction. The maximum cathodic current efficiency was 43% at -1.10 V and minimum of 15% at -1.40 V. A drastic decrease in cathodic current efficiency at potential below -1.15 V was confirmed. At the same time, the Zn content of the alloys increase as the electrodeposition potential became lower. The content of Zn in alloys was closely related to the deposition amount of Zn from Fe- and W-free Cit-Zn bath observed in EQCM measurement shown in Figure 3.9, implying the deposition of Zn is apart from the other two elements. Meanwhile, it was found that the W content of ternary alloys was increased as electrodeposition potential became lower. This is similar to the tendency of increased W content in electrodeposited iron group-W alloy plating deposited at higher current densities [11,23]. Various researchers have revealed that a lower overpotential in induced codeposition process promotes the electrodeposition of metallic Mo and W [51,52]. The increased Zn content of the ternary alloys at lower electrodeposition potentials indicates that anomalous codeposition is happening, which is normally observed in electrodeposition of iron group metal-Zn alloy platings [53]. At the low electrodeposition potential, the pH near the cathode surface during electrodeposition process shall increase and may promote the anomalous codeposition of metal Zn from $[Zn(NH_3)_4]^{2+}$ complex. This can suppress the induced codeposition of binary Fe-W alloy from mixed-metal complex, thereby affecting the total elemental composition of the ternary alloy plating [54]. Therefore, it was anticipated that both induced codeposition of Fe-W alloy from Cit-Fe-W complex ions and anomalous codeposition of Zn from Zn-NH_3 complex ion; $[Zn(NH_3)_4]^{2+}$ took place in this ternary alloy plating system.

3.6 Characterization of alloy plating

3.6.1 Morphology observation

The surface morphologies of deposited alloys were observed using SEM. The elemental composition of alloy plating was characterized by EDS. Considering the thickness of the electrodeposited alloy plating specimens, EDS measurement was conducted on alloy plating specimens deposited on commercial Ni plates instead of steel plates.

SEM micrographs and optical photographs of ternary Fe-W-Zn alloy plating electrodeposited at various potential are shown in Figure 3.12. All of electrodeposited ternary alloys were well adhered to the steel substrates and showed uniform, semi-glossy appearances. However, cracks were presented at the ternary alloy plating electrodeposited at -1.4 V, possibly originated by high internal stress.

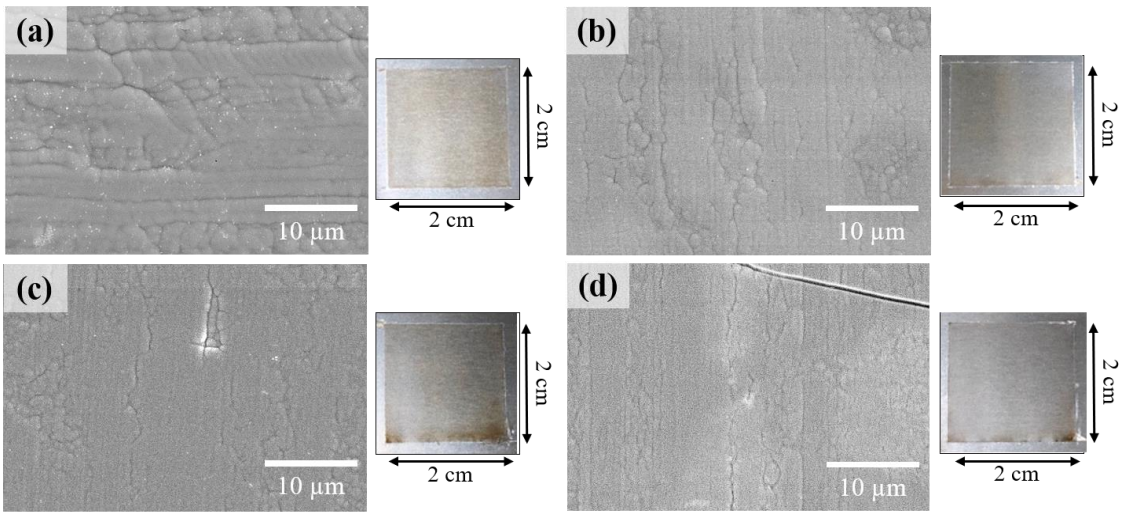

Figure 3.12 SEM micrographs and optical photographs of ternary Fe-W-Zn alloy plating: alloys electrodeposited at (a) -1.1 V, (b) -1.2 V, (c) -1.3 V, and (d) -1.4 V. Equivalent amount of charge Q= 50 C·cm^{-2} was applied.

Figure 3.13 shows the cross sectional SEM micrographs for binary Fe-W alloy plating and ternary Fe-W-Zn alloy plating prepared at -1.10 and -1.20 V. At the same electrodeposition potential, the W content of the alloy plating was similar, but higher for binary Fe-W alloy.

However, a significant difference in cross- sectional microstructure of alloy platings was confirmed. The grain size was found to be drastically decreased by the incorporation of Zn into binary Fe-W alloy structure.

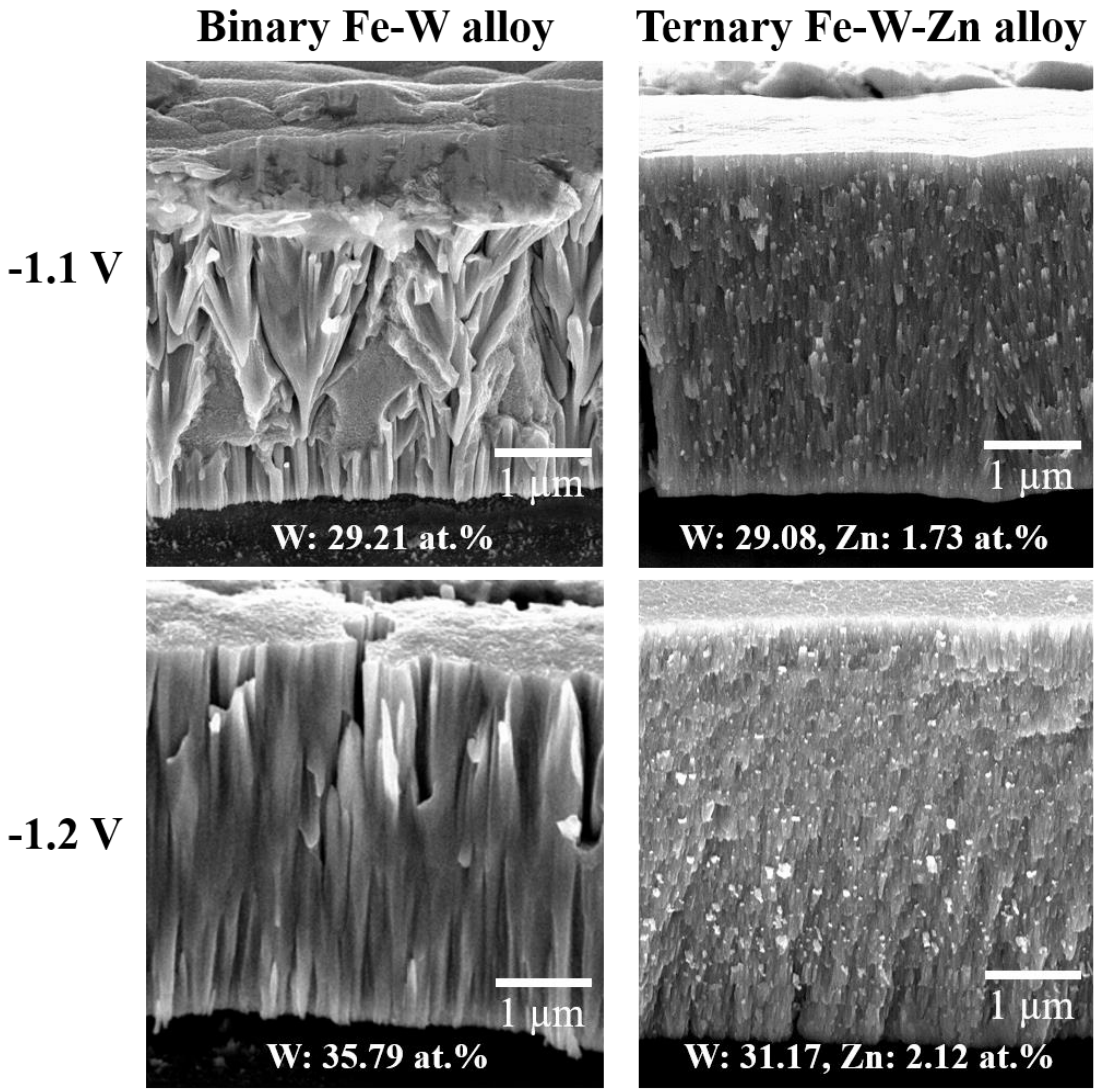

Figure 3.13 Cross sectional SEM micrographs for binary Fe-W alloy plating and ternary Fe-W-Zn alloy plating prepared at potential of -1.1 and -1.2 V. Equivalent amount of charge Q= 50 C·cm^{-2} was applied.

3.6.2 Crystalline structures analysis

Crystalline structures of alloy plating were characterized by XRD equipped with Cu-Kα source (λ: 0.154056 nm). The measurement range, scanning speed, accelerating voltage and accelerating current were $30° \leq 2\theta \leq 90°$, 2.0°/min, 40 kV and 30 mA, respectively. The grain sizes of ternary Fe-W-Zn alloy were obtained by calculating the derived parameters from the XRD patterns into Scherrer's equation:

$$D = \frac{k \cdot \lambda}{\beta \cdot \cos\theta} \qquad (3.10)$$

where, D (nm) is the calculated average grain size of the alloy plating, k is Scheer's constant (taken as 0.94 in this study), λ is wavelength of X-ray sources, β is the determined full width at half maximum (FWHM), and θ is the position of the peak. The calculated grain sizes of ternary Fe-W-Zn alloy platings were compared to those of binary Fe-W platings for investigating the effect of grain refinement by Zn addition.

X-ray diffraction patterns for ternary Fe-W-Zn alloy platings, binary Fe-W plating electrodeposited at -1.2V and steel plate used as substrate are shown in Figure 3.14. The ternary Fe-W-Zn alloy plating showed similar diffraction patterns to the binary Fe-W alloy plating. A single broad diffraction peak near the Fe (110) plane (2θ= 44.74°) appeared near 43.4° in all ternary alloy plating, indicating the ternary alloy was lowly crystalline amorphous-like nanocrystal structure similar to the results of other research on Fe-W plating [6,14]. The broadening of diffraction peak of ternary alloy plating indicates the Zn and W atoms are incorporated into the BCC structure of the Fe lattice [55]. The peaks of the steel plate were detected in the ternary alloys prepared by electrodeposition at -1.3 and -1.4 V due to thin plating thickness as a result of the low cathodic current efficiency.

Calculated grain size of the ternary Fe-W-Zn and binary Fe-W alloy platings are presented in Figure 3.15. Result shows the grain size of the ternary Fe-W-Zn and binary Fe-W alloy plating gradually decreased as the deposition potential become lower. It is considered that the grain size of both alloys decreases as the incorporated amount of W and Zn atoms into Fe lattice increases.

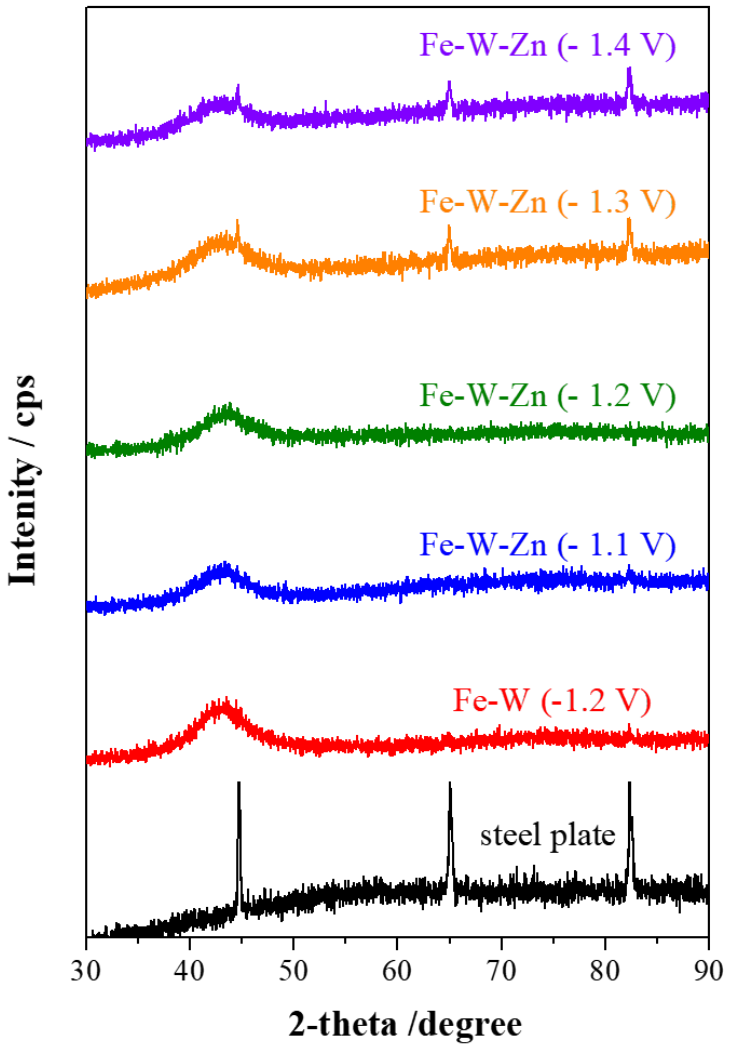

Figure 3.14 Current efficiencies and applied current densities of the electrodeposition of ternary Fe-W-Zn alloy plating. (Bath temperature, T = 80 °C)

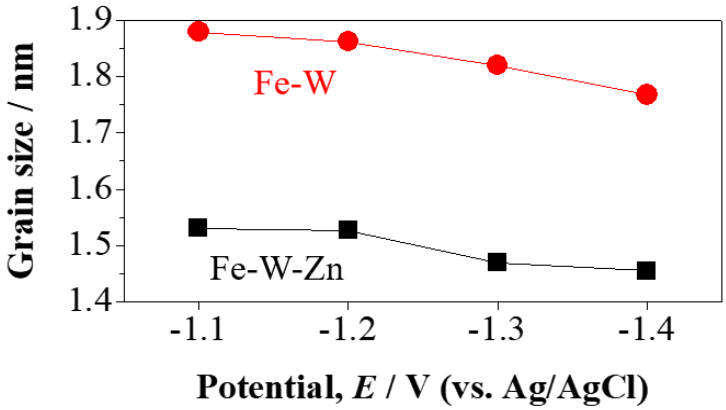

Figure 3.15 Current efficiencies and applied current densities of the electrodeposition of ternary Fe-W-Zn alloy plating. (Bath temperature, T = 80 °C)

Figure 3.16 exhibits the relation between the content of W and Zn of alloy plating and the grain size. Increase in Zn content in alloy plating obviously induced grain refinement while increase in W content in binary Fe-W alloy plating showed only slight grain refinement effect, even at high W content of approximately 35%. This indicates the Zn content has a distinctive influence on the crystal refinement of Fe-W alloy plating.

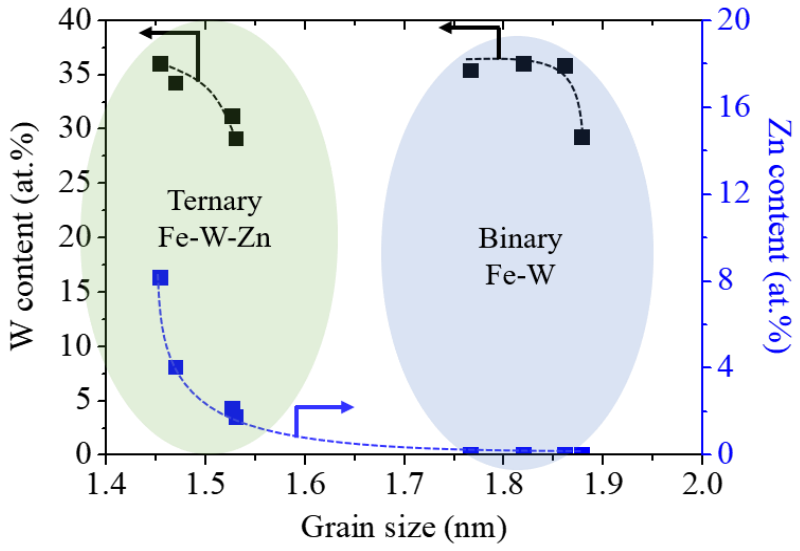

Figure 3.16 Current efficiencies and applied current densities of the electrodeposition of ternary Fe-W-Zn alloy plating. (Bath temperature, T = 80 °C)

3.6.3 Chemical states analysis

The chemical states of metal components of ternary alloy plating were analyzed using XPS equipped with Al-kα source (1486 eV). High-resolution scans for Fe 2p, W 4f and Zn LMM were measured at pass energy of 20 eV, in step of 0.05 eV with dwell time of 50 msec. Ar etching was conducted for 5 min with 1000 eV Ar ion beam to compare chemical states of the surface and inside of the plating layer.

XPS measurement results are shown in Figure 3.17. Figure 3.17(a) reveals XPS W4f core level spectra of before Ar etching (as-deposited state) and after Ar etching for 5 min. Result shows that W exist mainly as W^{6+} (WO_3, binding energy of 35.7 eV) at top surface of ternary alloy plating, while mostly as W_0 (metallic W, binding energy of 31.06 eV) at the inside. Fe 2p core level spectra shown in Figure 3.17(b) indicates Fe slightly exists, as oxidized state (Fe_2O_3, binding energy of 711.3 eV) at top surface and mainly as metallic Fe (707.1 eV) inside the plating [56]. Because of only slight energy shift at Zn 2p core level region, Zn LMM Auger peaks were investigated to verify the chemical state of Zn [57]. As can see in Figure 3.17(c), Zn is expected to exist in metallic state at inside of the alloy plating, which the peaks corresponding to metal Zn (distinguishing peaks originated from 992.0 and 995.6 eV) is coincident with that of Zn LMM spectra obtained from bulk Zn plate after Ar etching for 5 min, while peaks correspond to Zn^{2+} appeared at lower binding energy (near 989.3 eV) region. This means that the outer surface of the ternary alloy plating is mainly exist as a thick WO_3, not as an oxide of Fe or Zn, while the inside of the plating layer consisted of highly metallic alloys.

In conclusion, XPS result shows that the Zn was successfully electrodeposited from Zn-NH_3 complex ion; $[Zn(NH_3)_4]^{2+}$ in the metallic state, and this process did not affect the induced codeposition of Fe-W alloy, especially the reduction reaction of tungstate ion (WO_4^{2-}).

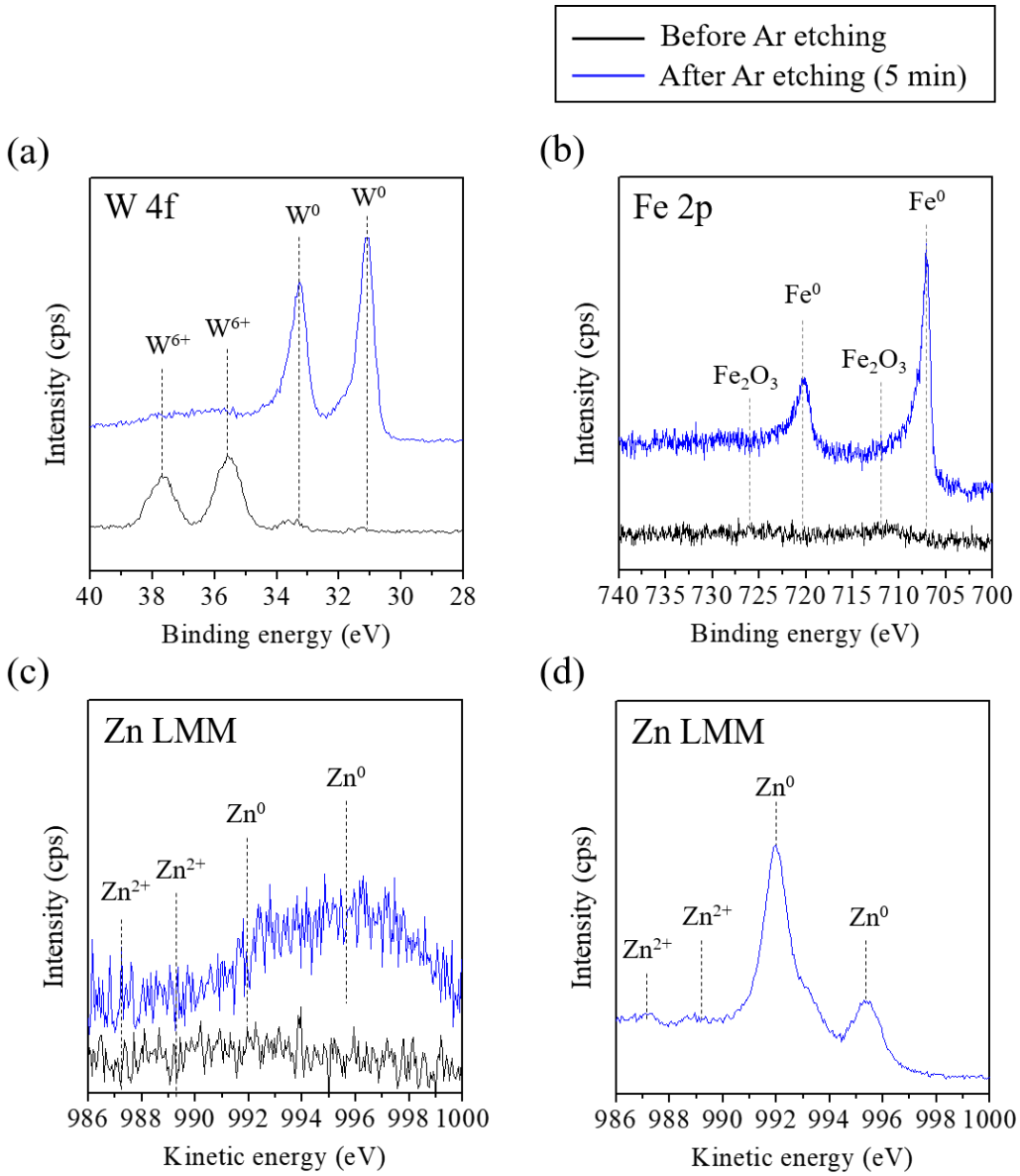

Figure 3.17 High-resolution XPS spectra: (a, b, c) W 4f, Fe 2p, Zn LMM spectra of ternary Fe-W-Zn alloy plating, respectively and (d) Zn LMM spectra of bulk Zn obtained after Ar etching for 5 min. (Electrodeposited conditions of ternary alloy: -1.2 V with electric charge, Q= 50 C·cm^{-2})

3.7 Corrosion properties

3.7.1 Potentiodynamic polarization test

Corrosion properties of electrodeposited ternary alloy plating were evaluated by potentiodynamic polarization test. Measurements were conducted in both 1M H_2SO_4 solution and 3 mass.% NaCl solution at room temperature. The test solution was degassed with high purity Ar gas before use for 30 min to eliminate dissolved oxygen in solution. The exposed area of plating specimens was fixed to 1×1 cm^2. The corrosion potential (E_{corr}) and corrosion current density (I_{corr}) of the alloy plating were calculated using the Tafel's equation. The passivation properties of the alloy plating were discussed by comparing with electrodeposited Ni-W alloy (19.68 at.% W), Fe-W alloy (33.10 at.% W), and bare steel plate. The bath composition and electrodeposition conditions for the Ni-W and Fe-W alloy plating used for the corrosion test are shown in Table 3.8. The polarization measurement was conducted as a scan range from -0.4 (vs. OCP) to +2.5 V (vs. Ag/AgCl) with 1 $mV \cdot s^{-1}$ after stabilizing the OCP thoroughly.

Table 3.8 Bath composition and electrodeposition conditions of Fe-W and Ni-W alloy plating for corrosion test.

Reagent and conditions	Bath composition [$mol \cdot dm^{-3}$]	
	Fe-W	Ni-W
$(NH_4)_3C_6H_5O_7$	0.3	0.3
$FeSO_4$	0.1	-
$NiSO_4$	-	0.1
Na_2WO_4	0.2	0.2
Bath temperature [°C]	60	40
pH	7.0	7.0
Current density [$mA \cdot cm^2$]	-30	-50

3.7.1.1 Corrosion resistance in acidic H_2SO_4 solution

Anodic polarization measurements were performed for the ternary Fe-W-Zn alloy plating and comparative materials in deaerated 1M H_2SO_4 solution for evaluating the corrosion resistance in an acidic environment. Results are shown in Figure 3.18. Figure 3.18(a) shows the measurement results obtained at various electrodeposition potentials.

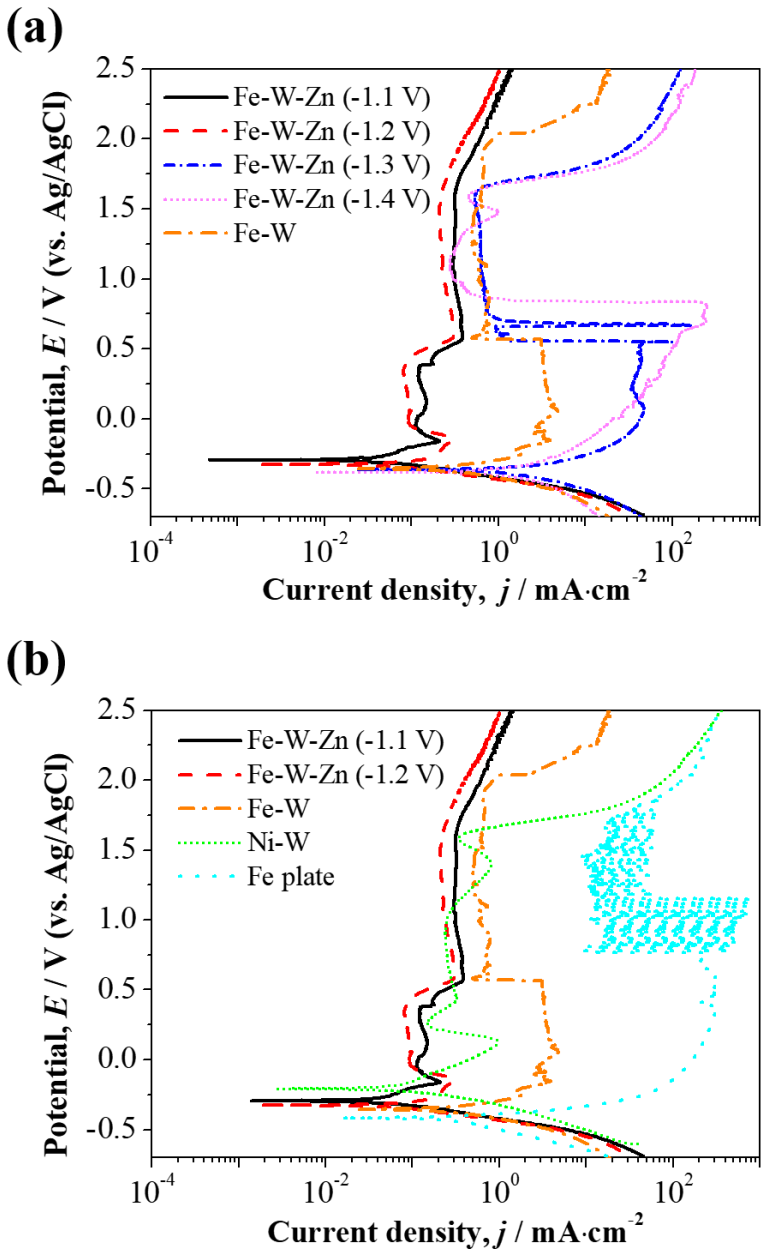

Figure 3.18 Polarization curves measured in deaerated 1M H_2SO_4 solution: (a) ternary Fe-W-Zn alloy plating and (b) with comparative materials.

The corrosion potential (E_{corr}) of the ternary Fe-W-Zn alloy plating gradually shifted to the base potential direction and the corrosion current density (I_{corr}) gradually increased as the electrodeposition potential became lower. This means the Zn and W contents of the ternary alloy shifted E_{corr} toward lower potential direction. Since the redox potential of Zn is the lowest (E^0= -0.76 V vs SHE) among the alloying elements, it is considered E_{corr} become lower as the Zn content of ternary alloy increases. However, although the redox potential of W is higher than that of Fe, it has been informed by other researchers that high W content in Fe-W and Ni-W alloy platings can lower the E_{corr} [58,59]. This is considered to be because n type semiconductor of WO_3 is formed by the oxidation of W on the surface of alloys [60]. The accumulation of negative charge at WO_3 surface shift E_{corr} to more negative potential values [61]. Polarization curves of the ternary alloy plating and various comparative materials are shown in Figure 3.18(b). The E_{corr} of binary Fe-W alloy plating was -355.46 mV, which was slightly higher than that of steel plate (-419.81 mV). The E_{corr} of ternary alloy platings gradually decreased as the electrodeposition potential become lower, which is considered to be related to the W content of the ternary alloys. The ternary alloy plating electrodeposited at -1.10 V exhibited I_{corr} of 21.60 $\mu A \cdot cm^{-2}$, which was the lowest value among the ternary Fe-W-Zn alloy plating and even lower than Ni-W alloy plating (28.46 $\mu A \cdot cm^{-2}$). The ternary Fe-W-Zn alloy plating obtained at -1.20 V also showed a low I_{corr} of 31.24 $\mu A \cdot cm^{-2}$. Meanwhile, when the electrodeposition potential is lower than -1.30 V, a significant increase in I_{corr} was confirmed, which was even higher than that of binary Fe-W alloy plating. Moreover, only the ternary alloys electrodeposited at -1.10 and -1.20 V showed two passivation areas with low passive current densities (I_p). The first passivation area appeared at -0.15 to +0.41 V, and the second area continued until the potential was higher than +2.5 V. The second passivation showed similar passive behavior to that of binary Fe-W alloy plating (33 at.% W). Meanwhile, the trans-passive potentials (E_t) of the ternary alloy plating were higher than those of Ni-W alloy plating (+1.6 V) and Fe-W alloy plating (+2.0 V), and continued until +2.5 V. This means the pitting corrosion in sulfuric acid solution was greatly suppressed in ternary Fe-W-Zn alloy plating. Moreover, the first passivation area is a unique property of this Fe-W-Zn alloy plating, which closely related to the Zn content in the

ternary alloy. I_p of ternary alloy plating decreased until the Zn content reached about 2 at.% and then increased thereafter.

3.7.1.2 Corrosion resistance in neutral NaCl solution

Polarization curves measured in deaerated neutral 3 mass.% NaCl solution are presented in Figure 3.19.

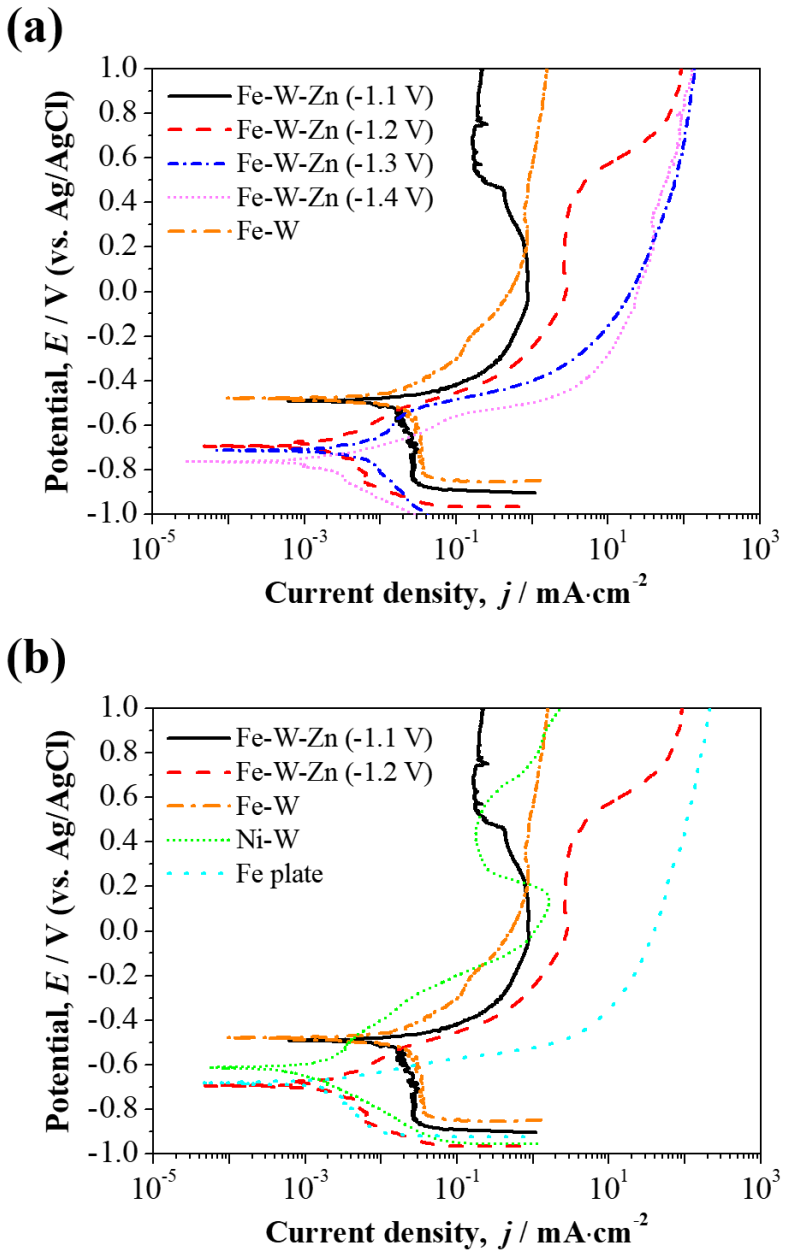

Figure 3.19 Polarization curves measured in deaerated 3 mass% NaCl solution: (a) ternary Fe-W-Zn alloy plating and (b) with comparative materials.

As seen in Figure 3.19(a), the E_{corr} of ternary alloy platings decreased as electrodeposition potential became lower. However, I_{corr} gradually decreased at lower potential, showing contrast results with measurement results in the 1M H_2SO_4 solution. The polarization curves of the ternary alloy plating prepared by electrodeposition at -1.1 V was similar to that of binary Fe-W alloy plating, but the passivation area gradually deceased as electrodeposition potential became lower.

3.7.1.3 Discussion in corrosion resistance

The polarization parameters and W contents of each alloy plating are presented in Table 3.9, and the correlation between Zn content of ternary alloy plating and polarization parameters are shown in Figure 3.20.

Table 3.9 Polarization parameters of ternary Fe-W-Zn alloy plating and comparative materials.

Specimen	W cont. [at.%]	At 1 M H_2SO_4		At 3 mass% NaCl	
		E_{corr} [mV]	I_{corr} [μA·cm^{-2}]	E_{corr} [mV]	I_{corr} [μA·cm^{-2}]
Fe–W–Zn (−1.1 V)	29.08	−288.44	21.60	−502.87	13.91
Fe–W–Zn (−1.2 V)	31.17	−325.19	31.24	−680.11	2.71
Fe–W–Zn (−1.3 V)	34.22	−366.22	726.32	−716.26	5.23
Fe–W–Zn (−1.4 V)	37.12	−377.63	1155.12	−785.87	1.45
Fe–W	33.10	−353.46	181.17	−491.34	11.27
Ni–W	19.68	−219.50	28.46	−636.05	1.01
Steel plate	–	−419.81	179.80	−673.33	1.83

Figure 3.20 shows that there is no distinctive relation between E_{corr} and Zn content of ternary alloy plating in 1M H_2SO_4 solution, while E_{corr} tend to decrease as W content of alloy plating increased as seen in Table 3.9. This indicates the W content of the binary Fe-W and ternary Fe-W-Zn alloy plating is considered as a primary factor for determining the E_{corr} in 1M H_2SO_4 solution. In contrast, the Zn content have a great influence on the E_{corr} of the ternary alloy plating in the

3 mass% NaCl solution. A distinct decrease in I_{corr} for ternary alloy platings in both 1M H_2SO_4 solution and 3 mass% NaCl solution was confirmed when the Zn content became around 2 at.%. It is anticipated that Zn has a critical role on the overall corrosion resistance of the ternary alloy plating only when the Zn content is in a particular range that can control the microstructure of the alloy platings.

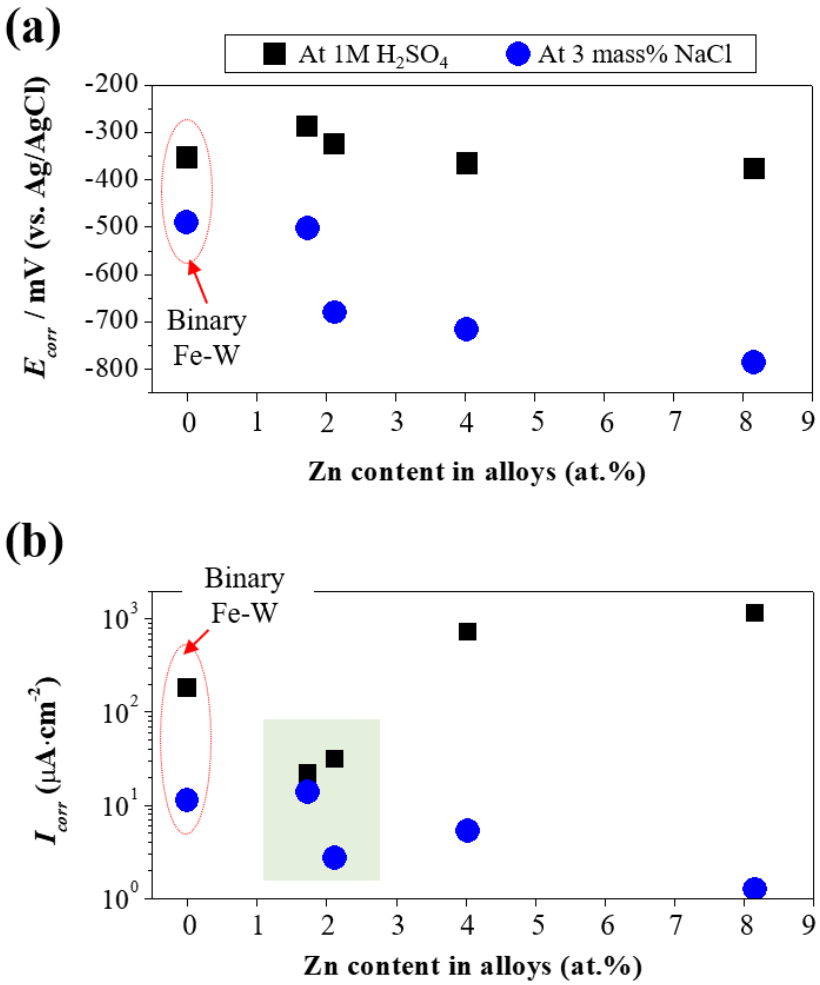

Figure 3.20 Polarization parameters of ternary Fe-W-Zn alloy platings: (a) corrosion potential (E_{corr}) and (b) corrosion current density (I_{corr}) as a function of Zn content of alloys.

Figure 3.21 shows the compared polarization curves of W-based alloy platings and hexavalent Cr plating (electrodeposited at Sargent bath) measured in 1M H_2SO_4

solution. Ternary Fe-W-Zn alloy plating prepared in this study showed lowest I_{corr} and superior passivation properties, which has better corrosion resistance than other W-based binary alloy plating and even Cr plating.

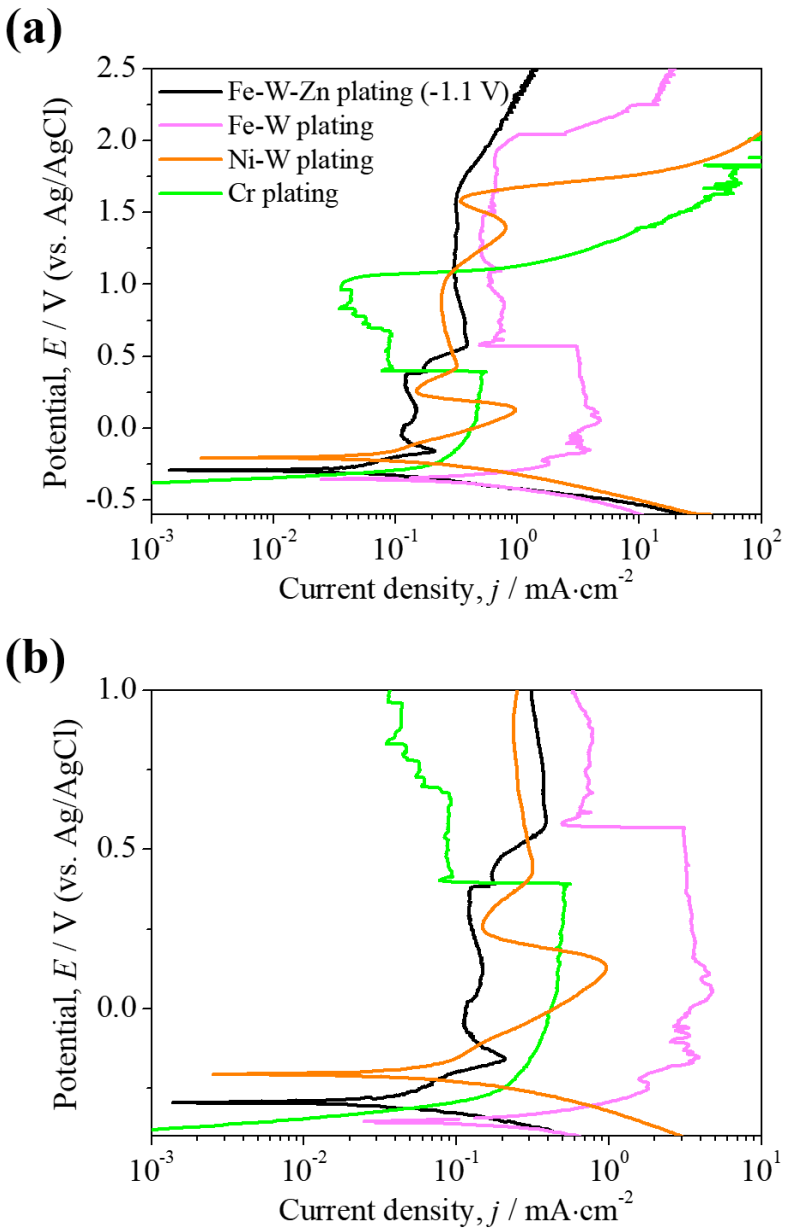

Figure 3.21 Polarization curves measured in 1M H_2SO_4 solution: (a) W-based alloy platings with Cr plating and (b) enlarged plots of (a).

3.8 Conclusion

In this work, a novel ternary Fe-W-Zn alloy plating was prepared by electrodeposition in citrate-ammonia bath and its corrosion properties were discussed. The formation of stable Zn-NH_3 complex ions, $[Zn(NH_3)_4]^{2+}$ by addition of $(NH_4)_2SO_4$ in plating bath, allowed Zn to be alloyed into the binary Fe-W alloy plating over a wide electrodeposition potential. The electrodeposition behaviors of the ternary Fe-W-Zn alloy plating was determined by the induced codeposition of the binary Fe-W alloy and the independent electrodeposition of Zn from Zn-NH_3 complex ions. The current efficiency decreased proportionally as the Zn content of the ternary alloy plating increased, while EQCM measurement results revealed that adsorption of Zn-NH_3 complex ions on the cathode slightly suppressed the electrodeposition of Fe-W alloy. The incorporation of Zn into the Fe-W alloy structure caused refinement of the grain size down to about 1.45 nm. The electrodeposited ternary alloy plating with a particular Zn content showed enhanced corrosion properties compared to binary Fe-W alloy plating. The corrosion properties of the ternary alloy platings were highly related to the elemental composition, especially, Zn. When the Zn content of ternary alloy plating was approximately 2 at.%, ternary alloy plating showed enhanced corrosion properties in 1M H_2SO_4 solution and in 3 mass% NaCl solution. The addition of Zn changed the plating structure while refining the crystalline size of the plating, and it is considered to be effective in improving corrosion resistance by changing the columnar structure of the Fe-W alloy into a nanocrystalline structure.

This novel ternary alloy plating is considered a possible candidate for plating with various industrial applications, which requires properties such as hardness, abrasion resistance and corrosion resistance.

Acknowledgement

References

[1] 若林信一, 次世代めっき技術 表面技術におけるプロセス・イノベーション, 日刊工業新聞社, 2005.

[2] L. Hua, Y.C. Chan, Y.P. Wu, B.Y. Wu, The determination of hexavalent chromium (Cr^{6+}) in electronic and electrical components and products to comply with RoHS regulations, J. Hazard. Mater. 163 (2009) 1360–1368.

[3] R. Rodríguez, J.J. Espada, M. Gallardo, R. Molina, M.J. López-Muñoz, Life cycle assessment and techno-economic evaluation of alternatives for the treatment of wastewater in a chrome-plating industry, J. Clean. Prod. 172 (2018) 2351–2362.

[4] H. Bhatt, Alternatives to Hexavalent Chromium to Comply with European Union's Directives (ELV, RoHS and WEEE), Plat. Surf. Finish. 93 (2006) 20–23.

[5] D.P. Weston, P.H. Shipway, S.J. Harris, M.K. Cheng, Friction and sliding wear behaviour of electrodeposited cobalt and cobalt–tungsten alloy coatings for replacement of electrodeposited chromium, Wear. 267 (2009) 934–943.

[6] N. Tsyntsaru, J. Bobanova, X. Ye, H. Cesiulis, A. Dikusar, I. Prosycevas, J.-P. Celis, Iron–tungsten alloys electrodeposited under direct current from citrate–ammonia plating baths, Surf. Coatings Technol. 203 (2009) 3136–3141.

[7] N.P. Wasekar, N. Hebalkar, A. Jyothirmayi, B. Lavakumar, M. Ramakrishna, G. Sundararajan, Influence of pulse parameters on the mechanical properties and electrochemical corrosion behavior of electrodeposited Ni-W alloy coatings with high tungsten content, Corros. Sci. 165 (2020) 108409.

[8] P. de Lima-Neto, A.N. Correia, R.A.C. Santana, R.P. Colares, E.B. Barros, P.N.S. Casciano, G.L. Vaz, Morphological, structural, microhardness and electrochemical characterisations of electrodeposited Cr and Ni–W coatings, Electrochim. Acta. 55 (2010) 2078–2086.

[9] L. Elias, A.C. Hegde, Electrodeposition of laminar coatings of Ni–W alloy and their corrosion behaviour, Surf. Coatings Technol. 283 (2015) 61–69.

[10] M.P.Q. Arganaraz, S.B. Ribotta, M.E. Folquer, L.M. Gassa, G. Benitez, M.E. Vela, R.C. Salvarezza, Ni–W coatings electrodeposited on carbon steel: Chemical composition, mechanical properties and corrosion resistance, Electrochim. Acta. 56 (2011) 5898–5903.

[11] K.A. Kumar, G.P. Kalaignan, V.S. Muralidharan, Pulse electrodeposition and characterization of nano Ni–W alloy deposits, Appl. Surf. Sci. 259 (2012) 231–237.

[12] X. Liu, Z. Xiang, J.C. Niu, K.D. Xia, Y. Yang, B. Yan, W. Lu, The corrosion behaviors of amorphous, nanocrystalline and crystalline Ni-W alloys coating, Int. J. Electrochem. Sci. 10 (2015) 9042–9048.

[13] A. Mulone, A. Nicolenco, V. Hoffmann, U. Klement, N. Tsyntsaru, H. Cesiulis, In-depth characterization of as-deposited and annealed Fe-W coatings electrodeposited from glycolate-citrate plating bath, Electrochim. Acta. 261 (2018) 167–177.

[14] S. Wang, C. Zeng, Y. Ling, J. Wang, G. Xu, Phase transformations and electrochemical characterizations of electrodeposited amorphous Fe–W coatings, Surf. Coatings Technol. 286 (2016) 36–41.

[15] V. Vasauskas, J. Padgurskas, R. Rukuiža, H. Cesiulis, J.-P. Celis, D. Milčius, I. Prosyčevas, Cracking behavior of electrodeposited nanocrystalline tungsten-cobalt and tungsten-iron coatings, Mechanics. 72 (2008) 21–27.

[16] H. Capel, P.H. Shipway, S.J. Harris, Sliding wear behaviour of electrodeposited cobalt–tungsten and cobalt–tungsten–iron alloys, Wear. 255 (2003) 917–923.

[17] M. Donten, H. Cesiulis, Z. Stojek, Electrodeposition and properties of Ni-W, Fe-W and Fe-Ni-W amorphous alloys. A comparative study, Electrochim. Acta. 45 (2000) 3389–3396.

[18] J. Ahmad, K. Asami, A. Takeuchi, D. V Louzguine, A. Inoue, High strength Ni-Fe-W and Ni-Fe-WP alloys produced by electrodeposition, Mater. Trans. 44 (2003) 1942–1947.

[19] S.-J. Mun, M. Kim, T.-H. Yim, J.-H. Lee, T. Kang, Mechanical and structural characteristics of electrodeposited Ni–Fe–W alloy after heat-treatment, J. Electrochem. Soc. 157 (2010) 177–180.

[20] F. He, J. Yang, T. Lei, C. Gu, Structure and properties of electrodeposited Fe–Ni–W alloys with different levels of tungsten content: A comparative study, Appl. Surf. Sci. 253 (2007) 7591–7598.

[21] A.L.M. Oliveira, J.D. Costa, M.B. de Sousa, J.J.N. Alves, A.R.N. Campos, R.A.C. Santana, S. Prasad, Studies on electrodeposition and characterization of the Ni–W–Fe alloys coatings, J. Alloys Compd. 619 (2015) 697–703.

[22] K.R. Sriraman, S.G. Sundara Raman, S.K. Seshadri, Synthesis and evaluation of hardness and sliding wear resistance of electrodeposited nanocrystalline Ni–Fe–W alloys, Mater. Sci. Technol. 22 (2006) 14–20.

[23] K.R. Sriraman, S.G.S. Raman, S.K. Seshadri, Corrosion behaviour of electrodeposited nanocrystalline Ni–W and Ni–Fe–W alloys, Mater. Sci. Eng. A. 460 (2007) 39–45.

[24] N.P. Raval, P.U. Shah, N.K. Shah, Adsorptive removal of nickel (II) ions from aqueous environment: a review, J. Environ. Manage. 179 (2016) 1–20.

[25] A. Goldenberg, S. Admani, J.L. Pelletier, S.E. Jacob, Belt buckles—Increasing awareness of nickel exposure in children: A case report, Pediatrics. 136 (2015) 691–693.

[26] M. Saito, R. Arakaki, A. Yamada, T. Tsunematsu, Y. Kudo, N. Ishimaru, Molecular mechanisms of nickel allergy, Int. J. Mol. Sci. 17 (2016) 202.

[27] A. Mulone, A. Nicolenco, J. Fornell, E. Pellicer, N. Tsyntsaru, H. Cesiulis, J. Sort, U. Klement, Enhanced mechanical properties and microstructural modifications in electrodeposited Fe-W alloys through controlled heat treatments, Surf. Coatings Technol. 350 (2018) 20–30.

[28] Y. Ruan, S. Yao, M. Kowaka, Amorphization of electrodeposited Fe-W alloy films and electrochemical behavior, J. Non. Cryst. Solids. 117 (1990) 752–755.

[29] L.G. Sillén, A.E. Martell, Stability Constants of Metal-Ion Complexes, Supplement No. 1, The Chemical Society, 1971.

[30] G.R. Hedwig, J.R. Liddle, R.D. Reeves, Complex formation of nickel (II) ions with citric acid in aqueous solution: a potentiometric and spectroscopic study, Aust. J. Chem. 33 (1980) 1685–1693.

[31] L.G. Sillen, A.E. Martell, J. Bjerrum, Stability constants of metal-ion complexes., Chemical Society, 1964.

[32] J.J. Cruywagen, L. Krüger, E.A. Rohwer, Complexation of tungsten (VI) with citrate, J. Chem. Soc. Dalt. Trans. (1991) 1727–1731.

[33] E. Gileadi, N. Eliaz, The mechanism of induced codeposition of Ni-W alloys, ECS Trans. 2 (2007) 337–349.

[34] O. Younes, E. Gileadi, Electroplating of Ni/W alloys I. Ammoniacal citrate baths, J. Electrochem. Soc. 149 (2002) 100–111.

[35] 石田幸平, 中出卓男, 森河務, 三宅正男, 平藤哲司, イオン交換膜– 複数陽極システムを用いた Fe-W 合金めっきの耐熱特性および耐溶融亜鉛侵食性, 鉄と鋼. 103 (2017) 209–214.

[36] 石田幸平, 森河務, 三宅正男, 平藤哲司, Fe-W 合金めっきにおける Fe (III) の影響とイオン交換膜-複数陽極システムを用いた連続めっき, 表面技術. 67 (2016) 489–493.

[37] M. Izaki, Electrodeposition of iron and iron alloys, Mod. Electroplat. 4 (2010) 461–481.

[38] A. Nicolenco, N. Tsyntsaru, H. Cesiulis, Fe (III)-based ammonia-free bath for electrodeposition of Fe-W alloys, J. Electrochem. Soc. 164 (2017) 590–596.

[39] A. Nicolenco, A. Mulone, N. Imaz, N. Tsyntsaru, J. Sort, E. Pellicer, U. Klement, H. Cesiulis, E. García-Lecina, Nanocrystalline Electrodeposited Fe-W/Al2O3 Composites: Effect of Alumina Sub-microparticles on the Mechanical, Tribological, and Corrosion Properties, Front. Chem. 7 (2019) 241.

[40] A. Mulone, A. Nicolenco, N. Imaz, J. Fornell, J. Sort, U. Klement, Effect of heat treatments on the mechanical and tribological properties of electrodeposited Fe–W/Al2O3 composites, Wear. 448 (2020) 203232.

[41] A. Mulone, A. Nicolenco, N. Imaz, V. Martinez-Nogues, N. Tsyntsaru, H. Cesiulis, U. Klement, Improvement in the wear resistance under dry friction of electrodeposited Fe-W coatings through heat treatments, Coatings. 9 (2019) 66.

[42] D.-Y. Park, B.Y. Yoo, S. Kelcher, N. V Myung, Electrodeposition of low-stress high magnetic moment Fe-rich FeCoNi thin films, Electrochim. Acta. 51 (2006) 2523–2530.

[43] I. Rodriguez-Torres, G. Valentin, F. Lapicque, Electrodeposition of zinc–nickel alloys from ammonia-containing baths, J. Appl. Electrochem. 29 (1999) 1035–1044.

[44] L. Patrick, A. William, Water Chemistry: an Introduction to the Chemistry of natural and Engineered Aquatic Sytems, 2011.

[45] S. Capone, A. De Robertis, C. De Stefano, S. Sammartano, Formation and stability of zinc (II) and cadmium (II) citrate complexes in aqueous solution at various temperatures, Talanta. 33 (1986) 763–767.

[46] 邑瀬邦明, 錯体や化合物を含む Pourbaix 図: その作図と応用, Rev. Polarogr. 60 (2014) 35–47.

[47] O. Younes-Metzler, L. Zhu, E. Gileadi, The anomalous codeposition of tungsten in the presence of nickel, Electrochim. Acta. 48 (2003) 2551–2562.

[48] N. Eliaz, E. Gileadi, Induced codeposition of alloys of tungsten, molybdenum and rhenium with transition metals, in: Mod. Asp. Electrochem., Springer, 2008.

[49] M. Zemanová, M. Krivosudská, M. Chovancová, V. Jorík, Pulse current electrodeposition and corrosion properties of Ni–W alloy coatings, J. Appl. Electrochem. 41 (2011) 1077.

[50] X. Qiao, H. Li, W. Zhao, D. Li, Effects of deposition temperature on electrodeposition of zinc–nickel alloy coatings, Electrochim. Acta. 89 (2013) 771–777.

[51] E.J. Podlaha, D. Landolt, Induced Codeposition II. A Mathematical Model Describing the Electrodeposition of Ni-Mo Alloys, J. Electrochem. Soc. 143 (1996) 893–899.

[52] M. Ahmadi, M.J.F. Guinel, Synthesis, characterization and understanding of the mechanisms of electroplating of nanocrystalline–amorphous nickel–tungsten alloys using in situ electrochemical impedance spectroscopy, J. Alloys Compd. 574 (2013) 196–205.

[53] G. Roventi, R. Fratesi, R.A. Della Guardia, G. Barucca, Normal and anomalous codeposition of Zn–Ni alloys from chloride bath, J. Appl. Electrochem. 30 (2000) 173–179.

[54] C. Srivastava, S.K. Ghosh, S. Rajak, A.K. Sahu, R. Tewari, V. Kain, G.K. Dey, Effect of pH on anomalous co-deposition and current efficiency during electrodeposition of Ni-Zn-P alloys, Surf. Coatings Technol. 313 (2017) 8–16.

[55] C. Su, M. Ye, L. Zhon, J. Hou, J. Li, J. Guo, Oxidation of Fe–W alloy electrodeposits for application to anodes as lithium ion batteries, Surf. Rev. Lett. 23 (2016) 1550100.

[56] J. Winiarski, W. Tylus, M.S. Krawczyk, B. Szczygieł, The influence of molybdenum on the electrodeposition and properties of ternary Zn–Fe–Mo alloy coatings, Electrochim. Acta. 196 (2016) 708–726.

[57] J. Winiarski, W. Tylus, B. Szczygieł, EIS and XPS investigations on the corrosion mechanism of ternary Zn–Co–Mo alloy coatings in NaCl solution, Appl. Surf. Sci. 364 (2016) 455–466.

[58] A. Chianpairot, G. Lothongkum, C.A. Schuh, Y. Boonyongmaneerat, Corrosion of nanocrystalline Ni–W alloys in alkaline and acidic 3.5 wt.% NaCl solutions, Corros. Sci. 53 (2011) 1066–1071.

[59] H. Alimadadi, M. Ahmadi, M. Aliofkhazraei, S.R. Younesi, Corrosion properties of electrodeposited nanocrystalline and amorphous patterned Ni–W alloy, Mater. Des. 30 (2009) 1356–1361.

[60] M. Anik, Effect of concentration gradient on the anodic behavior of tungsten, Corros. Sci. 48 (2006) 4158–4173.

[61] T.A. Aljohani, B.E. Hayden, A simultaneous screening of the corrosion resistance of Ni–W thin film alloys, Electrochim. Acta. 111 (2013) 930–936.

CHAPTER 4

Electrodeposition of ternary Zn-Fe-Mo plating and improvement in corrosion resistance by additional Mo-oxide coating

4.1 Background of this research

4.1.1 Zn and Zn alloy plating

4.1.1.1 Zn plating

Unlike Cu, Ni and Cr, Zn has low hardness and easily rusts even in air. However, although Zn is highly corrosive under acidic and alkaline environment, Zn plating is widely used as an anti-corrosion plating for steel products because it shows excellent corrosion resistance when paired with Fe and also affordable. The standard electrode potential of zinc (-0.76 V (vs. NHE)) is lower than that of Fe, (-0.44 V), so Zn can act as a sacrificial anode for Fe [1].

The manufacturing method of Zn coating generally includes hot-dip coating, sheradizing, electroplating, and physical vapor deposition (PVD) method. Normally, hot-dip galvanizing is applied to large steel materials such as building materials, and electroplating is applied to small steel products such as mechanical parts and home applications [2]. However, in order to maintain the corrosion resistance of Zn plating in severe corrosive environments, various post-treatments and chemical conversion treatments need to be applied. Chromate conversion coating, which is a kind of chemical conversion treatment is applied to prevent the formation of white rust and improving the corrosion resistance of Zn plating. It is formed by immersion in an aqueous solution containing hexavalent or trivalent chromic acid as the main component for forming a chromate film on the Zn plating surface. However, currently Cr^{6+} used for chromate conversion coating is designated as a hazardous substance according to the RoHS directive, so Cr^{3+} conversion coating is used, but it suffers a problems of insufficient corrosion resistance [3-5]. Therefore, the needs for developing a Cr-free but high corrosion resistance plating are increasing.

4.1.1.2 Zn-iron group element alloy plating

In recent years, it is required to increase the lifespan of materials due to the harshness of the corrosive environment and sustainable development in the automobile and aircraft industries, and the number of products that cannot guarantee sufficient corrosion resistance in Zn plating is increasing. For the purpose of improving the corrosion resistance of Zn plating, alloying with iron-group metals (Ni, Co, Fe) by electroplating have been widely studied [6-8]. By alloying with iron-group metals, the corrosion potential of plating shift to noble potential direction closing to that of steel substrate, so that high corrosion resistance can be obtained. Among them, Zn-Ni plating is widely applied in various industrial fields such as automobile and aircraft components because of its superior anti-corrosion properties than conventional Zn plating [9-11]. The corrosion resistance of Zn-Ni plating is approximately 5 to 7 times higher than that of conventional Zn plating at salt spray test (SST) [12]. Owing to its superior corrosion resistance of Zn-Ni plating, Zn-Ni platings are finding its way into new industrial areas, getting closer to human's life, such as fasteners in agriculture, lawn, gardening and buildings. However, in recent years, Ni has been reported as major factor in triggering skin allergies for human. Eluted Ni ions from Ni and Ni-based alloy components can trigger skin inflammation [13,14]. Since Ni metals are considered to be harmful to humans due to their low biocompatibility, the use of Ni is already regulated in some products in Europe, and the regulation is expected to become more stringent in the future. Therefore, there is a need to invent an alternative plating with high corrosion properties without using Ni. Therefore, development of an alternative material for Zn-Ni plating is required when forecasting the future. In addition to Zn-Ni plating, Zn-Co plating and Zn-Fe plating exist, but both corrosion resistance is lower than that of Zn-Ni plating. Moreover, Co is also counted as a harmful element for human. In contrast, Fe is a safe, abundant and environmental-friendly element. Therefore, Zn-Fe plating can be considered as a candidate alternative material for Zn-Ni plating, if its corrosion resistance can be improved to a similar level.

4.1.1.3 Zn-based ternary alloy plating

Zn-Fe alloy platings are possible alternatives for Zn-Ni platings. However, its corrosion resistance is not enough, corresponding to about one third that of Zn-Ni alloy plating [6]. The anti-corrosion property of binary Zn-Fe plating may be enhanced by the addition of noble third element, Mo [15,16]. Mo is a metal element with atomic number of 42 and is a kind of Cr group element. Because Mo has high melting point and excellent mechanical properties, Mo is usually used as alloying elements for steel materials. By adding Mo to the steel material, not only the wear resistance and hardness in high temperature region increase, but also the corrosion resistance can be improved [16]. Addition of Mo in stainless steel improves corrosion resistance through an anticorrosive mechanism known as follows. When a defect occurs in the passivation film of Cr, Mo gathers in the defect portion to improve the recovery ability. Although Mo is a promising metal to improve corrosion resistance, it is difficult to manufacture by general processes such as melting and solidification since Mo has a high melting point (2,622 °C) and its processability is also low.

Electrodeposition of metallic Mo from aqueous solution is also difficult because of its highly oxidized state of molybdate ion. However, electrodeposition of metal Mo is possible under codeposition with iron-group elements, which referred to as principle of induced codeposition [17-19]. Alloy plating containing Mo and W deposited by induction codepositon is reported to exhibit noble corrosion potential as well as high corrosion resistance by forming an oxide film of Mo and W at the surface.

The electrodeposition of ternary Zn-Fe-Mo plating and its corrosion resistance have been discussed in our past study [20]. Winiarski et al. also reported the electrodeposition of Zn-based ternary alloy plating, such as Zn-Fe-Mo [15,21] and Zn-Co-Mo [22]. They reported ternary alloy plating showed higher corrosion resistance than binary Zn-Fe and Zn-Co plating by the incorporation of Mo as a third element. However, it has not been confirmed whether such ternary alloy plating possesses enough corrosion resistance to replace Zn-Ni plating in an actual corrosive environment.

4.1.2 Electrodeposition of Mo oxide

As described above, chromate treatment is mainly applied to suppress the occurrence of white rust and improve corrosion resistance in Zn and Zn-alloy plating, especially Zn-Ni and Zn-Fe. Trivalent chromate treatment is recently applied since hexavalent chromate treatment, which use Cr^{6+}, is limited in use due to RoHS and ELV regulations. The self-healing property that contributes to the corrosion resistance improvement of the hexavalent chromate film is that when the chromate film with numerous cracks on the surface is damaged, the hexavalent chromium compound forms a new protective film using moisture and Zn. However, trivalent chromate treatment has lower corrosion resistance than hexavalent chromate treatment, and does not have self-healing properties, thus a new top coating is required to ensure the required corrosion resistance.

Meanwhile, Kitamura et al. reported that molybdate ion (MoO_4^{2-}) can be reduced to Mo oxide film containing a small amount of metal Mo on the iron group metal substrate by electrodeposition [23]. This oxide film, mainly composed of MoO_2 and MoO_3, is likely to be formed by induced codeposition of molybdate ion on the surface of the iron-group metal substrate. Focused on these characteristics, it was thought that such a Mo oxide film could be formed onto the Zn-based alloy plating containing iron group elements. Since Mo is Cr group element, which is harmless to the human body, if electrodeposited Mo oxide layer has self-healing properties such as chromate conversion coating, it is estimated that it will be effective in improving the corrosion resistance of Zn-based plating and has a possibility to replace chromate treatment.

4.2 Proposed structure design of plating

In current, the use of Ni in plating is gradually becoming avoided in the plating industry because of the harmfulness of Ni to human body and the global environment. Therefore, it is necessary to find alternatives for conventional platings containing Ni using harmless elements. Thus, it is necessary to develop Ni-free plating with high corrosion resistance, especially as an alternative to Zn-Ni plating. As a possible alternative, Zn-Fe-Mo plating in which Mo was added to Zn-Fe plating was prepared by electrodeposition, and its corrosion resistance was evaluated. And in order to further improve the corrosion resistance, additional Mo-oxide layer onto Zn-Fe-Mo plating was prepared by electrodeposition, considering the compatibility with electrodeposited ternary Zn-Fe-Mo plating. The formed Mo-oxide coating is expected to decreasing corrosion rate and improving corrosion resistance of underlying Zn-Fe-Mo plating by self-healing characteristics similar to chromate conversion coating. The graphical overview of the designed plating structure is presented in Figure 4.1.

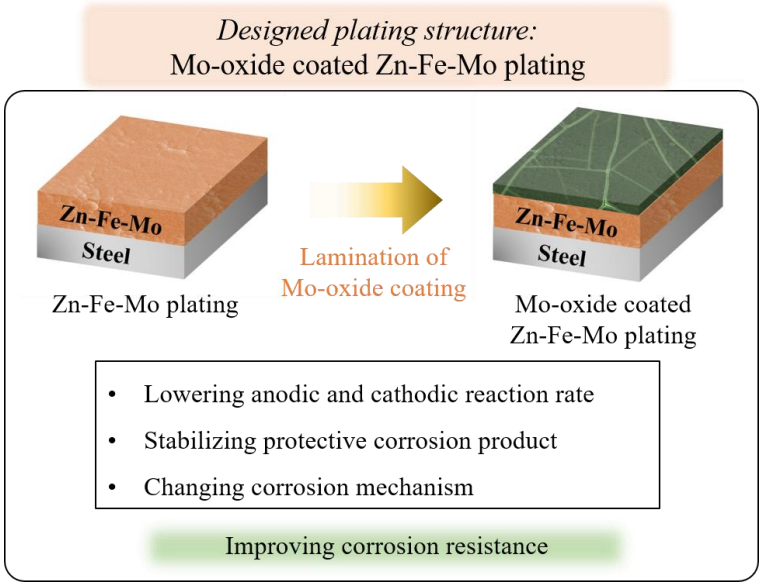

Figure 4.1 The graphical overview of the designed plating structure.

4.3 Objective of this work

Despite the superior anti-corrosion properties and widespread use of Zn-Ni plating, the harmfulness of Ni to human body has caused the demand for Ni-free alternative plating. In this respect, electrodeposited ternary Zn-Fe-Mo plating has been considered as a possible replacement for Zn-Ni plating. However, the corrosion resistance of Zn-Fe-Mo plating is still insufficient for replacing Zn-Ni plating. Therefore, as a method for improving the corrosion resistance, the lamination of the Mo oxide layer by electrodeposition is considered.

In this study, the formation of an effective multilayer structure to enhance the corrosion resistance is studied by forming a Mo oxide coating on ternary Zn-Fe-Mo plating. The electrodeposition behavior of Mo oxide coatings in a citrate bath and the effect of the substrate on the electrodeposition of Mo-oxide coating are discussed.

In addition, corrosion resistance of Mo-oxide coated plating was evaluated by electrochemical impedance spectroscopy (EIS) and cyclic corrosion test (CCT), and the influence of Mo-oxide coating on improvement of corrosion resistance was investigated by analyzing the formed corrosion products and the structure change of the plating layer as corrosion progression. Finally, the influence of Mo-oxide coating against the corrosion properties of Zn-Fe-Mo plating is discussed.

4.4 Materials, chemicals, and equipment

Materials, chemicals and equipment used in this study are listed in Table 4.1 and 4.2, respectively. All chemicals were used as purchased without any further purifications.

Table 4.1 Materials and chemicals

Materials and chemicals	Company
Tri-sodium citrate ($Na_3C_6H_5O_7$, ≥ 99.0%)	Nacalai Tesque, Inc, Japan
Zinc sulfate heptahydrate ($ZnSO_4 \cdot 6H_2O$, ≥ 99.5%)	Nacalai Tesque, Inc, Japan
Iron (II) sulfate hexahydrate ($FeSO_4 \cdot 6H_2O$, ≥ 99.0%)	Nacalai Tesque, Inc, Japan
Sodium molybdate dihydrate ($Na_2MoO_4 \cdot 2H_2O$, ≥ 98.0%)	Kishida chemical Co., Ltd Japan
Sodium sulfate (Na_2SO_4, ≥ 98.5%)	Nacalai Tesque, Inc, Japan
Sulfuric acid (H_2SO_4, 98.0%)	Nacalai Tesque, Inc, Japan
Sodium hydroxide (NaOH, ≥ 99.0%)	Nacalai Tesque, Inc, Japan
Sodium chloride (NaCl, ≥ 99.0%)	Nacalai Tesque, Inc, Japan
Commercial copper plate (B-60-P05, 99%)	Yamamoto-MS Co., Japan
Commercial steel plate (B-60-P01)	Yamamoto-MS Co., Japan

Table 4.2 Equipment

Equipments	Details	Company
Potentio/galvanostat	HZ-7000	Hokuto denko, Japan
Potentio/galvanostat	SP-150	Bio-Logic, France
Scanning electron microscope (SEM)	JSM-6330F	JEOL, Japan
Energy-dispersive spectroscopy (EDS)	SEM-EDX Type N	Hitachi, Japan
X-ray diffractometer (XRD)	Ultima IV	Rigaku, Japan
X-ray photoelectron spectroscope (XPS)	ESCALAB 250Xi	Thermo Fisher Scientific, USA

4.5 Electrodeposition of ternary Zn-Fe-Mo plating and Mo-oxide coating

4.5.1 Bath preparation

The bath compositions for Zn, Zn-Fe and Zn-Fe-Mo plating are shown in Table 4.3. Ternary Zn-Fe-Mo plating bath was prepared by dissolving 0.2 mol·dm^{-3} of $Na_3C_6H_5O_7 \cdot 2H_2O$, 0.01 mol·dm^{-3} of $Na_2MoO_4 \cdot 2H_2O$, 0.2 mol·dm^{-3} of $ZnSO_4 \cdot 7H_2O$, 0.2 mol·dm^{-3} of $FeSO_4 \cdot 7H_2O$ and 0.1 mol·dm^{-3} of Na_2SO_4 with distilled water. The bath pH was adjusted to 5.7 using distilled NaOH solution and H_2SO_4 solution according to previous study [20]. The volume of plating baths was adjusted to 100 ml. The dissolved oxygen in plating bath was removed by high purity Ar gas for 30 min before use. The bath compositions for Mo-oxide coating are shown in Table 4.4.

Table 4.3 Bath compositions of Zn, Zn-Fe and Zn-Fe-Mo plating.

	Concentration (mol·dm^{-3})		
	Zn plating	Zn-Fe plating	Zn-Fe-Mo plating
$Na_3C_6H_5O_7 \cdot 2H_2O$	-	0.2	0.2
$Na_2MoO_4 \cdot 2H_2O$	-	-	0.01
$ZnSO_4 \cdot 7H_2O$	0.7	0.2	0.2
$FeSO_4 \cdot 7H_2O$	-	0.2	0.2
Na_2SO_4	0.21	0.1	0.1
pH	3.0	5.7	5.7

Table 4.4 Bath compositions of Mo-oxide coating bath [23].

Bath composition	Concentration (mol·dm^{-3})		
	Citrate bath	Mo bath	Citrate-Mo bath
$Na_3C_6H_5O_7 \cdot 2H_2O$	0.1	-	0.1
Na_2SO_4	0.2	0.2	0.2
$Na_2MoO_4 \cdot 2H_2O$	-	0.1	0.1
pH	6.0	6.0	6.0

4.5.2 Cyclic voltammograms

CV was measured to investigate the effect of Mo addition in Zn-Fe plating bath. Conventional 3-electrode electrochemical measurement system with platinum coil as counter electrode and Ag/AgCl in sat. KCl solution as auxiliary electrode was used. Commercial Cu plate with 1×1 cm^2 was used for CV measurement of Zn-Fe and Zn-Fe-Mo plating, and steel plate was used for CV for Mo-oxide coating. CV measurements was performed with a scan rate of 5 $mV \cdot s^{-1}$ from the open circuit potential (OCP) to -1.4 V (vs. Ag/AgCl).

Figure 4.2 displays the cyclic voltammograms measured using the Zn-Fe bath and the Zn-Fe-Mo bath. The addition of 0.01 $mol \cdot dm^{-3}$ of $Na_2MoO_4 \cdot 2H_2O$ to Zn-Fe bath significantly changed the CV curve. In the Zn-Fe bath, peaks appeared at near -0.90 and -1.10 V (vs. Ag/AgCl), which correspond to the reduction peaks of metal Fe and Zn, respectively. Three oxidation peaks were also confirmed, possibly corresponding to dissolution peaks for Zn and Zn-Fe alloy phases. Meanwhile, another reduction peak near -0.45 V appeared in the case of Zn-Fe-Mo bath, which is considered as a codeposition peak for Fe and Mo. Moreover, the deposition potential of metal Zn and Fe somewhat moved toward a more cathodic potential direction, anticipated as effects of formed citrate-metal complex ions.

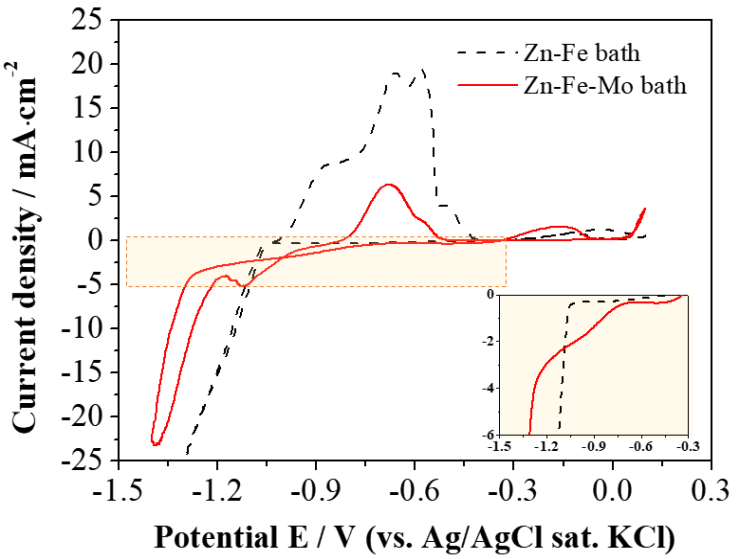

Figure 4.2 Cyclic voltammograms measured at Zn-Fe and Zn-Fe-Mo bath.
(Cathode: Cu plate, scan rate: 5$mV \cdot s^{-1}$)

The cathodic parts of cyclic voltammograms measured in Mo-oxide coating bath is shown in Figure 4.3. Based on our preliminary experiment, because metallic Mo-oxide layer was electrodeposited only on the substrates containing iron-group elements (Ni plate and steel plate), thus steel plate was selected as cathode for CV measurements. In the Citrate bath, which did not contain molybdate ions, only the hydrogen evolution reaction at near -1.1 V appeared. In the Mo bath and Citrate-Mo bath, one reduction peak was confirmed at near -0.7 V, possibly corresponding to the reduction peak of molybdate ions. However, a plateau was continued until -1.2 V for Mo bath, which implies the adsorption of incompletely reduced excessive molybdate ion at cathode surface. The addition of 0.1 mol·dm^{-3} of $Na_3C_6H_5O_7 \cdot 2H_2O$ in the Mo bath increased cathodic current significantly. This may be caused by the formation citrate-molybdate complex ions at pH near 6.0 [24], which can increase deposition rate of molybdate ion to molybdenum oxide by suppressing excessive adsorption of molybdate ion at the cathode surface.

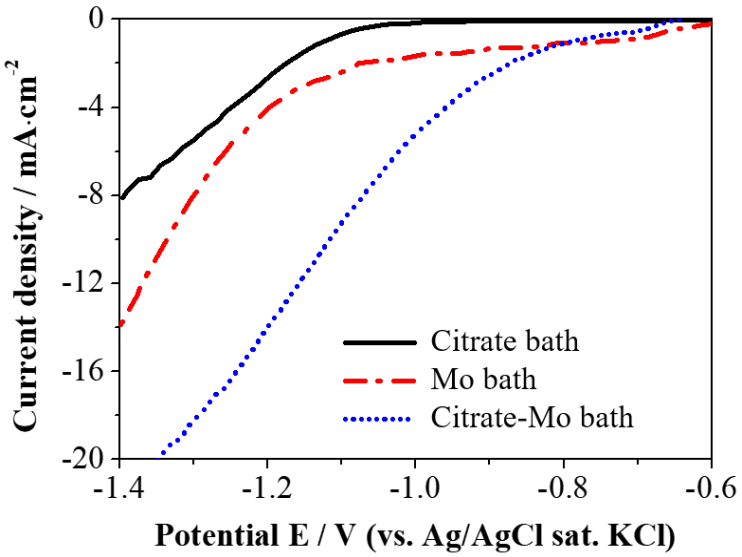

Figure 4.3 Linear sweep voltammograms obtained at Citrate bath, Mo bath and Citrate-Mo bath. (Cathode: steel plate, scan rate: 5mV·s^{-1})

4.5.3 Electrodeposition process

Electrodeposition of ternary Zn-Fe-Mo plating and Mo-oxide coating was prepared using a potentio/galvanostat. Commercial steel plates and Pt coil were used as the cathode and anode, respectively. The steel plates were washed with ethanol and dipped in 10 wt.% H_2SO_4 solution to remove the oxides on the surface before use. The electrodeposition area was kept to be 2×2 cm^2 by masking with insulating tape. A galvanostatic deposition was performed at -10 $mA \cdot cm^{-2}$ and a fixed electric charge of 35 $C \cdot cm^{-2}$ (approximate plating thickness of 10 μm) was applied for ternary Zn-Fe-Mo plating. For the Mo-oxide coated Zn-Fe-Mo plating, electrodeposited ternary Zn-Fe-Mo plating was used for cathode. Two kinds of electrodeposition methods were used: galvanostatic deposition at -2 $mA \cdot cm^{-2}$ and potentiostatic deposition at -1.2 V (vs. Ag/AgCl), each 30 min. Mo oxide coating was also prepared on Zn and Zn-Fe plating using the prior method for investigating the influence of substrate against the deposition of the Mo-oxide layer. Since the potential of Zn, Zn-Fe and Zn-Fe-Mo plating is different, galvanostatic deposition at -2 $mA \cdot cm^{-2}$ was used.

4.5.4 Characterization

4.5.4.1 Morphology observation

The surface and cross-sectional microstructures of the plating specimens were observed using FE-SEM. Optical photographs and FE-SEM micrographs of Zn-Fe-Mo plating and Mo-oxide coated Zn-Fe-Mo plating surfaces are presented in Figure 4.4. A gray metallic luster surface of ternary Zn-Fe-Mo plating was confirmed. The microstructure exhibited a fine and smooth microstructure. Mo-oxide coated Zn-Fe-Mo plating revealed green metallic luster surface. Mo-oxide coating was well-adhered to Zn-Fe-Mo plating surface but some micro-sized cracks existed on its surface according to observations by SEM. These cracks may have been formed by the high residual stress of Mo-oxide layer. Kitamura et al. [23] reported that metallic luster Mo-oxide layer containing a few atomic layers of metal Mo can be electrodeposited only on iron-group metal substrates (Ni, Co and Fe). This metallic luster of Mo-oxide coating deposited in this study is presumed to be owing to the

reduction of the few metallic Mo on the interface of Zn-Fe-Mo plating, owing to existence of metal Fe in the plating.

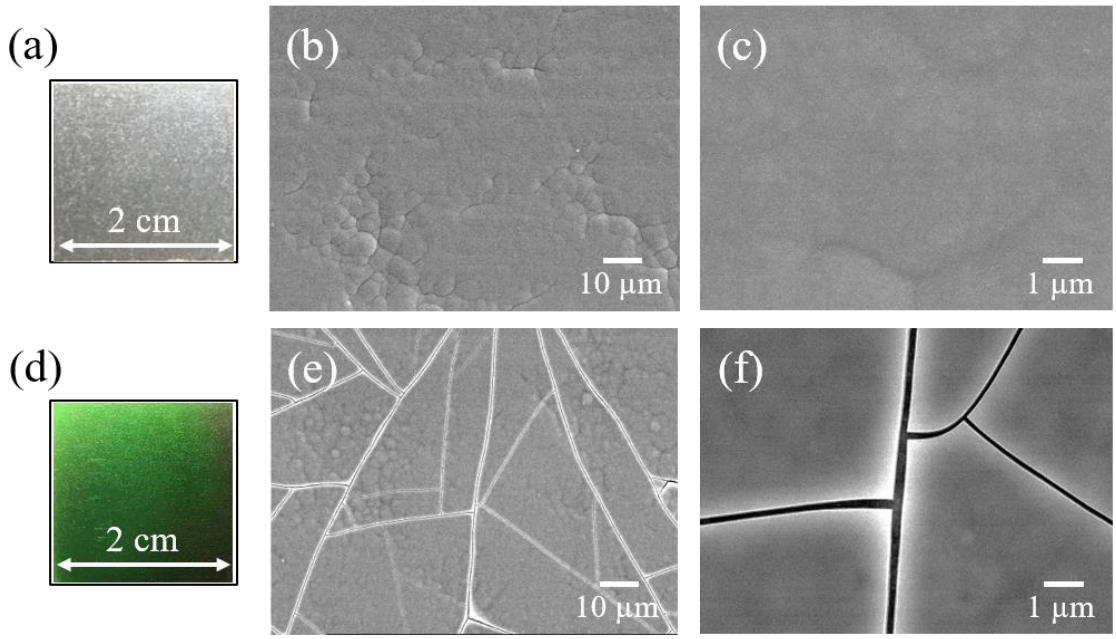

Figure 4.4 Optical photographs and SEM micrographs for ternary Zn-Fe-Mo plating (a), (b), (c), Mo-oxide coated Zn-Fe-Mo plating (d), (e) and (f).

Fukushima et al. [25] reported the absorbed hydrogen at deposited iron-group metal, H(Me) can act as a catalyst for reduction of MoO_4^{2-} to metal Mo as following:

$$Me^{2+} + 2e^- \rightarrow Me \qquad (4.1)$$

$$H^+ + e^- + Me \rightarrow H(Me) \qquad (4.2)$$

$$MoO_4^{2-} + (6-n)e^- \rightarrow Mo^{n+} \text{ oxide(hydroxide)} \qquad (4.3)$$

$$Mo^{n+} \text{ oxide(hydroxide)} + nH(Me) \rightarrow Mo(Me) \qquad (4.4)$$

here, Me is an iron-group metal, H(Me) is absorbed atomic hydrogen on a reduced iron-group metal, n is ionic valence of the molybdenum intermediate compounds ($0 < n < 6$), and Mo(Me) is electrodeposited metal Mo. Considering their research results, it was presumed that metallic lust Mo-oxide coating on the Zn-Fe-Mo plating was possibly deposited by the induced reduction of metal Mo at the Fe site onto the

Zn-Fe-Mo plating surface. It was also anticipated that good adhesion between Mo-oxide coating and ternary Zn-Fe-Mo plating was possible due to this reaction. The thickness of deposited Mo-oxide coating was approximately 300 nm, confirmed by cross-sectional SEM image in Figure 4.5. However, Mo-oxide coated Zn plating showed a pale green with non-metallic appearance as shown in Figure 4.6 (b). The SEM image showed the Mo-oxide did not adhere to the underlying Zn plating. Meanwhile, Mo-oxide well adhered on Zn-Fe plating with slightly metallic-lust appearance (Figure 4.6(d)). These results proves that the existence of iron-group element in the underlying substrate was essential for obtaining metallic lust and well-adhered Mo-oxide. However, the best adherence seemed to be obtained when the Mo-oxide coating was prepared on the Zn-Fe-Mo plating (Figure 4.6 (f)). The smoother surface may have been advantageous for the adhesion of the Mo-oxide coating.

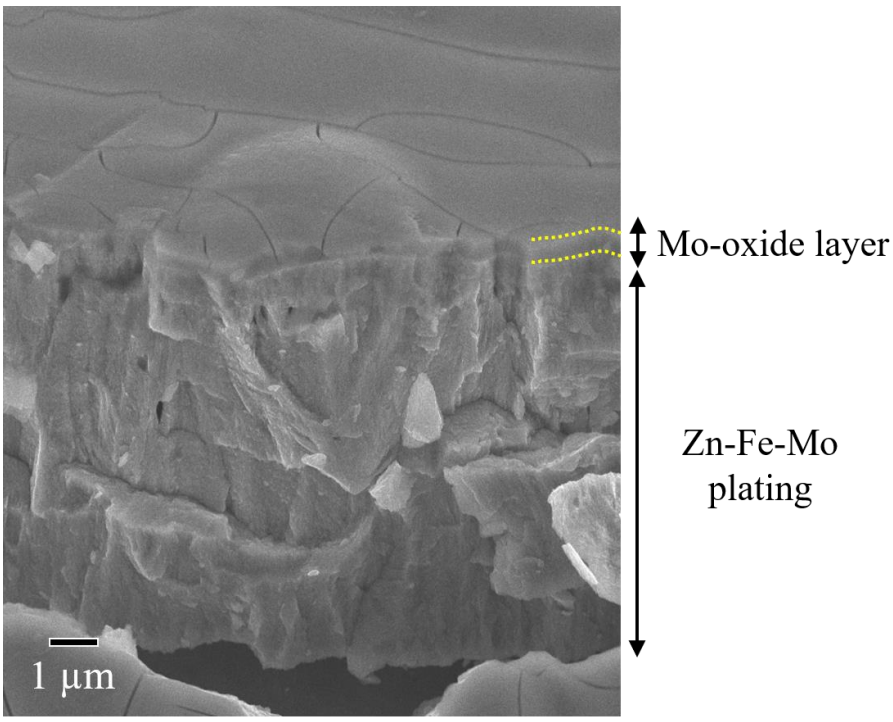

Figure 4.5 Cross-sectional SEM micrographs for Mo-oxide coated Zn-Fe-Mo plating.

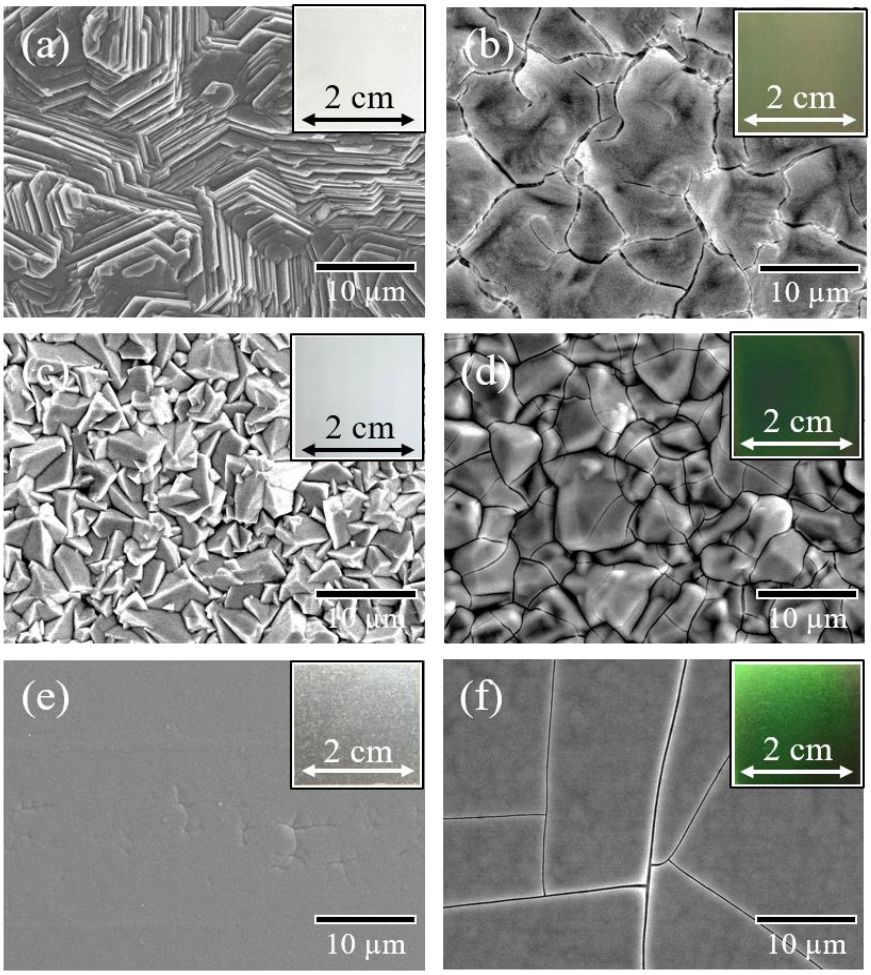

Figure 4.6 SEM micrographs and optical photographs (inside): (a) Zn plating, (b) Mo-oxide coated Zn plating, (c) Zn-Fe plating, (d) Mo-oxide coated Zn-Fe plating, (e) Zn-Fe-Mo plating and (f) Zn-Fe-Mo plating with Mo oxide coating (Mo oxide was electrodeposited at -2 $mA \cdot cm^{-2}$ for 30 min).

4.5.4.2 Crystalline structures analysis

Crystalline structures of plating specimens were characterized by XRD equipped with Cu-Kα radiation source (λ = 0.154056 nm). The measurement range, scanning speed, accelerating voltage and accelerating current were $30° \leq 2\theta \leq 100°$, 2.0°/min, 40 kV and 30 mA, respectively.

X-ray diffraction patterns for plating specimens are shown in Figure 4.7. The peaks for Zn and Fe_3Mo along with Fe from the steel substrate were detected. However, the peak of pure Mo was not detected. The Mo in ternary Zn-Fe-Mo plating

may exist as Fe-Mo alloy phase or as a solid-solution in Zn lattice [21]. Moreover, the difference in crystalline structure by Mo-oxide coating on Zn-Fe-Mo plating was not well distinguished. The crystalline structure of Mo-oxide coating is presumed to be exist as MoO_2 and MoO_3, including a few amounts of metal Mo at the interface between Zn-Fe-Mo plating and Mo-oxide coating [23]; however, diffraction was too weak to detect this layer possibly due to its thin thickness. Therefore, XPS measurement was conducted in a different section afterwards to investigate the chemical state of Mo in Mo-oxide coating.

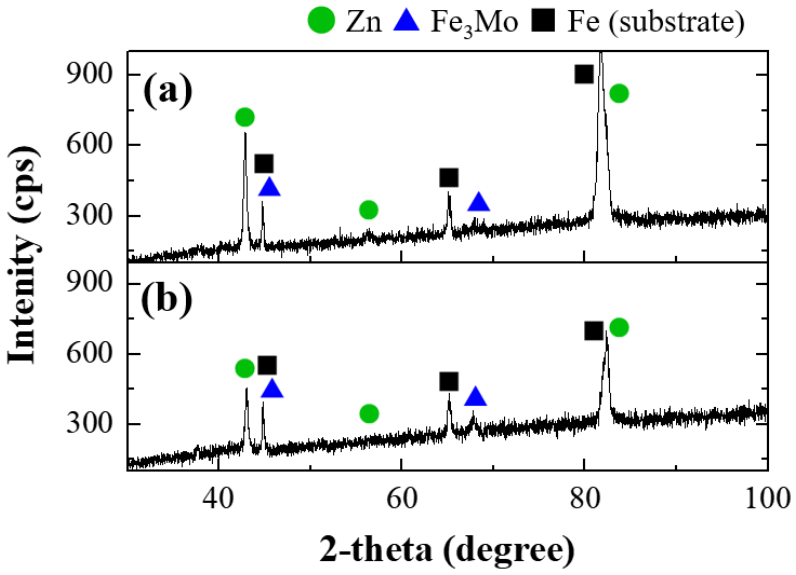

Figure 4.7 X-ray diffraction patterns: (a) Zn-Fe-Mo plating and (b) Mo-oxide coated Zn-Fe-Mo plating.

4.5.4.3 Elemental compositions and chemical states analysis

The elemental compositions of the Zn-Fe-Mo and Mo-oxide coated Zn-Fe-Mo plating specimens were analyzed by EDS. The chemical states of metal components of the surface and inside of Zn-Fe-Mo and Mo-oxide coated Zn-Fe-Mo were analyzed using XPS equipped with Al-kα source (1486 eV). High-resolution scans for Zn LMM, Fe 2p, Mo 3d and O 1s were measured at pass energy of 20 eV, in step of 0.05 eV with dwell time of 50 msec. Ar etching was conducted with 1000 eV Ar ion beam for comparing chemical states of top surface and inside of plating layer.

EDS analysis results presented in Table 4.5 showed ternary Zn-Fe-Mo plating consist of relatively high O content, possibly caused by metal oxides existing at the plating surface. Meanwhile, Mo-oxide coated Zn-Fe-Mo plating consists of high Mo and O contents, 11.87 and 63.49 at.%, respectively. This implies that the Mo-oxide layer was deposited onto the surface of Zn-Fe-Mo plating.

Table 4.5 Elemental compositions for ternary Zn-Fe-Mo plating and Mo-oxide coated Zn-Fe-Mo plating measured by EDS.

Composition [at.%]	Zn-Fe-Mo plating	Mo-oxide coated Zn-Fe-Mo plating
Zn	75.71	22.40
Fe	5.03	1.34
Mo	2.08	11.87
O	17.18	63.49

XPS measurement results of Zn-Fe-Mo platings are shown in Figure 4.8. Measured Zn LMM spectra is shown in Figure 4.8(a). Because of only slight energy shift at Zn 2p core level region, Zn LMM auger peaks were investigated to verify the chemical state of Zn [16,22]. After Ar etching for 3 min, peaks corresponding to metal Zn (distinguishing peaks originated from 992.0 and 995.6 eV) were identified. Zn is expected to exist mainly in the metallic state since the inside of the plating should be forming alloys, thus, the result seems to be reasonable. Meanwhile, peaks correspond to Zn^{2+} appeared at lower binding energy region (near 989.3 eV) before Ar etching,

which can be presumed Zn exist as oxide or hydroxide states at top surface. Fe 2p core level spectra shown in Figure 4.8(b) indicates Fe slightly exists as oxidized state (Fe_2O_3, binding energy of 711.3 eV) at top surface and mainly as metallic Fe (707.1 eV) inside the plating [26]. This also well corresponds to the anticipation that the surface is oxidized and the inside is forming alloys. Figure 4.8(c) reveals Mo 3d core level spectra obtained before and after Ar etching. Result shows that Mo hardly exists at top surface, while Mo exists as metallic Mo (binding energy of 287.8 eV) at inside of plating layer [16,23]. However, O 1s core level spectra reveals that metal hydroxide or carbonates, possibly caused by slightly corroded Zn were exist at plating surface. And presence of metal oxide was presumed to be caused by presence of a few amount of incompletely reduced molybdate ions. XPS measurement results of ternary Zn-Fe-Mo plating show that the outer surface is mainly comprised of oxides and hydroxides of Zn, while the inside of the plating layer is composed as highly metallic alloys. Mo was also obtained in the metal state by induced codeposition from molybdate ions in the presence of Fe.

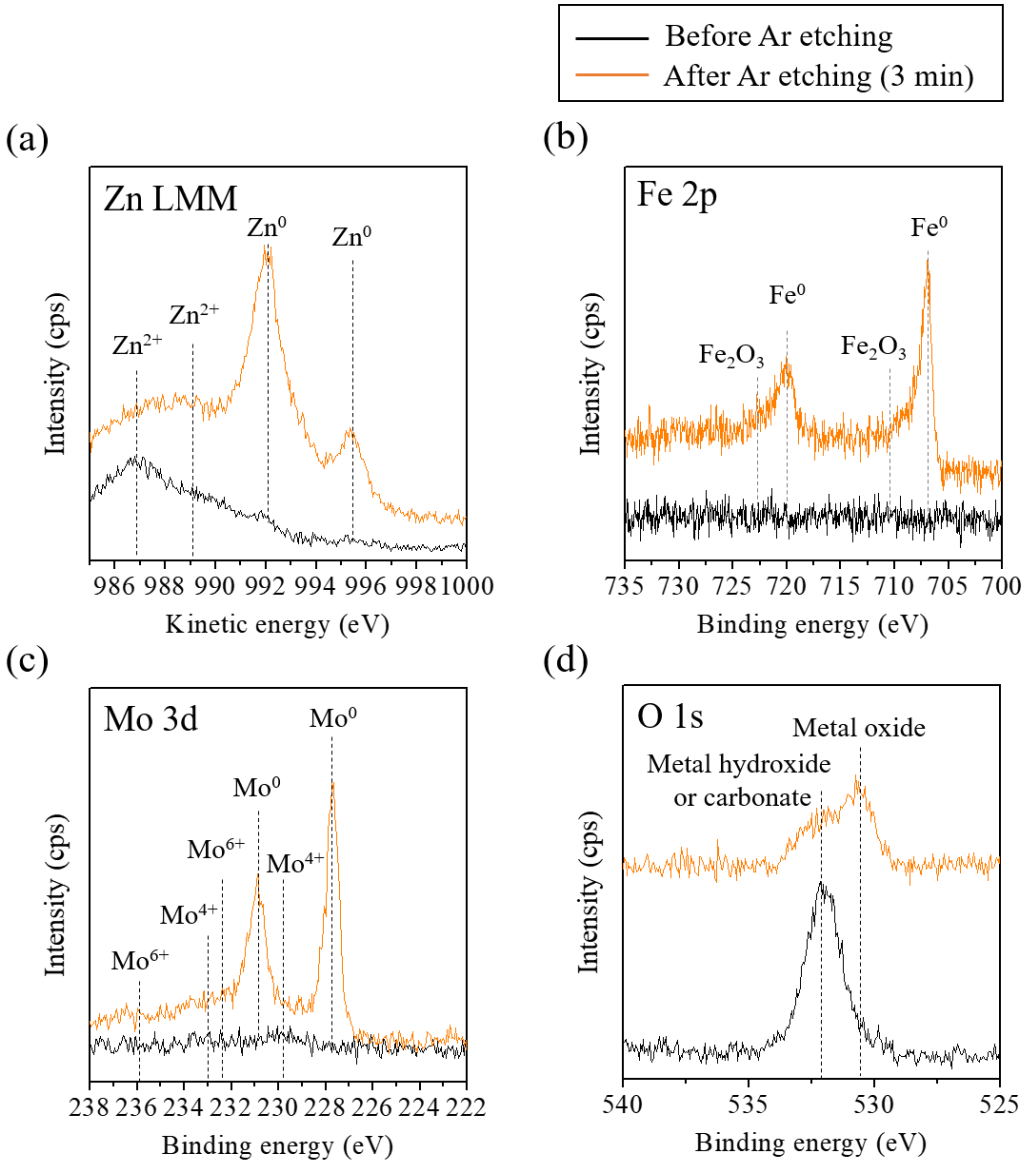

Figure 4.8 High-resolution XPS spectra for ternary Zn-Fe-Mo plating before and after Ar etching: (a) Zn LMM, (b) Fe 2p, (c) Mo 3d and (d) O 1s scans, respectively.

Mo 3d core level spectra for Mo-oxide coating is shown in Figure 4.9. Non-metal state Mo is obviously detected in contrast to the Zn-Fe-Mo plating without the additional coating. This indicates that an Mo-oxide layer was successfully formed by the electrodeposition process. Moreover, the results show that Mo-oxide coating was comprised mainly of MoO_2 (binding energy of ~ 229.1 eV and ~232.9 eV) and MoO_3 (binding energy of ~232.3 eV and ~235.9 eV), and metal Mo (binding energy of ~228.1 eV and ~ 231.6 eV) [23] was hardly presented even after Ar etching for 5 min.

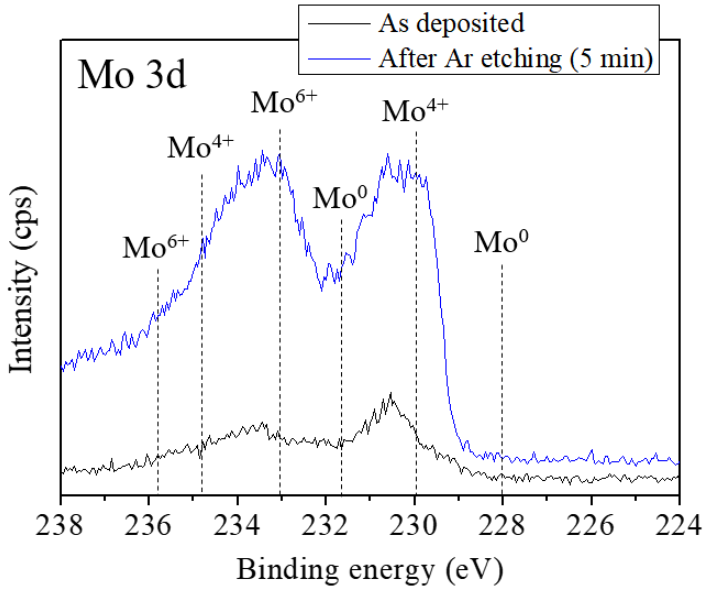

Figure 4.9 High-resolution XPS spectra for Mo 3d of Mo-oxide coated Zn-Fe-Mo plating before and after Ar etching.

4.6 Evaluation of corrosion resistance

4.6.1 EIS

EIS was conducted to evaluate the corrosion resistance of the plating specimens. The EC-Lab software was used to analysis of measure data. EIS measurements were conducted in 100 ml of 3 wt.% NaCl solution at room temperature. Measurement conditions were as follows: scan range of 10 kHz to 10 mHz with AC 10 mV amplitude. Each measurement was performed after stabilizing the open circuit potential.

Figure 4.10 exhibits the EIS results of Zn, Zn-Fe, Zn-Fe-Mo plating and Mo-oxide coated Zn-Fe-Mo plating in 3 mass% NaCl solution.

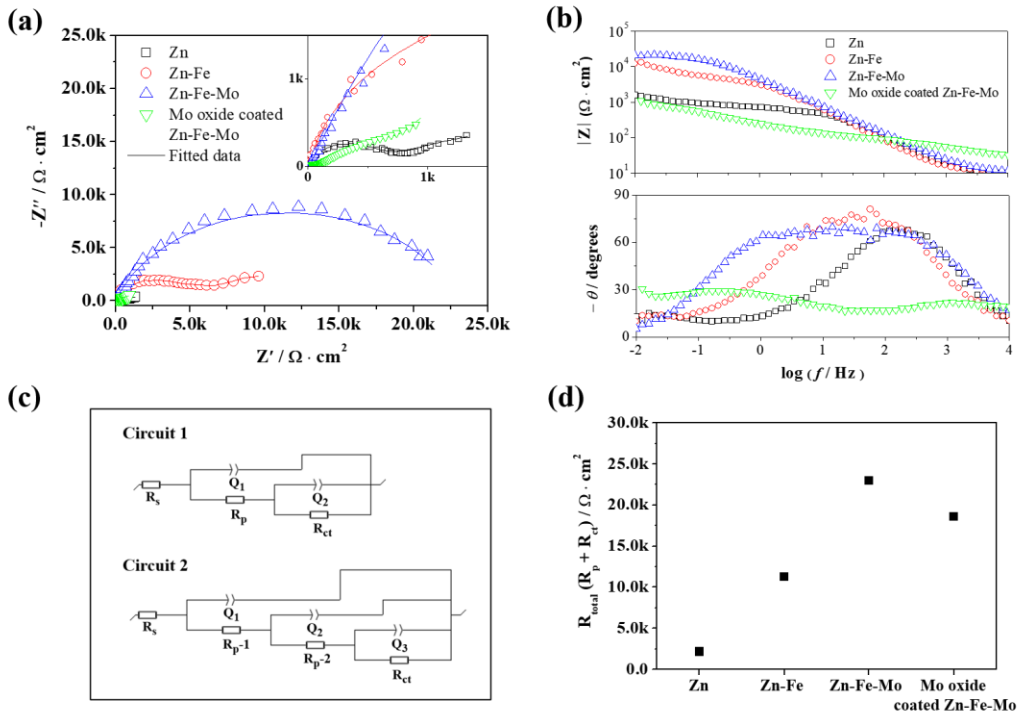

Figure 4.10 EIS measurement results: (a) Nyquist plots, (b) bode impedance (upper) and phase (lower) plots, (c) used equivalent circuits and (d) calculated R_{total} (R_p + R_{ct}) of each plating specimen.

The equivalent circuit 1 shown in Figure 4.10(c) was used for data fitting for Zn, Zn-Fe and Zn-Fe-Mo plating and circuit 2 was used for Mo-oxide coated Zn-Fe-Mo plating. R_s is the resistance of electrolyte, R_p is correspond to the resistance of

pores due to the formed porous corrosion product layer on surface, and Q_1 corresponds to capacitance of this layer. R_{ct} is the charge-transfer resistance by the anodic dissolution of metals at the interface and Q_2 is capacitance of double-layer. Considering the inhomogeneity of plating surface, a constant phase element (CPE) was adapted instead of capacitor. For Mo-oxide coated ternary Zn-Fe-Mo plating, the measurement results with scan range up to 1 mHz showed a third time constant at near 10 mHz; possibly attributed to the underlying ternary Zn-Fe-Mo plating. Thus, the equivalent circuit 2 was used in consideration of the multi-layer structure. In this circuit, R_p-1 corresponds to the pore resistance of the cracked portion of Mo-oxide coating, R_p-2 is for the formed corrosion products from the underlying plating, and R_{ct} is charge transfer resistance of ternary Zn-Fe-Mo plating. Nyquist plots for Zn and Zn-Fe plating shown in Figure 4.10(a) showed well-defined two semi-circles. For Zn-Fe-Mo plating, it seemed that the two semi-circles overlap. R_{total} of Zn-Fe-Mo plating exhibited higher value (22,981 $\Omega \cdot cm^2$) than that of Zn (2,163 $\Omega \cdot cm^2$) and Zn-Fe plating (11,227 $\Omega \cdot cm^2$). This indicates the addition of Mo to Zn-Fe plating is helpful to enhance the surface barrier properties. However, EIS measurement results for Mo-oxide coated Zn-Fe-Mo plating showed relatively lower resistance value than other plating (R_p-1: 99.97 $\Omega \cdot cm^2$, R_p-2: 1,308 $\Omega \cdot cm^2$ and R_{ct}: 17,175 $\Omega \cdot cm^2$). It is presumed that the surface barrier properties of Mo-oxide coating itself is not so excellent without the resistance from the underlying Zn-Fe-Mo plating.

4.6.2 CCT

The corrosion resistance of Zn-Fe-Mo plating and Mo-oxide coated Zn-Fe-Mo plating were evaluated by CCT, which is a wet-dry cyclic corrosion accelerating test method according to ASTM D 6899 standard. Electrodeposited Zn, Zn-Fe plating (thickness approximately 10 μm) and respective Mo-oxide coated platings were also tested for the comparison of corrosion resistance. The exposed area for CCT was kept at 2×2 cm^2 and their edges were masked with insulating tape. Test specimens was observed every 3 cycles (corresponding to 24 h) to determine the times for initial red rust was generated. The test conditions of CCT are shown in Table 4.6.

Table 4.6 Corrosion test conditions for 1 cycle of cyclic corrosion test (CCT).

Operating conditions	Test conditions
Salt spray (2 hour)	T= 35 °C, Spray 5 wt.% NaCl sol., R.H: 100 %
Dry (4 hour)	T= 60 °C, R.H: 25 %
Humid (2 hour)	T= 50 °C, R.H: 95 %

CCT results for plating specimens with and without Mo-oxide coating are presented in Figure 4.11. Initial red rust appeared after 12 cycles (96 h) for both Zn and Zn-Fe plating, while it appeared after 6 cycles (48 h) for Zn-Fe-Mo plating. Also, the corroded area of Zn-Fe-Mo plating spread faster compared to Zn plating. In contrast to the expectations from EIS measurements, the corrosion resistance seemed to decrease by the addition of Mo into the Zn-Fe plating.

Meanwhile, Mo-oxide coated Zn-Fe-Mo plating showed significantly enhanced corrosion resistance. Initial red rust appeared after 75 cycle (deposition condition: -2 $mA \cdot cm^{-2}$) and 60 cycles (deposition condition: -1.2 V), respectively. This result is also contrast to the expected result from the EIS measurements. Observed corrosion progress in surface showed only as local corrosion with fewer corrosion products on the surface of Mo-oxide coated Zn-Fe-Mo plating while rapid appearance of white rust was observed on the surface of Zn-Fe-Mo plating. However, Mo-oxide coated Zn plating showed only slight improvement in anti-corrosion properties, implying that the Mo-oxide coating itself is not the main cause for the improvement in corrosion resistance. Meanwhile, the corrosion progression of Mo-oxide coated Zn-Fe plating was observed as local corrosion with slow expansion of white rust, similar to Mo-oxide coated Zn-Fe-Mo plating. This tendency was observed only when the substrate for Mo-oxide coating was Zn-Fe and Zn-Fe-Mo plating. The existence of Fe in the plating is expected to be responsible for this tendency. The results indicate that the corrosion resistance significantly improves in case when underlying plating with small roughness and well-adhered Mo-oxide coating was deposited with the help of underlying plating containing Fe.

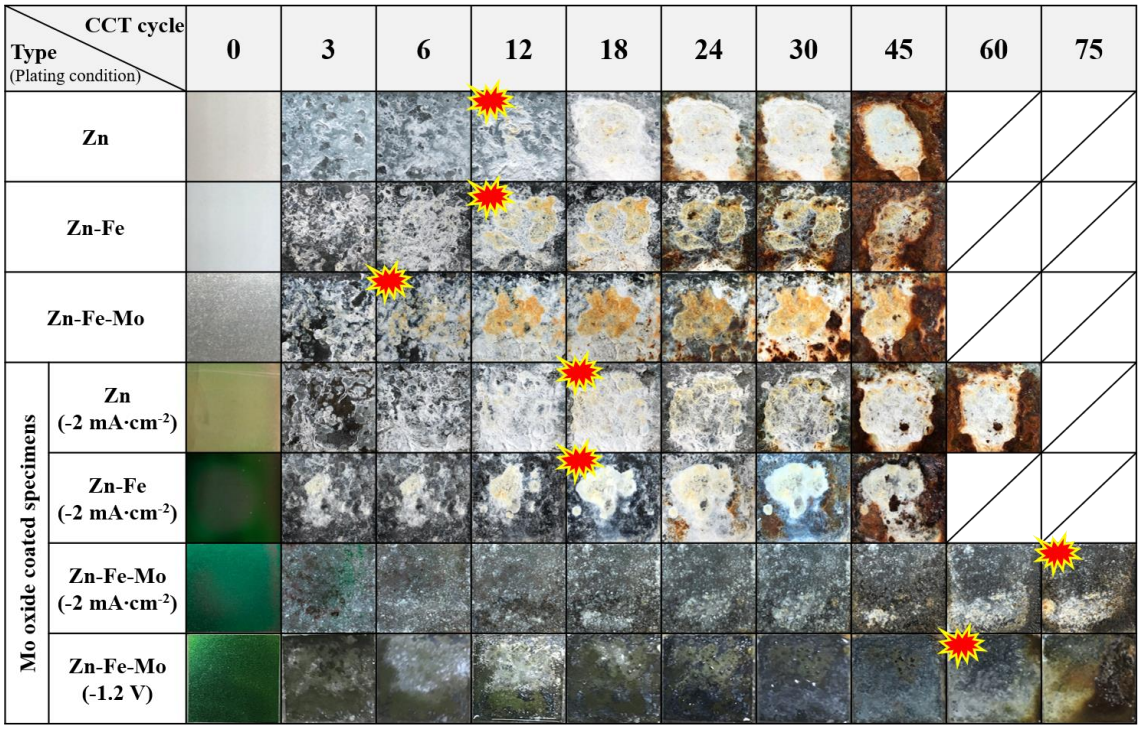

Figure 4.11 Cyclic corrosion test results of Zn, Zn-Fe, Zn-Fe-Mo plating, and respective Mo oxide coated plating (1 CCT cycle correspond to 8 h and symbols indicate times for initially red rust appeared).

4.7 Characterization of corrosion behavior as corrosion progress

To clarify the corrosion mechanism of Mo-oxide coated Zn-Fe-Mo plating, mutual relationship between Mo-oxide coating and underlying ternary Zn-Fe-Mo plating were investigated. For this, formed the corrosion were analyzed. The crystalline phases, cross-sectional micrographs and elemental compositions were investigated after 15 and 30 cycles of CCT.

Figure 4.12 shows the X-ray diffraction patterns of the corrosion products for Zn-Fe-Mo plating and Mo-oxide coated Zn-Fe-Mo plating after CCT. At the Zn-Fe-Mo plating, almost metal Zn peaks disappeared and peaks of ZnO appeared after 15 cycles of CCT. White corrosion products exist on the surface of Zn-Fe-Mo plating after CCT are considered as ZnO phase. The ZnO phase can be formed by the reaction of eluted Zn ion from anodic site of plating surface and hydroxide ion formed by the oxygen reduction reaction at cathodic sites. The formed $Zn(OH)_2$ easily dehydrated to ZnO by following reaction:

$$Zn\ (s) + \frac{1}{2}O_2 + H_2O \rightarrow Zn(OH)_2\ (s) \rightarrow ZnO\ (s) + H_2O \quad (4.5)$$

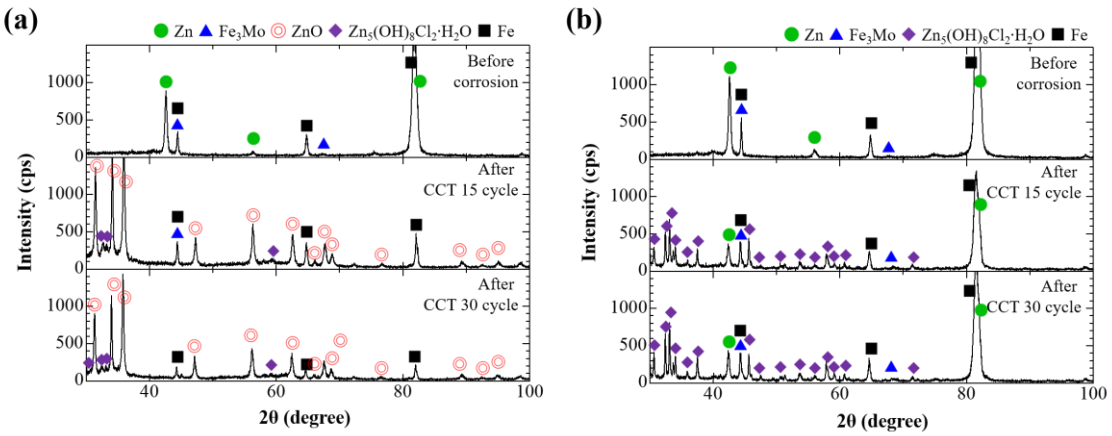

Figure 4.12. X-ray diffraction patterns before and after cyclic corrosion test: (a) Zn-Fe-Mo plating and (b) Mo-oxide coated Zn-Fe-Mo plating.

Meanwhile, the $Zn_5(OH)_8{\cdot}Cl_2{\cdot}H_2O$ (simonkolleite) phase was confirmed as corrosion products of Mo-oxide coated Zn-Fe-Mo plating. This phase has a dense structure that contributes to enhancing corrosion resistance of Zn-based coatings, as already has been reported by other researchers [27-30]. This phase forms in high

chloride ion concentrated corrosion environment, by immigration of chloride ion to anodic sites of Zn likes the following reaction:

$$5Zn^{2+} + H_2O + 8OH^- + 2Cl^- \rightarrow Zn_5(OH)_8Cl_2 \cdot H_2O\ (s) \quad (4.6)$$

Moreover, the metal Zn peaks at 43.45 and 82.65° (corresponding to (101) and (112) planes of Zn, respectively) still exist after CCT 30 cycles. This implies the Zn-Fe-Mo plating layer remains owing to the protection effect of the dense corrosion products. Therefore, Mo-oxide coating may be inducing the transformation of Zn corrosion products from ZnO to $Zn_5(OH)_8 \cdot Cl_2 \cdot H_2O$ phase, thereby enhancing the corrosion resistance of the overall plating through the densification of the Zn corrosion products layer. Figure 4.13 reveals the comparative cross-section of Zn-Fe-Mo and Mo-oxide coated Zn-Fe-Mo plating during corrosion progression. In the absence of the Mo-oxide coating, the plating layer rapidly corroded and the formed corrosion products at top surface grew thicker than 10 μm. Due to the non-dense structure of the ZnO phase, the corrosion factor can easily penetrate into the steel plate (substrate) under the plating layer in CCT 30 cycles and exhibits a large crack at the plating-steel plate interface. This is evidenced by the result of EDS point analysis results shown in Table 4.7. Point 1, 2, 5 and 6 exhibited a Zn/O ratio similar to 1 and Cl was hardly detected, which means ZnO was mainly formed as the corrosion product. The Fe content at point 2 and 6 showed 9.56 and 12.81 at.%, respectively, which considered to contain the corrosion products of Fe, because this value was higher than Fe content of pristine Zn-Fe-Mo plating (approximately 5-6 at.%). Mo was hardly confirmed in both corrosion products and in the remained Zn-Fe-Mo plating. Meanwhile, high content of Cl (2.83 at.%) and Mo (0.32 at.%) were confirmed in point 3 of the Mo-oxide coated Zn-Fe-Mo plating after CCT 15 cycles. The concentration of Cl at point 7 further increased to 9.96 at.% after CCT 30 cycles. The formed corrosion products consist of a low Zn/O ratio phase close to 0.5. These results support the idea that a $Zn_5(OH)_8 \cdot Cl_2 \cdot H_2O$ phase formed instead of ZnO phase. The Zn-Fe-Mo plating seems to hardly corrode from the XRD and EDS results (point 4 and 8). Therefore, the formation of $Zn_5(OH)_8 \cdot Cl_2 \cdot H_2O$ phase must have played a major role in improving the corrosion resistance, by serving a barrier for corrosion factors.

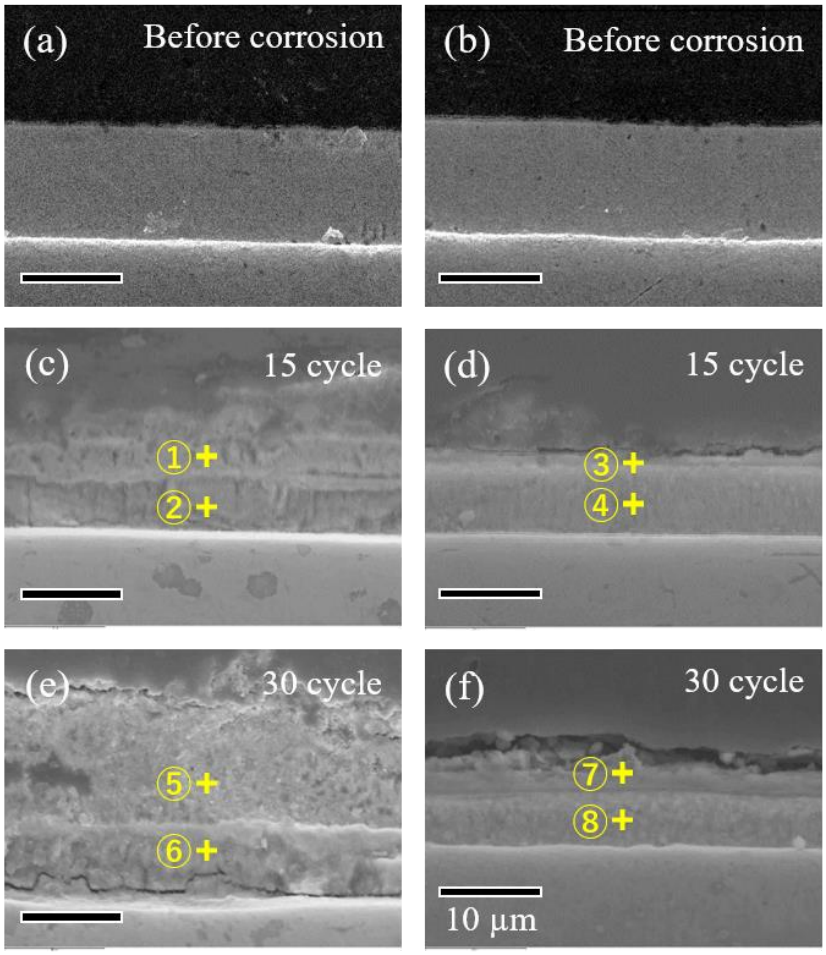

Figure 4.13 Cross-sectional SEM micrographs as cyclic corrosion test progress: (a, c, e) Zn-Fe-Mo plating and (b, d, f) Mo-oxide coated Zn-Fe-Mo plating.

Table 4.7 EDS elemental analysis results of cross section shown in Figure 4.13.

(At.%)	Zn	Fe	Mo	O	Cl	Zn/O ratio
Point 1	47.10	4.77	0.00	47.62	0.51	0.99
Point 2	43.32	9.56	0.10	46.21	0.81	0.94
Point 3	29.75	1.04	0.32	66.06	2.83	0.45
Point 4	50.76	6.54	2.69	39.20	0.82	1.29
Point 5	43.28	2.61	0.00	53.62	0.49	0.81
Point 6	36.12	12.81	0.03	50.51	0.53	0.72
Point 7	31.06	1.24	0.23	57.51	9.96	0.54
Point 8	58.60	5.54	1.80	33.67	0.39	1.74

4.8 The effect of Mo-oxide coating in improvement of corrosion resistance

As explained in the previous section, one of the major reasons for improving the corrosion resistance of Mo-oxide coated ternary Zn-Fe-Mo plating owes to the existence of a protective corrosion product of Zn, namely $Zn_5(OH)_8 \cdot Cl_2 \cdot H_2O$ phase. However, even the corrosion test condition was same for both plating, $Zn_5(OH)_8 \cdot Cl_2 \cdot H_2O$ phase was only confirmed in the Mo-oxide coated Zn-Fe-Mo plating. The guessed two reasons were inferred as follows:

1. Formation of locally high Cl^- concentration areas by minimizing surface corrosion area.
2. Lowered pH at plating surface by retarding oxygen reduction rate.

By forming less-conductive Mo-oxide coating over the plating, the anodic dissolution rate and oxygen reduction rate were impeded at the surface by minimizing the area for corrosion reaction. The corrosion reaction is likely to be started at the cracked-portion of Mo-oxide coating, and locally eluted Zn ions from underlying plating must attracted Cl ions, forming locally high Cl concentration in these areas. This assumption was well demonstrated by the EDS mapping results for Mo-oxide coated Zn-Fe-Mo plating measured after CCT 1 cycle shown in Figure 4.14.

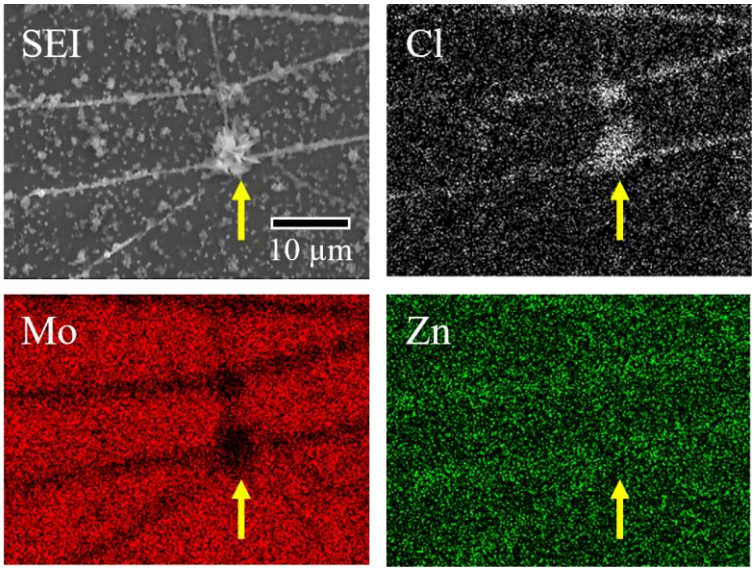

Figure 4.14 EDS mapping for Mo-oxide coated Zn-Fe-Mo plating after 1 cycle of cyclic corrosion test.

It was confirmed from EDS results that Cl ion was concentrated in the cracked-portion of Mo-oxide coating. And slightly high intensity of Zn was detected as same portion. Such corrosion environment induces the formation of $Zn_5(OH)_8 \cdot Cl_2 \cdot H_2O$ phase according to reference [31].

EDS results of the cross section of the platings provides more evidence for this assumption. In case of Zn-Fe-Mo plating without Mo-oxide coating, the influence of Cl and Mo on the corrosion product layer could not be confirmed (Figure 4.15) after CCT of 15 and 30 cycles.

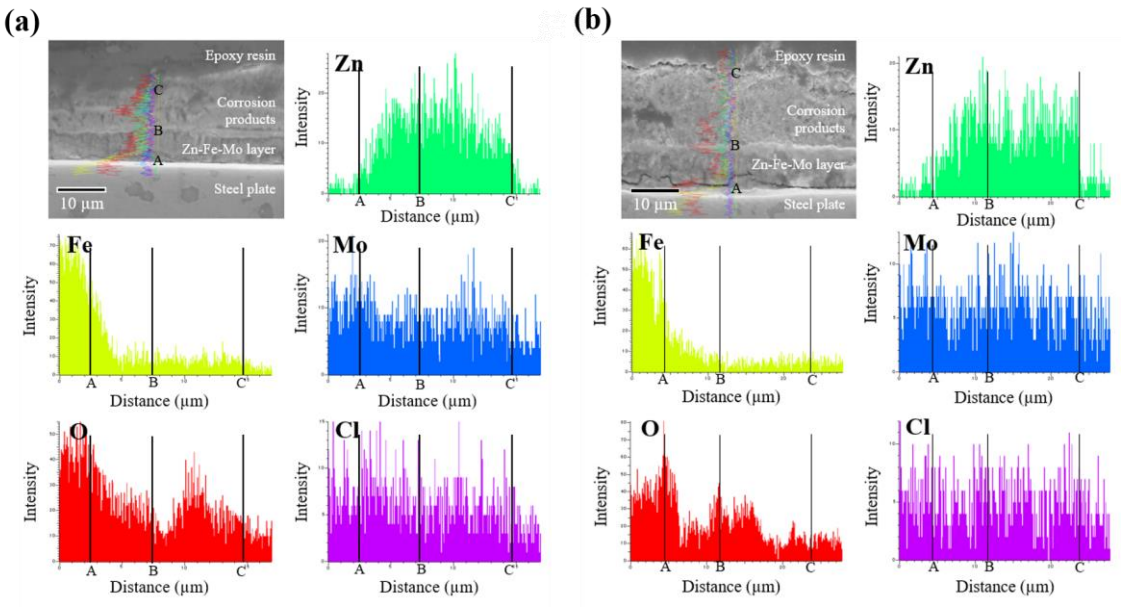

Figure 4.15 EDS line analysis results for Zn-Fe-Mo plating after cyclic corrosion test: (a) after 15 cycles and (b) 30 cycles.

Meanwhile, after CCT 15 cycles for Mo-oxide coated Zn-Fe-Mo plating, a thin Mo-rich layer on the surface of plating existed (Figure 4.16(a)). This Mo-oxide layer could be recognized more distinctively after CCT 30 cycles, and corrosion products of Zn with high concentration of Cl was also confirmed on the top of Mo-oxide coating (Figure 4.16 (a)). From the concentration gradient of Cl ion throughout this layer, local micro-corrosion of Zn from Zn-Fe-Mo plating at cracked-portion of Mo-oxide coating attracted Cl ions to this defect sites. This induced the formation of $Zn_5(OH)_8 \cdot Cl_2 \cdot H_2O$ phase and suppressed the oxygen diffusion reaction through the corrosion product.

This shall contribute to reduction of the cathodic reaction rate [32,33], which possibly lowered the surface pH. The phenomenon in which the Zn corrosion product layer is formed from the cracked-portion of the Mo-oxide coating can be well explained by the following Figure 4.17. It can be confirmed that the corrosion products generated in the crack portion of the Mo oxide layer (Spot 2) gather to form a new Zn corrosion product layer (Spot 1).

Considering the stability diagram for Zn ions in Cl^- containing corrosion environment (Figure 4.18) [34], lower pH is important as well as the high Cl^- concentration for the stabilization of the $Zn_5(OH)_8 \cdot Cl_2 \cdot H_2O$ phase. For these reasons, the Mo-oxide coating is considered to play an important role in improving the corrosion resistance of Zn-Fe-Mo plating by retarding the corrosion rate of Zn-Fe-Mo plating and stabilizing the $Zn_5(OH)_8 \cdot Cl_2 \cdot H_2O$ phase as the protective corrosion products.

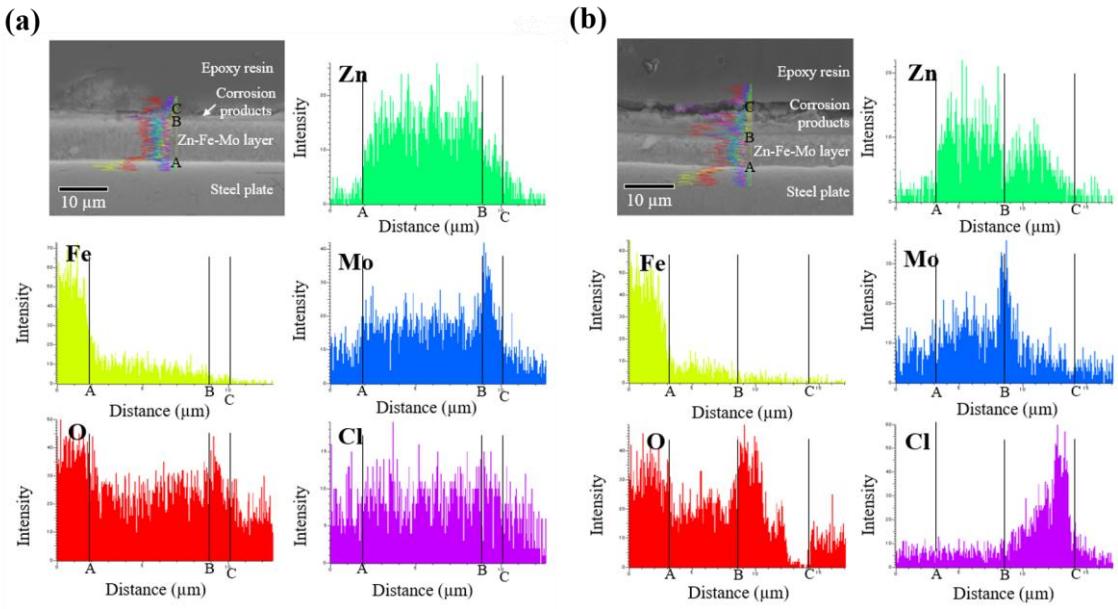

Figure 4.16 EDS line analysis results for Mo-oxide coated Zn-Fe-Mo plating after cyclic corrosion test: (a) after 15 cycles and (b) 30 cycles.

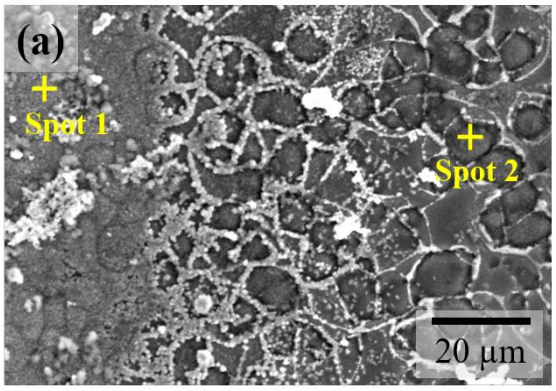

(b)

at.%	Spot 1	Spot 2
Zn	60.21	37.31
Fe	6.75	6.31
Mo	9.23	22.42
Cl	0.59	0.38
O	16.14	22.69
C	7.09	10.89

Figure 4.17 SEM images for Mo-oxide coated Zn-Fe-Mo plating after 4 cycle of cyclic corrosion test (a) and EDS elemental analysis results of each spot (b).

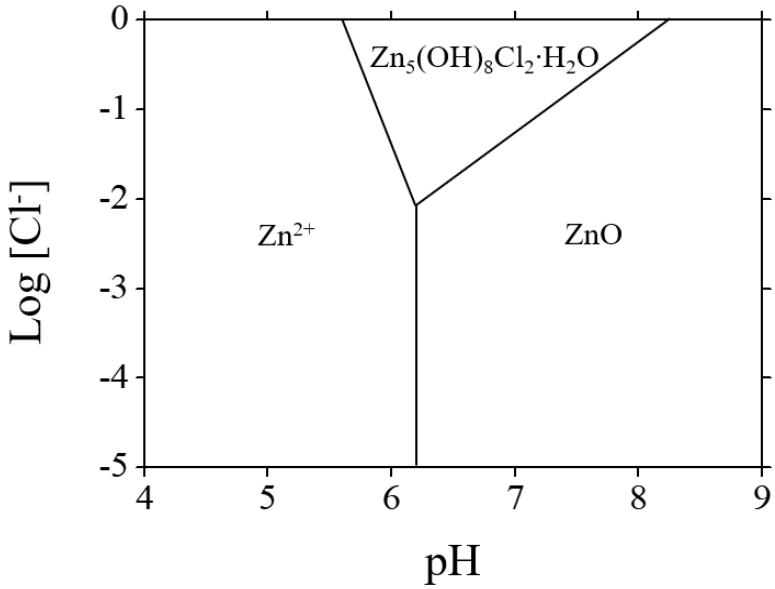

Figure 4.18 Stability diagram for Zinc ions at varying pH and chloride concentrations ([Zn^{2+}]= 0.1 M, 25 °C) [34].

4.9 Conclusion

In this study, the possibility of using ternary Zn-Fe-Mo plating as an alternative plating for anti-corrosive Zn-Ni plating was discussed. Despite the high impedance of Zn-Fe-Mo plating, CCT test results showed corrosion resistance of Zn-Fe-Mo plating itself is not sufficient. Meanwhile, an additional Mo-oxide coating was found to drastically improve the corrosion resistance of Zn-Fe-Mo plating. The formation and corrosion properties of Mo-oxide coated Zn-Fe-Mo plating were investigated in detail and the following conclusions were obtained from the results.

1. A metallic lust Mo-oxide coating was deposited on Zn-Fe-Mo plating. The partial induced reduction of molybdate ions to metal Mo at the cathode surface which containing Fe content was anticipated.
2. Despite the high impedance of ternary Zn-Fe-Mo, CCT results showed poor corrosion resistance. Moreover, impedance of Mo-oxide itself does not show high corrosion resistance. Nevertheless, Mo-oxide coated Zn-Fe-Mo plating exhibited significantly enhanced corrosion resistance at CCT. The formation of multi-layer structure had a critical contribution to the enhancement of corrosion resistance.
3. The major reasons for the improved corrosion resistance of Mo-oxide coated Zn-Fe-Mo plating were the formation of dense $Zn_5(OH)_8 \cdot Cl_2 \cdot H_2O$ phase as a corrosion product of Zn. The formation of multi-layer structure by additional Mo-oxide coating played a major role in the formation and stabilization of $Zn_5(OH)_8 \cdot Cl_2 \cdot H_2O$ phase.

Acknowledgement

References

[1] M. Izaki, Electrodeposition of iron and iron alloys, Mod. Electroplat. 4 (2010) 461–481.

[2] 井上雅博, 現代めっき教本, エレクトロニクス実装学会誌, 2012.

[3] V.S. Protsenko, F.I. Danilov, Chromium electroplating from trivalent chromium baths as an environmentally friendly alternative to hazardous hexavalent chromium baths: comparative study on advantages and disadvantages, Clean Technol. Environ. Policy. 16 (2014) 1201–1206.

[4] H. Bhatt, Alternatives to Hexavalent Chromium to Comply with European Union's Directives (ELV, RoHS and WEEE), Plat. Surf. Finish. 93 (2006) 20–23.

[5] L. Hua, Y.C. Chan, Y.P. Wu, B.Y. Wu, The determination of hexavalent chromium (Cr^{6+}) in electronic and electrical components and products to comply with RoHS regulations, J. Hazard. Mater. 163 (2009) 1360–1368.

[6] Z.L. Qun, Electrodeposition of zinc-iron alloy from an alkaline zincate bath, Met. Finish. 96 (1998) 54–57.

[7] G. Roventi, R. Fratesi, R.A. Della Guardia, G. Barucca, Normal and anomalous codeposition of Zn–Ni alloys from chloride bath, J. Appl. Electrochem. 30 (2000) 173–179.

[8] T. V Byk, T. V Gaevskaya, L.S. Tsybulskaya, Effect of electrodeposition conditions on the composition, microstructure, and corrosion resistance of Zn–Ni alloy coatings, Surf. Coatings Technol. 202 (2008) 5817–5823.

[9] J. Mackowiak, N.R. Short, Metallurgy of galvanized coatings, Int. Met. Rev. 24 (1979) 1–19.

[10] A.R. Marder, The metallurgy of zinc-coated steel, Prog. Mater. Sci. 45 (2000) 191–271.

[11] A. Tozar, I.H. Karahan, Structural and corrosion protection properties of electrochemically deposited nano-sized Zn–Ni alloy coatings, Appl. Surf. Sci. 318 (2014) 15–23.

[12] A. SHIBUYA, T. KURIMOTO, K. KOREKAWA, K. NOJI, Corrosion-resistance of electroplated Ni-Zn alloy steel sheet, Tetsu-to-Hagané. 66 (1980) 771–778.

[13] A. Goldenberg, S. Admani, J.L. Pelletier, S.E. Jacob, Belt buckles—Increasing awareness of nickel exposure in children: A case report, Pediatrics. 136 (2015) e691–e693.

[14] M. Saito, R. Arakaki, A. Yamada, T. Tsunematsu, Y. Kudo, N. Ishimaru, Molecular mechanisms of nickel allergy, Int. J. Mol. Sci. 17 (2016) 202.

[15] J. Winiarski, W. Tylus, M.S. Krawczyk, B. Szczygieł, The influence of molybdenum on the electrodeposition and properties of ternary Zn-Fe-Mo alloy coatings, Electrochim. Acta. 196 (2016) 708–726.

[16] J. Winiarski, W. Tylus, A. Lutz, I. De Graeve, B. Szczygieł, The study on the corrosion mechanism of protective ternary ZnFeMo alloy coatings deposited on carbon steel in 0.5 mol dm^{-3} NaCl solution, Corros. Sci. 138 (2018) 130–141.

[17] A. Brenner, Electrodeposition of Alloys: Practical and specific information, Academic Press, 1963.

[18] T. Akiyama, H. Fukushima, Recent study on the mechanism of the electrodeposition of iron-group metal alloys, ISIJ Int. 32 (1992) 787–798.

[19] E.J. Podlaha, D. Landolt, Induced codeposition I. An experimental investigation of Ni-Mo alloys, J. Electrochem. Soc. 143 (1996) 885–892.

[20] D. Kosugi, T. Hagio, Y. Kamimoto, R. Ichino, Effect of the addition of molybdenum on the structure and corrosion resistance of zinc–iron plating, Coatings. 7 (2017) 235.

[21] J. Winiarski, A. Leśniewicz, P. Pohl, B. Szczygieł, The effect of pH of plating bath on electrodeposition and properties of protective ternary Zn–Fe–Mo alloy coatings, Surf. Coatings Technol. 299 (2016) 81–89.

[22] J. Winiarski, W. Tylus, B. Szczygieł, EIS and XPS investigations on the corrosion mechanism of ternary Zn–Co–Mo alloy coatings in NaCl solution, Appl. Surf. Sci. 364 (2016) 455–466.

[23] 北村浩司, 森河務, 横井昌幸, 盛山浩, 電解還元法によるクエン酸塩浴からのモリブデート皮膜の形成, 表面技術. 55 (2004) 42.

[24] H. Kazimierczak, P. Ozga, R.P. Socha, Investigation of electrochemical co-deposition of zinc and molybdenum from citrate solutions, Electrochim. Acta. 104 (2013) 378–390.

[25] H. Fukushima, T. Akiyama, S. Akagi, K. Higashi, Role of iron-group metals in the induced codeposition of molybdenum from aqueous solution, Trans. Japan Inst. Met. 20 (1979) 358–364.

[26] M.-C. Chou, C.-F. Chu, S.-T. Wu, Phase transformations of electroplated amorphous iron–tungsten–carbon film, Mater. Chem. Phys. 78 (2003) 59–66.

[27] R.P. Edavan, R. Kopinski, Corrosion resistance of painted zinc alloy coated steels, Corros. Sci. 51 (2009) 2429–2442.

[28] M.S. Azevedo, C. Allély, K. Ogle, P. Volovitch, Corrosion mechanisms of Zn (Mg, Al) coated steel: 2. The effect of Mg and Al alloying on the formation and properties of corrosion products in different electrolytes, Corros. Sci. 90 (2015) 482–490.

[29] E. Diler, B. Rouvellou, S. Rioual, B. Lescop, G.N. Vien, D. Thierry, Characterization of corrosion products of Zn and Zn–Mg–Al coated steel in a marine atmosphere, Corros. Sci. 87 (2014) 111–117.

[30] J. Winiarski, W. Tylus, K. Winiarska, I. Szczygieł, B. Szczygieł, XPS and FT-IR Characterization of Selected Synthetic Corrosion Products of Zinc Expected in Neutral Environment Containing Chloride Ions, J. Spectrosc. (2018).

[31] Q. Qu, C. Yan, Y. Wan, C. Cao, Effects of NaCl and SO2 on the initial atmospheric corrosion of zinc, Corros. Sci. 44 (2002) 2789–2803.

[32] K. Nishimura, K. Kato, H. Shindo, Highly corrosion-resistant Zn-Mg alloy galvanized steel sheet for building construction materials, Nippon Steel Tech. Rep. 81 (2000).

[33] M. Uranaka, T. Shimizu, Corrosion resistance of hot-dip Zn-6% Al-3% Mg alloy coated hlkhjk, Metall. Sci. Tecnol. 30 (2013).

[34] R. Lindström, J. Svensson, L. Johansson, The atmospheric corrosion of zinc in the presence of NaCl the influence of carbon dioxide and temperature, J. Electrochem. Soc. 147 (2000) 1751–1757.

CHAPTER 5

CONCLUSIONS

Three studies on the electrodeposition of high corrosion resistive alloy platings, comprising Mo or W via structure design have been explored in this dissertation. The three methods were examined as a method for designing the structure of the plating material: the addition of the composite material, the addition of the third element, and formation of multilayer structure. Each method was found to be effective in improving the corrosion resistance of platings. The results obtained from each research are summarized as follows.

(I) Electrodeposition of Ni-W/CNT composite plating: A possible candidate for PEMFC bipolar plate coating: The incorporation of CNT, which has high electrical conductivity and excellent corrosion resistance into Ni-W alloy plating structure, had a positive effect in improving the corrosion resistance and lowering the contact resistance of plating layer. The present of inactive CNT onto the plating surface contributed to improving the corrosion resistance of the plating, and CNT that penetrate the surface oxide film on the Ni-W plating was confirmed to be effective in lowering contact resistance by acting as a conductive path. In addition, it was possible to control the structure of composite plating by adjusting the addition amount of CNT in the plating bath, which was an important factor in obtaining a uniform and improved properties of Ni-W/CNT composite plating. It was confirmed that the change of the plating structure by incorporating CNT into plating layer is an effective method for improving the corrosion resistance and conductivity of the plating material for application as a PEMFC bipolar plate coating.

***(II) Electrodeposition of a novel ternary Fe-W-Zn alloy plating: improvement of corrosion properties of binary Fe-W alloy by Zn addition*:** It has been suggested that the corrosion resistance of binary Fe-W alloy can be improved by structure control of plating via the addition of the third element, Zn. The corrosion resistance of ternary alloy plating highly depends on the Zn content of ternary alloys, which is the main factor for determining the plating structure by refining the grain size

of alloys. Nanocrystalline structured ternary alloys containing only about 1-2 at.% Zn showed improved corrosion resistance than binary Fe-W alloy and even Ni-W alloy. The electrodeposited novel ternary Fe-W-Zn alloy is expected to be applicable as a promising alternative to hexavalent Cr plating, without using harmful elements.

(III) Electrodeposition of ternary Zn-Fe-Mo plating and improvement in corrosion resistance by additional Mo-oxide coating: The presence of iron group element was essential for electrodeposition of ternary Zn-Fe-Mo alloy as well as well-adhered metallic luster Mo oxide coating onto underlying plating. The formation of multi-layer structure by additional Mo-oxide coating had a critical contribution to the enhancement of corrosion resistance by stabilizing protective Zn corrosion product, $Zn_5(OH)_8 \cdot Cl_2 \cdot H_2O$ (simonkolleite) phase. Formation of multi-layer structure by electrodeposition of less-active Mo-oxide coating on ternary Zn-Fe-Mo plating can improve the corrosion resistance of Zn-based plating by changing the corrosion mechanism of Zn.

As an overall conclusion, it was clarified that the corrosion resistance of the plating material can be significantly improved by appropriately designing the structure of the plating according to the applied environment and purpose. Even a small amount of additive such as CNT and third elements were found to drastically change the plating structure and their properties. In addition, structure design of platings can provide effective solutions for improving the properties of conventional platings and for replacing the existing platings which using harmful elements to harmless one. The developed structural design can contribute to the development of the industry as well as realizing a sustainable future society.

ACHIEVEMENTS

Publications

1. **Park J-H,** Wada T, Naruse Y, Hagio T, Kamimoto Y and Ichino R. Electrodeposition of Ni-W/CNT Composite Plating and Its Potential as Coating for PEMFC Bipolar plate. *Coatings*. 2020; 10(11): 1095

2. **Park J-H,** Hagio T, Kamimoto Y and Ichino R. Electrodeposition of a novel ternary Fe–W–Zn alloy: Tuning corrosion properties of Fe–W based alloys by Zn addition. *Journal of the Electrochemical Society*. 2020; 167:132508.

3. **Park J-H,** Kosugi D, Hagio T, Kamimoto Y, Ichino R and Lee M-H. Improvement in corrosion resistance of ternary Zn-Fe-Mo plating by additional Mo oxide coating. *Surface and Coatings Technology*. 2020; 389:125567.

4. **Park J-H,** Hagio T, Kamimoto Y, Ichino R and Lee M-H. Enhancement of corrosion resistance by lamination of Mg film on Zn-55Al-1.6Si-coated steel by physical vapor deposition. *Surface and Coatings Technology*. 2020; 387:125537.

5. **Park J-H,** Hagio T, Kamimoto Y and Ichino R. The effect of bath pH on electrodeposition and corrosion properties of ternary Fe-W-Zn alloy platings. *Journal of Solid State Electrochemistry*. 2021; 25:1901.

6. Hagio T, **Park J-H,** Naruse Y, Goto Y, Kamimoto Y, Ichino R and Bessho T. Electrodeposition of Nano-Diamond/Copper Composite Platings: Improved Interfacial Adhesion between Diamond and Copper via Formation of Silicon Carbide on Diamond Surface. *Surface and Coatings Technology*. 2020; 403:126322.

7. Hagio T, **Park J-H,** Lin Yan, Tian Yanqin, Hu Yun Hang, Kamimoto Y and Ichino R. Facile Hydrothermal Synthesis of EAB-type Zeolite under Static Synthesis Conditions. *Crystal Research and Technology*. 2021; 56(4): 2000163.

8. Naruse Y, **Park J-H,** Hagio T, Kamimoto Y, Ichino R and Bessho T. Effect of SiC formation temperature on improvement in thermal conductivity of electrodeposited SiC-coated diamond/Cu composite plating. *Composite Interfaces*. 2021; 1-18.

9. Naruse Y, **Park J-H,** Hagio T, Kamimoto Y, Ichino R and Bessho T. Electroplating of copper/microdiamond composites and the effect of diamond surface functionalization. *Functional Materials Letters*. 2021; 2151023.

Conferences

1. **Park J-H**, Ichino R and Lee M-H. Improvement of corrosion resistance of hot dip Zn-55Al plated steel sheet by Mg films prepared by PVD sputtering process. 平成 30 年度表面技術若手研究者・技術者研究交流発表会: 2018 (口頭発表), 名古屋、日本

2. **Park J-H,** Kosugi D, Hagio T, Kamimoto Y, Ichino R and Lee M-H. Enhancement of corrosion resistance by lamination of Mg film on Zn-55Al-1.6Si-coated steel by physical vapor deposition. The 12th Asian-European International Conference on Plasma Surface Engineering (AEPSE): 2019 (poster presentation), Jeju, Korea

3. **Park J-H,** Kosugi D, Hagio T, Kamimoto Y and Ichino R. Improvement of corrosion resistance of ternary Zn-Fe-Mo plating by additional Mo oxide coating. The 12th Asian-European International Conference on Plasma Surface Engineering (AEPSE): 2019 (poster presentation), Jeju, Korea

4. **Park J-H,** Hagio T, Kamimoto Y and Ichino R. 非水系溶媒を利用したアルミニウムの無電解めっき. 第 51 回溶融塩討論会: 2019 (口頭発表), 北海道、日本

5. **Park J-H,** Hagio T, Kamimoto Y and Ichino R. Fe-W 合金めっき皮膜への Zn 導入による耐食性向上の検討. 表面技術協会第 142 回講演大会: 2020 (口頭発表), 名古屋 、日本

ACKNOWLEDGEMENT

私の研究指導にあたり、親切丁寧な指導と御鞭撻を賜りました 教授 市野良一 先生に謹んで感謝いたします。市野先生のような立派な方の指導の下で学んだのがとても幸運であったと感じます。先生のおかげで、笑いがあふれるいい雰囲気の下で勉強することができました。
研究を進めるにあたり、大変貴重なご助言を頂き、 留学生活の色々な部分を助けてくださった 准教授 神本祐樹 先生に心から感謝いたします。
研究の進めと留学生活までのすべての部分にあたり助けて下さった 助教 萩尾健史 先生にも誠に感謝いたします。萩尾先生から研究者としての姿勢・教育者としての心構えの両面において貴重なご指導をいただきました。
また、忙しいところ、論文の検討してくださった 齋藤永広 先生、片山新太 先生にもお礼申し上げます。

研究の遂行から研究室での生活に至るまで、大変お世話になりました市野研究室の皆様、Dr. NIJPANICH Supinya, 國司寛人、小杉大智、後藤泰輝、西濱達郎、和田達哉、山口祥、山下雄也、成瀬優斗、坂下崇高、鈴木嵩啓、黒田涼太、早崎雄太、坂本光志朗、村瀬慶哉、松永匠平、和田慎太郎、山城拓也、鈴木響君にも誠に感謝いたします。
短い期間でしたが、私には研究室の一人一人が綺麗な思い出として残っています。みんなと一緒に過ごしたこの時を忘れません。

私からの "何が幸せな人生でしょうか？" という少し変な質問に対して、私の修士課程の指導教授である 韓国海洋大学校の 李明勳 先生からお申し越した言葉が忘れられません。
自分が価値を感じる仕事をしながら、遣り甲斐を感じるなら、それが幸せだし、成功ではないか？

私にとっての'幸せ'というのは、皆様と一緒に過ごせるこの瞬間であり、'成功'は、今の私が遣り甲斐を感じることを皆様と一緒にできるということ。
これが幸せし、成功ではないでしょうか？

2021 年、朴 載嫩